Evolving Microstructures
in Carbon Steel

A Neutron and Synchrotron Radiation Study

S.E. Offerman

Propositions accompanying the thesis

"Evolving Microstructures in Carbon Steel
A Neutron and Synchrotron Radiation Study"

S.E. Offerman

1. The presence of microchemical bands is a prerequisite for the formation of banded microstructures, but the kinetics of the phase transformations determines their actual formation.
   S.E. Offerman, N.H. van Dijk, M.Th. Rekveldt, J. Sietsma, and S. van der Zwaag,
   Mater. Sci. Technol., 18 (2002) 297-303.

2. The nucleation of a lamellar eutectoid phase is a transient process in which the pro-eutectoid grains frequently nucleate at high energy interfaces and can continue to grow, with the same crystallographic orientation, into the eutectoid phase of which the grains of the second phase nucleate at low energy interfaces.
   - S.E. Offerman, N.H. van Dijk, J. Sietsma, S. Grigull, E.M. Lauridsen, L. Margulies, H.F. Poulsen,
   * M.Th. Rekveldt, and S. van der Zwaag, Science, 298 (2002) 1003-1005.*
   - S.E. Offerman, L.J.G.W. van Wilderen, N.H. van Dijk, J. Sietsma, M.Th. Rekveldt, and S. van der Zwaag,
   * Acta Mater., 51 (2003) 3927-3938.*

3. The interplay of orientation relations and the energy of the interface between the new and parent phase, as well as the shape of the nucleus with respect to the shape of the parent grain, play a more important role in nucleation processes during solid-state phase transformations than hitherto assumed.
   This thesis, Chapter 6.

4. Detailed understanding of phase transformations in steel will not only lead to a better process control of steel but also of many other polycrystalline materials.
   This thesis.

5. Spin-echo small-angle neutron scattering opens the possibility to study the formation of precipitates from a nanometer to micrometer level in-situ in the bulk of a material.
   T. Krouglov, W.H. Kraan, J. Plomp, M.Th. Rekveldt, and W.G. Bouwman, J.Appl.Cryst.,36 (2003) 816-819.

6. The combined use of a thermomechanical simulator and a three-dimensional x-ray diffraction microscope will give in-situ information about the development of the microstructure at the level of individual grains during deformation at high temperatures, which will significantly contribute to thermomechanical research of polycrystalline materials.

7. The problem of loading and unloading hydrogen storage materials due to the slow hydrogen transport at ambient pressure and temperatures of around 50°C might be solved by using a material that has a structural phase transformation of the host matrix at around 50°C with a very low hydrogen mobility below the phase transition temperature and a very high one above the phase transition temperature.

8. A journalistic treatment of a scientific paper for the benefit of a broad audience does not guarantee a comprehensive and careful description of the original findings.

9. Original ideas originate almost everywhere, but rarely behind a desk.

10. As the emancipation of women goes on, the way to a woman's heart can be found more often through her stomach.

These propositions are considered defendable and as such have been approved by the supervisor,
prof.dr.ir. S. van der Zwaag.

Stellingen behorende bij het proefschrift

"Evolving Microstructures in Carbon Steel
A Neutron and Synchrotron Radiation Study"

S.E. Offerman

1. De aanwezigheid van microchemische banden is een voorwaarde voor het ontstaan van microstructurele banden, maar de kinetiek van de fasetransformaties bepaalt of ze daadwerkelijk ontstaan.
   S.E. Offerman, N.H. van Dijk, M.Th. Rekveldt, J. Sietsma, en S. van der Zwaag,
   Mater.Sci.Technol., 18 (2002) 297-303.

2. De kiemvorming van een lamellaire eutectoïdische fase is een tijdsafhankelijk proces waarin de pro-eutectoïdische korrels frequent op hoog energetische korrelgrenzen kiemen en kunnen doorgroeien, met dezelfde kristallografische oriëntatie, als onderdeel van de eutectoïdische fase waarvan de korrels van de tweede fase op laag energetische korrelgrenzen kiemen.
   - S.E. Offerman, N.H. van Dijk, J. Sietsma, S. Grigull, E.M. Lauridsen, L. Margulies, H.F. Poulsen,
   *   M.Th. Rekveldt en S. van der Zwaag, Science, 298 (2002) 1003-1005.*
   - S.E. Offerman, L.J.G.W. van Wilderen, N.H. van Dijk, J. Sietsma, M.Th. Rekveldt en S. van der Zwaag,
   *   Acta Mater., 51 (2003) 3927-3938.*

3. Het samenspel van de oriëntatierelaties en de energie van het grensvlak tussen de nieuwe en de oude fase, alsook de geometrie van de kiem in relatie tot de geometrie van de oude korrel spelen een belangrijkere rol in het kiemvormingsproces tijdens transformaties in vaste stoffen dan tot op heden is aangenomen.
   Dit proefschrift, hoofdstuk 6.

4. Een gedetailleerd begrip van de fasetransformaties in staal zal niet alleen tot een betere beheersing van het productieproces van staal leiden, maar ook van vele andere polykristallijne materialen.
   Dit proefschrift.

5. De uitvinding van spin-echo kleine-hoek neutronenverstrooiing schept de mogelijkheid om de vorming van precipitaten vanaf nanometer- tot micrometerschaal in situ te bestuderen in de bulk van het materiaal.
   T. Krouglov, W.H. Kraan, J. Plomp, M.Th. Rekveldt en W.G. Bouwman, J. Appl. Cryst., 36 (2003) 816-819.

6. Door een thermomechanische simulator in combinatie met een driedimensionale Röntgendiffractie-microscoop te gebruiken kan in situ informatie verkregen worden over de microstructuur op het niveau van individuele korrels tijdens deformaties op hoge temperaturen, hetgeen een belangrijke bijdrage zal leveren aan het thermomechanische onderzoek van polykristallijne materialen.

7. Het probleem van het langzaam laden en ontladen van materialen voor waterstofopslag, kan wellicht worden opgelost door een materiaal te gebruiken dat een structurele fasetransformatie van de matrix ondergaat bij $50°C$ met een langzame waterstof mobiliteit beneden de overgangstemperatuur en een hoge daarboven.

8. Een journalistieke bewerking van een wetenschappelijk artikel ten behoeve van een breed lezerspubliek staat niet garant voor een volledige en zorgvuldige beschrijving van de originele bevindingen.

9. Originele ideeën ontstaan haast overal, maar zelden achter een bureau.

10. Met het voortschrijden van de emancipatie van vrouwen kan de liefde van een vrouw steeds vaker via haar maag worden gevonden.

Deze stellingen worden verdedigbaar geacht en zijn als zodanig goedgekeurd door de promotor,
prof.dr.ir. S. van der Zwaag.

Evolving Microstructures in Carbon Steel

A Neutron and Synchrotron Radiation Study

TUDelft

Evolving Microstructures in Carbon Steel

A Neutron and Synchrotron Radiation Study

Proefschrift

ter verkrijging van de graad van doctor
aan de Technische Universiteit Delft,
op gezag van de Rector Magnificus prof.dr.ir. J.T. Fokkema,
voorzitter van het College voor Promoties,
in het openbaar te verdedigen op maandag 8 september 2003 om 15:30 uur
door

Sven Erik OFFERMAN

materiaalkundig ingenieur
geboren te Schiedam

Dit proefschrift is goedgekeurd door de promotor:
Prof.dr.ir. S. van der Zwaag

Toegevoegd promotor: Dr.ir. J. Sietsma

Samenstelling promotiecommissie:

Rector Magnificus, voorzitter
Prof.dr.ir. S. van der Zwaag, Technische Universiteit Delft, promotor
Dr.ir. J. Sietsma, Technische Universiteit Delft, toegevoegd promotor
Prof.dr. J. Ågren, Royal Institute of Technology Stockholm (Zweden)
Prof.dr. J.Th.M. de Hosson, Rijksuniversiteit Groningen
Prof.dr. G.J. Kearley, Technische Universiteit Delft
Dr. H.F. Poulsen, Risø National Laboratory (Denemarken)
Dr.ir. N.H. van Dijk, Technische Universiteit Delft
Prof.dr. I.M. Richardson, Technische Universiteit Delft, reservelid

Dr.ir. N.H. van Dijk en Dr. M.Th. Rekveldt hebben als begeleider in belangrijke mate aan de totstandkoming van het proefschrift bijgedragen.

Printed in the Netherlands

Contents

VI

VII

VIII

1. General introduction

1.1. Introduction

Steel has been investigated more extensively than any other structural material because of a combination of fundamental scientific interest and technological importance. From a technological perspective a better understanding of the metallurgical mechanisms that take place during the production process of steel are of vital importance, because they have a strong influence on the product properties. From a scientific point of view steel is a very interesting material, because the metallurgical mechanisms that occur in steel are common to two broad classes of polycrystalline materials: metals and ceramics.

    A long-standing problem in the field of materials science is the modeling of two very important metallurgical mechanisms that take place during processing of polycrystalline materials: grain nucleation and grain growth. Grain nucleation and growth phenomena are important, because they govern the kinetics of many phase transformations and recrystallization processes that largely determine the final microstructure, and thereby the mechanical properties of the material. Despite the various models that have been developed and the experimental efforts that have been made in the last 60 years, the grain nucleation and growth processes are not completely understood. An important reason is that in-situ experimental information is extremely difficult to obtain on the behavior of grains that are in the bulk of the material. This is especially the case for steel, with grain sizes that are in the nano- to micrometer range and specimen temperatures that are in the range of 600 to 1200°C.

    This thesis describes unique neutron and synchrotron experiments that give in-situ information on the behavior of grains in the bulk of carbon steel, even down to the level of individual grains. These measurements have hitherto not been realized with other techniques.

1.2. Crystallographic phases and phase transformations in carbon steel

Carbon steel consists of iron, up to 2 wt.% carbon, and small quantities of other alloying elements. The three crystallographic phases of carbon steel are austenite (γ-Fe), ferrite (α-Fe or δ-Fe), and cementite (θ). Austenite consists of a face-centred cubic (FCC) structure of iron atoms in which carbon atoms are interstitially dissolved up to a concentration of 2 wt.%. Ferrite consists of a body-centred cubic (BCC) structure of iron atoms in which carbon atoms are interstitially dissolved up to 0.02 wt.%. Cementite is an iron carbide, Fe_3C, that has an orthorhombic structure.
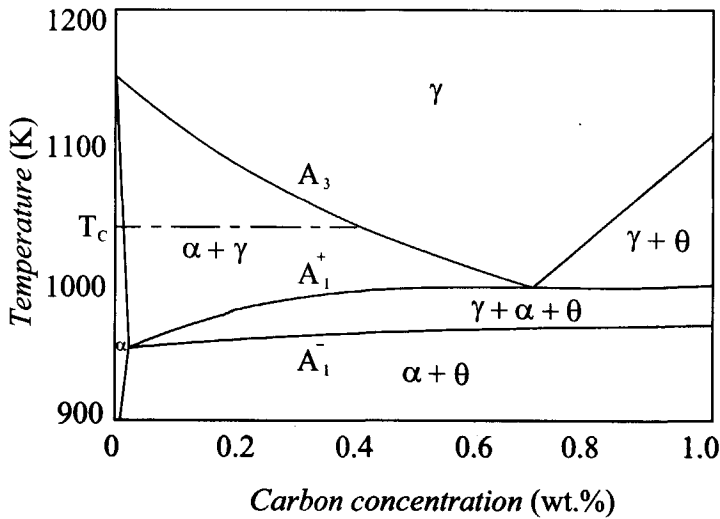
Fig. 1.1: Characteristic Fe-C quasi-binary phase diagram for carbon steel with a small amount of alloying elements. Note the three-phase region in which austenite (γ), ferrite (α), and cementite (θ) coexist and that arises as a consequence of alloying elements.

The production process of carbon steel involves several phase transformations that take place during cooling of the liquid metal to room temperature. The principal phase transformation in carbon steel is from the high-temperature austenite phase (γ) to the low-temperature ferrite phase (α). This transformation is a diffusion-controlled solid-state phase transformation. The equilibrium transition temperature or temperature range depends on the chemical composition of the steel. Fig. 1.1 shows a typical quasi-binary iron-carbon phase diagram of carbon steel that contains a small amount of alloying elements. The austenite/ferrite transition temperature (A_3) strongly depends on the carbon concentration. During continuous cooling of hypo-eutectoid steel, which contains less than 0.77 wt.% carbon (the eutectoid composition), the austenite phase will start to transform to ferrite at the austenite grain corners, since these are the most energetically favorable positions for the nucleation of the ferrite grains. The growth of the ferrite grains is accompanied by a carbon enrichment of the austenite, since the solubility of carbon in ferrite is much lower than in austenite. At lower temperatures the carbon-rich austenite decomposes into ferrite and cementite in the form of pearlite, which consists of two interpenetrating single crystals of ferrite and cementite that are primarily

2

ordered in alternating plates. As indicated in Fig. 1.1, low-alloy carbon steel usually has a three-phase region in which austenite, ferrite and cementite coexist. Under equilibrium conditions the pearlite formation starts and ends at the transition temperatures above (A_1^+) and below (A_1^-) the three phase region, respectively.

1.3. Microstructure and mechanical properties of carbon steel

At room temperature and atmospheric pressure, the microstructure of carbon steel after slow cooling is composed of ferrite and pearlite. Commercial alloys of carbon steel often contain precipitates in addition to ferrite and pearlite. Precipitates are crystallographic phases that have a different chemical composition than the matrix in which they are embedded.

The mechanical properties of carbon steel are directly related to the microstructure. For example, the Hall-Petch relation shows that the strength of a material is linearly related to the inverse of the square root of the average grain size [1]. Another example is that pearlite consisting of fine plates is harder and stronger than pearlite that consists of coarse plates [2]. The desired mechanical properties for a particular application can thus be obtained by manipulating the microstructure. Manipulation of the microstructure is a difficult process, because it requires control over the phase transformation kinetics. The phase transformation kinetics depends on the austenite state prior to the transformation, the deformation during processing, the presence of precipitates, and the chemical composition and heat treatment of the steel. In recent years, the philosophy to improve the mechanical properties moved slowly from a chemical approach, in which the addition of alloying elements played a central role, to a more physical approach, in which the control of solid-state transformations plays a central role.

1.4. Modeling the processing of carbon steel

The phase transformation model that is used in the production process plays a critical role in predicting the microstructure of modern steel grades. Unpredicted results of the austenite decomposition very often lead to undesired steel products. A detailed knowledge of the evolution of the microstructure as a function of the process parameters is essential for the production of steel grades with strictly specified demands concerning strength and formability. It is clear that a realistic phase transformation model requires a thorough knowledge of the physical parameters governing the austenite decomposition. The current austenite decomposition models for industrial conditions are often empirical or semi-empirical in nature. These models cannot be used to predict the phase transformation kinetics during new processing routes or to develop new steel grades. Therefore, there is a need to increase the understanding of phase transformations by combining state-of-the-art experimental techniques with physical phase transformation models at a granular level.

Most of the current diffusional solid-state phase transformation models are based on the classical nucleation theory (CNT) [3-6] and the law of parabolic grain growth as derived by Zener [7], which describes the growth of a pro-eutectoid phase like ferrite, in the case that the kinetics are controlled by diffusion. The growth of an eutectoid phase like pearlite is usually described by either the Zener-Hillert [8,9] or the Hillert theory [10]. These models predict nucleation and growth rates of grains and can in principle be used as input for the theory developed by Kolmogorov, Johnson, Mehl, and Avrami (KJMA) to predict the overall

3

transformation rate during isothermal phase transformations with grains nucleating randomly in space [11-15].

1.5. Experimental validation of physical phase transformation models

Experimental observations that give more detailed information about the evolution of the microstructure during austenite decomposition are crucial for the development of physical phase transformation models [16]. The traditional experimental techniques that are available to study phase transformations have limitations that complicate detailed verification of the previously mentioned physical models. Experimental techniques like dilatometry, differential scanning colorimetry, and differential thermal analysis give in-situ information about the overall transformation, but not the nucleation and growth rates. Nucleation and growth rates can be determined from a series of cross-sections of quenched samples that are analyzed by optical and electron microscopy, but this is limited to ex-situ measurements. In-situ transmission electron microscopy measurements are possible, but they are limited to the surface of thin samples and only give local information [17]. Altogether, in-situ experimental information is extremely difficult to obtain on the behavior of grains that are in the bulk of the material. This is especially the case for grain sizes that are in the nano- to micrometer range and specimen temperatures that are in the range of 600 to 1200°C. Promising experimental techniques that can provide this information involve the use of neutron and synchrotron radiation, because these types of radiation have the ability to penetrate steel and at the same time provide real-time information on the evolving microstructure.

1.6. Aim and contents of this thesis

The work presented in this thesis aims to provide in-situ experimental observations, obtained with neutron and synchrotron techniques, on the decomposition of austenite into ferrite and pearlite in carbon steel and to relate these observations to physical models that describe the phase transformation kinetics as grain nucleation and growth processes.

Chapter 2 briefly reviews the theories that are at the basis of the current physical phase transformation models. Chapter 3 describes the characteristics of the neutron and synchrotron techniques used for the research presented in this thesis, which are three-dimensional neutron depolarization (3DND), three-dimensional x-ray diffraction microscopy (3DXRD), and small-angle neutron scattering (SANS). Chapter 4 describes the influence of micro-segregation of alloying elements on the austenite decomposition into ferrite/pearlite bands. On the basis of 3DND and electron probe micro analysis (EPMA) measurements a model has been developed to predict band formation from the chemical composition and cooling path of medium carbon steel. Chapter 5 presents improvements to the experimental method and data analysis of the 3DND technique. This chapter focuses on the in-situ study of pearlite nucleation and growth during isothermal austenite decomposition in nearly eutectoid steel that has been studied with the 3DND technique. Chapter 6 presents the kinetics of individual austenite and ferrite grains during the austenite decomposition into ferrite and pearlite that was measured with the 3DXRD technique during continuous cooling in medium carbon steel. Chapter 7 presents SANS measurements of the size distributions of Nb(C,N) and MnS precipitates as a function of temperature during dissolution or precipitation in high strength low alloy (HSLA) steel.

4

References

[1] J.P. Hall and Z.Z. Petch, *Can. J. Metallurgy*, 26 (1954) 254.
[2] R.W.K. Honeycombe and H.K.D.H. Bhadeshia, In: *Steels: Microstructure and Properties*, London, Hodder Headline PLC, 1995.
[3] M. Volmer and A. Weber, *Z. Phys. Chem.*, 119 (1925) 277.
[4] R. Becker and W. Döring, *Ann. Phys.*, 24 (1935) 719.
[5] J.B. Zeldovich, *Acta Physicochim*, URSS, 18 (1943) 1.
[6] H.I. Aaronson and J.K. Lee, In: *Lectures on the Theory of Phase Transformations*, Met. Soc., New York, 1977.
[7] C. Zener, *J. Appl. Phys.*, 20 (1949) 950.
[8] C. Zener, *Trans. AIME*, 167 (1945) 550.
[9] M. Hillert, *Jerkont. Ann.*, 141 (1957) 757.
[10] M. Hillert, *Met. Trans.*, 3 (1972) 2729.
[11] A.N. Kolmogorov, *Izv. Acad. Nauk SSSR, Ser. Materm.*, 3 (1937) 355.
[12] J. Johnson and R. Mehl, *Trans. AIME* 135 (1939) 416.
[13] M. J. Avrami, *Chem. Phys.*, 7 (1939) 1103.
[14] M. J. Avrami, *Chem. Phys.*, 8 (1940) 212.
[15] M. J. Avrami, *Chem. Phys.*, 9 (1941) 117.
[16] M. Militzer, *Science* 298 (2002) 975.
[17] M. Onink, F.D. Tichelaar, C.M. Brakman, E.J. Mittemeijer, and S. van der Zwaag, *J. Mat. Sci.*, 30 (1995) 6223.

6
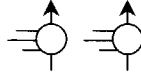
2. Solid-state phase transformation kinetics in carbon steel

2.1. Introduction

Most of the current models for diffusional solid-state phase transformation are based on the classical nucleation theory (CNT) [1-4] and the law of parabolic grain growth as derived by Zener [5], which describes the growth of a pro-eutectoid phase like ferrite, in the case that the kinetics are controlled by diffusion. The growth of an eutectoid phase like pearlite is usually described by either the Zener-Hillert [6,7] or the Hillert theory [8]. These models predict nucleation and growth rates of grains and can in principle be used as input for the theory developed by Kolmogorov, Johnson, Mehl, and Avrami (KJMA) to predict the overall transformation rate during isothermal phase transformations with randomly nucleated grains [9-13]. This chapter briefly reviews the most important results of the CNT, the Zener and Hillert models, and the KJMA theory.

2.2. Classical nucleation theory

2.2.1. Cluster formation

The formation of a stable nucleus during diffusional solid-state phase transformations begins with fluctuations in composition and structure that are the result of thermal motion. The formation of a cluster A_j, containing j atoms, from j single atoms A is given by the following reaction equation

$$jA \leftrightarrow A_j . \tag{2.1}$$

From standard chemical thermodynamics [14], the equilibrium constant K_j for this reaction is

$$K_j = \frac{a_{A_j}}{(a_A)^j} \approx \frac{x_{Aj}}{(x_A)^j} \tag{2.2}$$

where a_{A_j} and a_A are the activities of the cluster and the atom, respectively. In the case of an ideal-dilute solution the solute obeys Henry's law and the solvent obeys Raoult's law, which in the present case means that the activities can be approximated by their molar fractions x_A and x_{A_j}. The change in Gibbs free energy caused by this reaction is given by

$$\Delta G_j = -k_B T \ln(K_j), \qquad (2.3)$$

where $k_B = 1.38 \times 10^{-23}$ J/K is the Boltzmann constant and T the temperature. Substitution of eqn. (2.2) into eqn. (2.3) and taking into account that for a small number of nuclei $x_A \approx 1$ and $x_{A_j} \approx N_{A_j} / N_A$, leads to

$$N_{A_j} = N_A \exp\left(-\frac{\Delta G_j}{k_B T}\right), \qquad (2.4)$$

where N_{A_j} and N_A are the number of clusters containing j atoms and the total number of atoms per unit volume, respectively.

2.2.2. Critical nucleus

The change in Gibbs free energy ΔG during heterogeneous nucleation of ferrite on austenite grain boundaries, edges, or corners has the following contributions [15]:

1. The creation of ferrite below the transition temperature results in a reduction of the Gibbs free energy by $V\Delta G_V$, where V is the ferrite volume and ΔG_V is the difference in Gibbs free energy per unit volume between the austenite G^γ and ferrite G^α. ΔG_V is also known as the driving force for nucleation and depends on the chemical composition and temperature.
2. The removal of an area $A^{\gamma\gamma}$ of austenite/austenite grain boundary with grain boundary energy $\gamma^{\gamma\gamma}$ results in the reduction of the Gibbs free energy by $A^{\gamma\gamma}\gamma^{\gamma\gamma}$.
3. The creation of an area $A^{\alpha\gamma}$ of ferrite/austenite interface with interface energy $\gamma^{\alpha\gamma}$ results in the increase of the Gibbs free energy by $A^{\alpha\gamma}\gamma^{\alpha\gamma}$.
4. The misfit strain that arises because the transformed volume does not fit perfectly into the space originally occupied by the matrix results in an increase of the Gibbs free energy by $V\Delta G_S$.

The total change in Gibbs free energy is thus given by

$$\Delta G = -V(\Delta G_V - \Delta G_S) + \sum_i A^i \gamma^i, \qquad (2.5)$$

where the index i represents all the interfaces that play a role during nucleation.
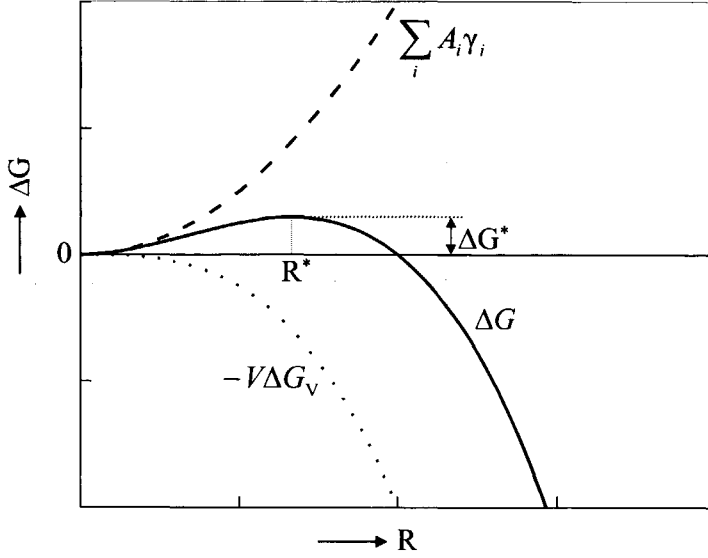
Fig. 2.1: The total change in Gibbs free energy ΔG as a function of the cluster dimension R is the sum of the interfacial energies $\sum_i A^i \gamma^i$ and the change in volume free energy $V\Delta G_V$. The size of the critical nucleus R^* is determined by the maximum in ΔG, which is the activation energy for nucleation ΔG^*. The contribution of the strain energy ΔG_S was neglected.

The misfit strain effectively reduces ΔG_V, but is usually assumed to be zero, because its value is not accurately known [16]. The ferrite volume increases with $z_V R^3$, where z_V is a geometrical parameter depending on the shape of the nucleus and R is the nucleus dimension. The interfacial area is given by $z_A^i R^2$, where z_A^i is a geometrical parameter depending on the shape of the ith interface. Fig. 2.1 shows a typical example of the change in Gibbs free energy as a function of the particle dimension. The critical nucleus is defined by the maximum in ΔG. The size R^* of the critical nucleus is thus given by

$$R^* = \frac{2\sum_i z_A^i \gamma^i}{3 z_V \Delta G_V} \tag{2.6}$$

The corresponding activation energy for nucleation ΔG^* is given by

$$\Delta G^* = \frac{4}{27} \frac{\left(\sum_i z_A^i \gamma^i\right)^3}{z_V^2 \Delta G_V^2} . \tag{2.7}$$

In the case of solid-state phase transformations the activation energy for heterogeneous nucleation, i.e. nucleation at inhomogeneous places like grain boundaries and dislocations, can be much smaller than for homogeneous nucleation. The activation energy for the

9

formation of a nucleus decreases in the following order: homogeneous nucleation, nucleation on grain boundaries, edges, and corners [17].

INTERFACIAL ENERGY AND CRITICAL NUCLEUS SHAPE

The optimal or energetically most favorable shape of the critical nucleus is that particular shape resulting in the minimum activation energy for nucleation as given by eqn. (2.7). It has not yet been possible to determine experimentally the exact shape of the critical nucleus. Several theoretical attempts have been made in order to determine the optimal shape of the nucleus of which the most common are the double spherical cap [18] and the pillbox model [16]. The interfacial energies γ^i play an important role in these models, but the exact interfacial energies are difficult to determine, because they depend on the local chemical composition and the degree of coherence of the interface. In general, the interfacial energy is high for an incoherent interface and low for a coherent interface. Because of the uncertainties in γ^i and z^i we will use a simplified version of eqn. (2.7), written as

$$\Delta G^* = \frac{\Psi}{\Delta G_V^2},$$

(2.8)

where

$$\Psi = \frac{4\left(\sum_i z_A^i \gamma^i\right)^3}{27 z_V^2},$$

(2.9)

which contains all the information about the shape of the nucleus and the interfacial energies that are involved in the nucleation. The balance between the energy that is required for the formation of new interfaces and the energy that is released due to the removal of old interfaces is represented by the factor Ψ. It is the uncertainty in Ψ which makes predictions of the nucleation rate very difficult.

DRIVING FORCE FOR NUCLEATION

The driving force for nucleation is the difference in Gibbs free energy between the austenite matrix G^γ and the ferrite nucleus G^α, i.e. $\Delta G_V = G^\gamma - G^\alpha$. The probability to form a critical nucleus increases with increasing difference in Gibbs free energy. The largest difference in Gibbs free energy is likely to be the determining quantity in the nucleation process. This energy can be found via the parallel tangent construction in a free energy versus composition plot. A graphical representation of this construction is shown in Fig. 2.2. First, the line k is constructed, which is the tangent to the free energy curve of the austenite at the initial carbon concentration x_0. The line l is the tangent to the free energy curve of the ferrite that is parallel to the line k. The carbon composition of the ferrite during nucleation $x_{C,nu}^\alpha$ is the point where the line l is the tangent of the free energy curve of the ferrite.

10
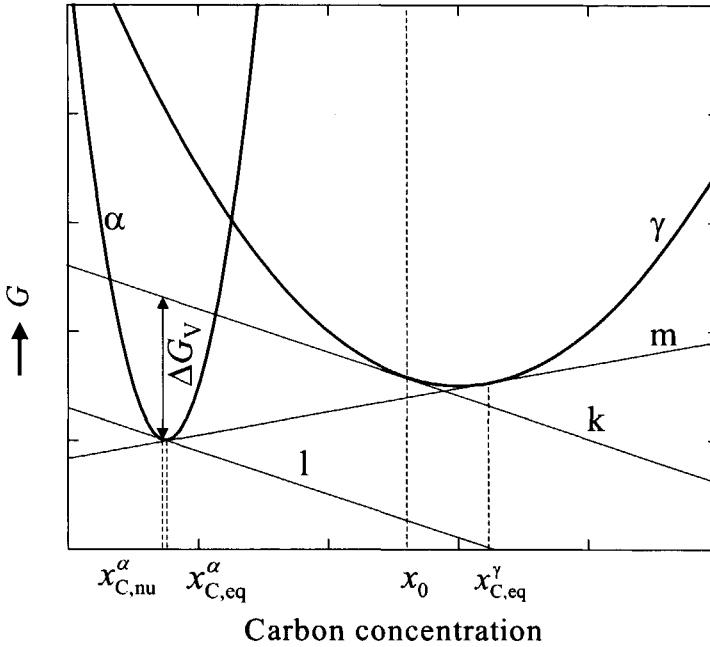
Fig. 2.2: The Gibbs free energy G as a function of the molar fraction of carbon atoms x_C in austenite and ferrite. The driving force for nucleation ΔG_V is determined via the parallel tangent construction (lines k and l, see text).

The distance between the lines k and l determines the driving force for nucleation ΔG_V as calculated via the parallel tangent construction. This approach requires that the Gibbs free energy curves of ferrite and austenite are known. For practical reasons the Gibbs free energies that are determined from bulk samples are used. However, a nucleus consisting of 10 – 100 atoms might have a different Gibbs free energy curve. For completeness the line m is drawn, which represents the common tangent between the ferrite and the austenite that gives the equilibrium carbon concentrations in austenite $x_{C,eq}^\gamma$ and ferrite $x_{C,eq}^\alpha$. Note that $x_{C,eq}^\alpha \neq x_{C,nu}^\alpha$.

2.2.3. Steady-state nucleation rate

The number of stable clusters or critical nuclei that form under equilibrium conditions is obtained by the substitution of $N_{A_j} = N^*$ and $\Delta G = \Delta G^*$ in eqn. (2.4), yielding:

11

$$N^* = N_n \exp\left(-\frac{\Delta G^*}{k_B T}\right),$$
(2.10)

where N_n is the number of potential nucleation sites in the case of heterogeneous nucleation. In the case of homogeneous nucleation N_n equals N_A. The steady-state nucleation rate $\dot{N}_{SS}$ of ferrite is equal to the rate at which critical nuclei are formed:

$$\dot{N}_{SS} = Z\beta^* N_n \exp\left(-\frac{\Delta G^*}{k_B T}\right),$$
(2.11)

where the Zeldovich factor Z is given by

$$Z = \sqrt{-\frac{1}{2\pi kT}\left(\frac{\partial^2 \Delta G}{\partial j^2}\right)_{j=j^*}}.$$
(2.12)

The Zeldovich factor takes into account the reduction in the number of critical nuclei that become supercritical during nucleation. The value for Z is nearly constant (≈ 0.05), because the rate of formation of critical nuclei and their growth to a supercritical size are similar, determined by atom diffusion onto the growing cluster of atoms.

The rate at which the (iron) atoms are added onto the critical nucleus is taken into account by the frequency factor β^*. The number of atoms N_{α_d} that are within a single jump distance α_d from the surface of the critical nucleus S^* is approximately

$$N_{\alpha_d} \approx \frac{S^*}{a^2},$$
(2.13)

where a is the interatomic distance. The atomic jump frequency Γ is related to the diffusion coefficient D by [15]

$$\Gamma = \frac{6D}{\alpha_d^2}.$$
(2.14)

The frequency factor β^* is then given by multiplication of eqns (2.13) and (2.14):

$$\beta^* \approx \frac{6DS^*}{\alpha_d^2 a^2}$$
(2.15)

In general the diffusion coefficient in eqn. (2.15) can be written as

$$D = D_0 \exp\left(-\frac{Q_D}{k_B T}\right)$$
(2.16)

12

where Q_D is the activation energy for diffusion of the (iron) atoms in the original (austenite) phase. The pre-exponential factor is given by [15]

$$D_0 = \frac{1}{6} \alpha_d^2 z f^* \exp\left(\frac{\Delta S}{k_B}\right),$$ (2.17)

where z is number of nearest neighbor sites to which the atom can jump, ΔS the entropy change for diffusion, f^* is the attempt frequency which is usually taken as being [19]

$$f^* = \frac{k_B T}{h} \approx 10^{13} s^{-1},$$ (2.18)

where $h = 6.62608 \times 10^{-34}$ Js is the Planck constant.

2.2.4. Time-dependent nucleation rate

In general the steady-state nucleation rate is not reached instantaneously, but the nucleation rate develops with time according to [4]

$$\dot{N} = \dot{N}_{SS} \exp\left(-\frac{\tau}{t}\right),$$ (2.19)

in which the so-called incubation time τ is given by

$$\tau = \frac{-4k_B T}{\beta^* \left(\frac{\partial^2 \Delta G}{\partial j^2}\right)_{j=j^*}}.$$ (2.20)

Fig. 2.3 illustrates the time dependence of the nucleation rate.

In general, predictions of the absolute nucleation rate are very difficult, because a number of parameters are not accurately known, like the interfacial energies and the shape of the critical nucleus. These parameters are contained in the ψ parameter, see eqn. (2.9). Moreover, each nucleation site can differ in local chemical composition, which in turn gives a spread in local driving forces for nucleation over the specimen. Thus, in polycrystalline specimens there is a range of both the activation energies and driving forces for nucleation and the shapes of the critical nuclei. Predictions of the nucleation rate are further complicated by the fact that the overall nucleation rate is the sum of homogeneous and several types of heterogeneous nucleation rates. Another complicating factor is the experimental determination of nucleation rates, which makes validation of the nucleation theory difficult. There exist very few in-situ techniques that have the potential to measure nucleation rates in the interior of a steel specimen.
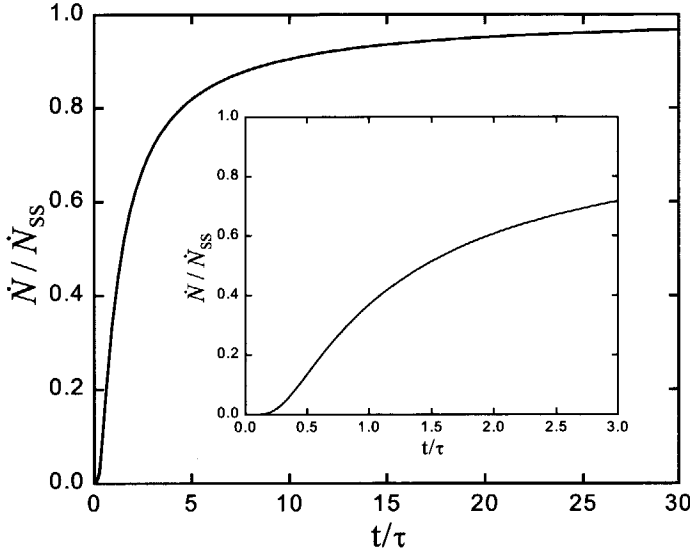
Fig. 2.3: The nucleation rate $\dot{N}$ normalized to the steady state nucleation rate $\dot{N}_{ss}$ as a function of the time t relative to the incubation time τ corresponding to eqn. (2.19).

2.3. Growth

2.3.1. Ferrite growth

Ferrite nucleation is followed by growth. The classical Zener model [5] predicts a parabolic growth for a spherical grain when the growth rate is limited by diffusion. This theory is commonly used to describe the growth of ferrite grains in construction steels during the transformation from austenite. Since the solubility of carbon in ferrite is two orders of magnitude lower than in austenite, the carbon piles up at the moving interface and diffuses into the bulk of the austenite phase. This forms the rate-limiting process for the ferrite grain growth during the phase transformation. During the initial stages of the transformation, in which the growth of the individual grain is not limited by interactions between neighboring grains due to overlapping diffusion fields (soft impingement) or existing grain boundaries (hard impingement), the radius of a ferrite grain R^{α} as a function of time t is given by the Zener model as

$$R^{\alpha}(t) = \chi\sqrt{D_{C,v}^{\gamma}(t - t_s)}, \tag{2.21}$$

where t_s is the moment of nucleation of the grain and χ is a parameter that is determined by the carbon solubilities in ferrite and austenite and can be approximated by [5]

14

$$\chi = 2.102 \left(\frac{C_\infty^\gamma - C_{eq}^\gamma}{C_{eq}^\alpha - C_\infty^\gamma} \right)^{0.5871}, \tag{2.22}$$

where C_{eq}^α and C_{eq}^γ are the equilibrium carbon concentrations in ferrite and austenite, respectively, obtained from the phase diagram, and C_∞^γ is the carbon concentration in the austenite matrix far away form the austenite/ferrite interface. Fig. 2.4 shows a schematic drawing of the carbon concentrations near the austenite/ferrite interface. In a first approximation the carbon concentration in the austenite matrix far away from the austenite/ferrite interface C_∞^γ equals the initial or average carbon concentration C_0. The volume diffusion coefficient of carbon in austenite $D_{C,V}^\gamma$ depends on the temperature and the nominal carbon concentration and can be described by [20]

$$D_{C,V}^\gamma = 4.53 \times 10^{-7} \left(1 + Y_C (1 - Y_C) \frac{8339.9}{T} \right) \exp \left\{ - \left(\frac{1}{T} - 2.221 \times 10^{-4} \right) (17767 - 26436 Y_C) \right\}, \tag{2.23}$$

where $D_{C,V}^\gamma$ is in m^2/s and the temperature T in K. The site fraction Y_C of carbon on the interstitial sub-lattice is given by

$$Y_C = \frac{x_C}{1 - x_C}, \tag{2.24}$$

where x_C is the overall atom fraction of carbon in the alloy.

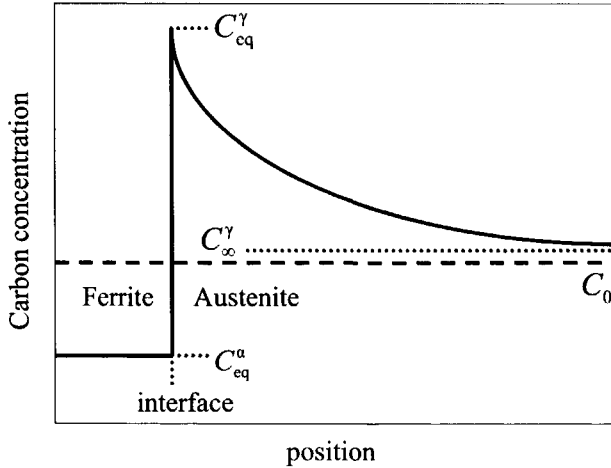*Fig. 2.4: The carbon concentration profile at the ferrite/austenite interface during diffusion-controlled growth. The carbon piles up at the interface, because the carbon solubility in ferrite is much smaller than in austenite.*

15

2.3.2. Pearlite growth

The formation of pearlite is a nucleation and growth process that involves the formation of two interpenetrating single crystals of ferrite and cementite (Fe_3C), which are primarily ordered as alternating plates. In hypo-eutectoid steels the pro-eutectoid ferrite nucleates first and continues to grow with the same crystallographic orientation during the pearlite formation as part of a pearlite colony [21]. However, cementite still has to nucleate in order to form pearlite. In hyper-eutectoid steels the roles of ferrite and cementite are reversed. In perfectly eutectoid steel the pearlite nucleation is assumed to take place at the austenite grain corners, edges, and boundaries and it is not clear which phase nucleates first. However, this situation will hardly arise under practical circumstances, since local inhomogeneities in commercial steel will result in hypo- and/or hyper-eutectoid regions. The exact nature of the pearlite formation mechanism is still under debate. One of the open questions is whether the pearlite growth is controlled by the volume or grain boundary diffusion of carbon.

2.3.2.1. Pearlite growth controlled by volume diffusion

In the Zener-Hillert model [6, 7], which assumes that volume diffusion of carbon is the rate-controlling mechanism for the growth of pearlite, the growth rate v_V is given by

$$v_V = \frac{D^\gamma_{C,V}}{k_V} \frac{\lambda^2}{\lambda^\alpha \lambda^\theta} \frac{C^{\gamma\alpha}_{eq} - C^{\gamma\theta}_{eq}}{C^\theta_{eq} - C^\alpha_{eq}} \frac{1}{\lambda} \left(1 - \frac{\lambda_c}{\lambda}\right), \tag{2.25}$$

where k_V is a geometrical constant related to the volume diffusion mechanism, and λ^α and λ^θ are the lamella thicknesses of the ferrite and cementite, respectively. The pearlite lamellar spacing amounts to $\lambda = \lambda^\alpha + \lambda^\theta$. $C^{\gamma\alpha}_{eq}$ and $C^{\gamma\theta}_{eq}$ are the equilibrium carbon concentrations in the austenite in contact with ferrite and cementite, respectively. C^θ_{eq} is the equilibrium carbon concentration in cementite. The critical (theoretical minimum) spacing λ_c is given by

$$\lambda_c = \frac{2\gamma^{\alpha\theta} T_{A1}}{\Delta T} \frac{V_m}{\Delta H_m}, \tag{2.26}$$

where $\gamma^{\alpha\theta} = 0.94$ J/m^2 [22] is the interfacial free energy of the ferrite/cementite interface in the pearlite, T_{A1} is the austenite/pearlite equilibrium transition temperature, $\Delta T = T_{A1} - T$ is the undercooling, $\Delta H_m = 4.3$ kJ/mol [22] is the change in molar enthalpy, and $V_m = 7.1\times10^{-6}$ m^3/mol is the molar volume of pearlite.

2.3.2.2. Pearlite growth controlled by grain boundary diffusion

In the Hillert model [8], which assumes that grain boundary diffusion of carbon is the rate-controlling mechanism for the growth of pearlite, the growth rate v_{GB} is given by:

$$v_{GB} = 12k_{GB} D^\gamma_{C,GB} \frac{\lambda^2}{\lambda^\alpha \lambda^\theta} \frac{C^{\gamma\alpha}_{eq} - C^{\gamma\theta}_{eq}}{C^\theta_{eq} - C^\alpha_{eq}} \frac{\delta}{\lambda^2} \left(1 - \frac{\lambda_c}{\lambda}\right), \tag{2.27}$$

16

where k_{GB} is the ratio of carbon concentration in the bulk of the austenite and the grain boundary and δ is the thickness of the boundary. The grain boundary diffusion coefficient of the carbon atoms $D_{C,GB}^{\gamma}$ can be estimated by assuming that the activation energy is half that of the activation energy for volume diffusion [15]. In the present case the argument of the exponential factor in eqn. (2.23) is multiplied by 0.5 to calculate $D_{C,GB}^{\gamma}$ as a function of x_C and T. For the eutectoid composition $C_{eq}^{\theta} = 6.67$ wt.% , $C_{eq}^{\alpha} \approx 0.02$ wt.%, $\dfrac{\lambda^{\alpha}}{\lambda^{\theta}} \approx 7$, and $k_V = 0.72$ [7]. Furthermore, we can assume that $\left(C_{eq}^{\gamma\theta} - C_{eq}^{\gamma\alpha}\right) \propto \Delta T$, and $\lambda \propto \Delta T^{-1}$ [23].

As a consequence the two different theories, represented by equations (2.25) en (2.27), can both be rewritten in the following form:

$$v_X = c_X D_{C,X}^{\gamma} \left(\Delta T\right)^{\zeta}, \tag{2.28}$$

where the subscript X equals either V or GB, which represents the volume or grain boundary diffusion theory, respectively. c_X is a constant, which is different for volume or grain boundary diffusion of carbon. The exponent ζ expresses the different temperature dependence for the two processes. For volume diffusion $\zeta = 2$ and for grain boundary diffusion $\zeta = 3$. Hence, the rate determining mechanism for the growth of pearlite can be determined from the dependence of the growth rate on the undercooling, or more specifically from the exponent ζ.

2.4. Overall transformation

The nucleation and growth rates form the basic input parameters for the KJMA theory that predicts the overall transformation kinetics. The KJMA theory predicts the fraction f of the formed phase as a function of the isothermal transformation time t as

$$f(t) = 1 - \exp\left(-k_g v^d \int_0^t \dot{N}_u(t')(t - t')^d \, dt'\right), \tag{2.29}$$

where v is a constant growth rate, d the dimensionality of the growth, and k_g a constant that depends on the geometry of the particle. For spherical particles ($d = 3$) the constant is $k_g = 4\pi/3$. The nucleation rate $\dot{N}_u$ is defined as the number of nuclei per unit untransformed volume per unit time. It is assumed that the nuclei are randomly distributed. The integration parameter t' can be interpreted as the time at which nucleation of grains took place.

Within the KJMA theory it is usually assumed that either there is a fixed number of pre-existing nuclei N_c throughout the transformation or that the nucleation rate is constant: $\dot{N}_u = k_u$. In the former case the transformed fraction as a function of time is given by

$$f(t) = 1 - \exp\left(-N_c k_g (vt)^d\right). \tag{2.30}$$

In the latter case the transformed fraction is given by

$$f(t) = 1 - \exp\left(-\frac{k_u k_g v^d t^{d+1}}{d+1}\right).$$ (2.31)

Cahn [24] showed that when the nucleation rate, per unit untransformed volume, increases with time according to

$$\dot{N}_u(t) = k_u t^m,$$ (2.32)

where k_u and m are constants, the KJMA equation becomes

$$f(t) = 1 - \exp\left(-\frac{8\pi m!}{(m+4)!} k_u v^3 t^{m+4}\right),$$ (2.33)

for spherical particles that grow at a constant rate.

Cahn [17] also derived equations for site-saturated transformations on grain surfaces, edges, and corners. These are, respectively:

$$f(t) = 1 - \exp(-2Bvt),$$ (2.34)

$$f(t) = 1 - \exp(-\pi L(vt)^2),$$ (2.35)

and

$$f(t) = 1 - \exp\left(-\frac{4}{3}\pi\eta(vt)^3\right),$$ (2.36)

where B is the grain boundary area, L is the edge length and η the number of grain corners per unit volume.

The generalized KJMA equation can be expressed as

$$f(t) = 1 - \exp(-kt^n),$$ (2.37)

where $k = \ln(2)(t_{1/2})^{-n}$ is a rate constant, which depends on the nucleation and growth characteristics and n is referred to as the Avrami exponent. The time to transform half of the volume is represented by $t_{1/2}$. The Avrami exponent depends on the characteristics of the phase transformation. For a transformation in which the growth rate is constant in three directions ($d = 3$) at least three different values for the Avrami exponent can be expected:
  a) $n = 3$ for a fixed number of pre-existing nuclei;
  b) $n = 4$ for a constant nucleation rate;
  c) $n = 5$ for a nucleation rate that increases linearly with time.
Fig. 2.5 shows the typical sigmoidal shape of the fraction curves as predicted by the KJMA theory for the three different values of the Avrami exponent n, as calculated with eqn. (2.37).

However, different transformation modes may give the same Avrami exponent. For example a transformation in which the nucleation rate is constant and the growth of (plate-like) precipitates is in two dimensions, results in $n = 3$. This example shows that the

information about the transformation mechanism may not unambiguously be determined from the Avrami exponent.

In summary, the physical models that are described in this chapter form the basis of many current phase transformation models. These models are widely used to interpret experimental observations even beyond the limitations set by theory, as is often the case with the KJMA theory. The results can often not be unambiguously interpreted with the KJMA theory, because of experimental difficulty in simultaneously determining nucleation, growth and overall transformation rates, as well as the relative spatial position of the grains. Furthermore, the nucleation and growth theories are still under debate. The activation energy for nucleation is the key parameter in predicting nucleation rates, but is extremely hard to measure accurately, which complicates experimental validation of the calculated activation energies. The parabolic growth law derived by Zener is widely used, but in-situ experimental validation has hitherto not been possible for grains in the interior of a specimen. Moreover, the discussion on the rate determining mechanism for the pearlite growth rate has not been settled. Therefore, there is a need for experimental studies that provide this in-situ and simultaneously obtained information. Potential techniques for this purpose are described in the next chapter.
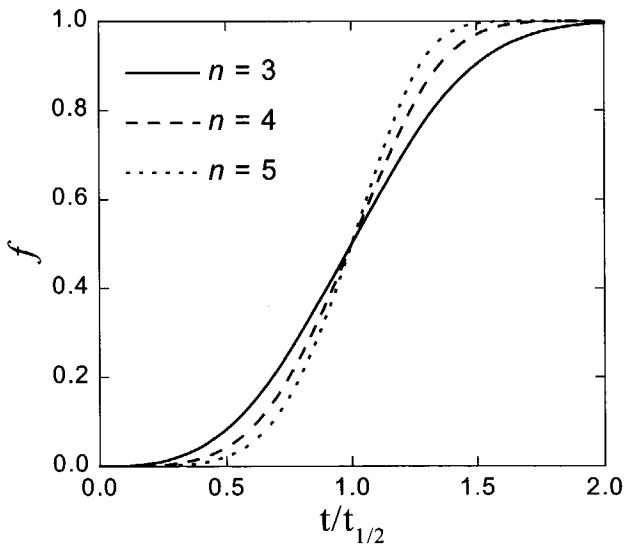
Fig. 2.5: The fraction transformed f as a function of the time t relative to the time to transform half the volume $t_{1/2}$ as given by eqn. (2.37) for three different values of the Avrami exponent n.

References

[1] M. Volmer and A. Weber, *Z. Phys. Chem.*, 119 (1925) 277.

[2] R. Becker and W. Döring, *Ann. Phys.*, 24 (1935) 719.

[3] J.B. Zeldovich, *Acta Physicochim*, URSS, 18 (1943) 1.

[4] H.I. Aaronson and J.K. Lee, In: *Lectures on the Theory of Phase Transformations*, Met. Soc., New York, 1977.

[5] C. Zener, *J. Appl. Phys.*, 20 (1949) 950.

[6] C. Zener, *Trans. AIME*, 167 (1945) 550.

[7] M. Hillert, *Jerkont. Ann.*, 141 (1957) 757.

[8] M. Hillert, *Met. Trans.*, 3 (1972) 2729.

[9] A.N. Kolmogorov, *Izv. Acad. Nauk SSSR, Ser. Materm.*, 3 (1937) 355.

[10] J. Johnson and R. Mehl, *Trans. AIME* 135 (1939) 416.

[11] M.J. Avrami, *Chem. Phys.*, 7 (1939) 1103.

[12] M.J. Avrami, *Chem. Phys.*, 8 (1940) 212.

[13] M.J. Avrami, *Chem. Phys.*, 9 (1941) 117.

[14] P.W. Atkins, In: *Physical chemistry*, Oxford University Press, Oxford, 1994.

[15] D.A. Porter and K.E. Easterling, In: *Phase Transformations in Metals and Alloys*, London, Chapman & Hall, 1993.

[16] W.F. Lange III, M. Enomoto, and H.I. Aaronson, *Metall. Trans. A*, 19A (1988) 427.

[17] J.W. Cahn, *Acta Metall.*, 4 (1956) 449.

[18] W.C. Johnson, C.L. white, P.E. Marth, P.K. Ruf, S.M. Tuominen, K.D. Wade, K.C. Russell, and H.I. Aaronson, *Metall. Trans. A*, 19A (1975) 911.

[19] J.W. Christian, *The Theory of Transformations in Metals and Alloys*, Oxford, Pergamon Press, 1981.

[20] J. Ågren, *Scripta Metall.*, 20 (1986) 841.

[21] S.W. Thompson and P.R. Howell, *Scripta Metall.*, 22 (1988) 1775.

[22] A.K. Jena and M.C. Chaturvedi, In: *Phase Transformations in Materials*, London, Prentice-Hall, 1992.

[23] P.R. Howell, *Mat. Char.*, 40 (1998) 227.

[24] J.W. Cahn, *Trans. AIME*, 209 (1957) 140.
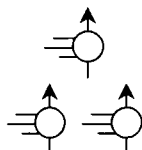
3. In-situ neutron and synchrotron techniques

3.1. Introduction

The traditional experimental techniques that have been available to study phase transformations have limitations that prevent verification of the physical models described in chapter 2. Experimental techniques like dilatometry, differential scanning colorimetry and differential thermal analysis give in-situ information about the overall transformation, but not on the nucleation and growth rates. Nucleation and growth rates can be determined from a series of cross-sections of quenched samples that are analyzed by optical and electron microscopy, but this is limited to ex-situ measurements. In-situ transmission electron microscopy measurements are possible, but they are limited to the surface of thin samples and only give local information [1]. Altogether, the traditionally used experimental techniques can not simultaneously give in-situ information about grain nucleation and growth rates and the overall transformation rate. There is a need for experimental techniques that give more detailed information about the evolution of the microstructure during the austenite decomposition [2].

Promising experimental techniques that provide this information involve the use of neutron and synchrotron radiation, because these types of radiation have the ability to penetrate steel and at the same time provide real-time information on the microstructural evolution. Neutrons are electrically neutral and interact with the nucleus of the atom, which is relatively small compared to the electron cloud of the atom. Therefore, neutrons penetrate relatively easily into steel. The spin of the neutron interacts with the local magnetic induction in the sample which makes it sensitive to the magnetic (micro)structure of the material. X-rays interact with the electron cloud of the atom and therefore do not easily penetrate steel, as is the case for x-rays from conventional laboratory machines. However, hard x-rays (> 50 keV) from a synchrotron source have such high energies that it is possible to probe the bulk of steel. An x-ray beam of 80 keV penetrates through 4 mm of steel [3]. The in-situ neutron and synchrotron techniques that were used for the research that is described in this thesis are three-dimensional neutron depolarization (3DND), three-dimensional x-ray diffraction (3DXRD) microscopy, and small-angle neutron scattering (SANS). These techniques are

21

used in combination with optical microscopy, dilatometry, and electron probe micro analysis (EPMA).

Previous work of Krielaart showed that the application of the three-dimensional neutron depolarization technique to the study of the phase transformations in steel opens new opportunities in the field of steel research [4]. The technique simultaneously gives information about the ferrite and pearlite fractions, the average particle size, and the spatial distribution of the particles during the austenite decomposition in the bulk of a steel sample. From these measurements nucleation and growth rates, as well as the overall transformation rate are determined, which can be compared to theoretical models. Te Velthuis improved the experimental set-up of the 3DND technique by the design of a two-stage furnace, which allows the in-situ study of isothermal phase transformations [5]. The advantage of studying isothermal transformations rather than continuous cooling transformations is that the time and temperature characteristics of the transformation can be separated. The work of Te Velthuis on the austenite decomposition into ferrite and pearlite is continued in this thesis.

Recently, the development of x-ray microscopes at synchrotron sources with focused high-energy x-rays created the opportunity to go one step further in the characterization of the evolution of the microstructure than the 3DND technique. The three-dimensional x-ray diffraction microscope allows the in-situ study of *individual* grains in the bulk of a metal [6]. The 3DXRD microscope gives detailed information about the phase transformations in steel, which at present cannot be obtained with any other experimental technique. In particular the quantitative data on the nucleation behavior are unique. Furthermore, the growth rates of the individual grains can be measured with this technique. In addition, the 3DXRD technique gives information about the fraction transformed and the behavior of individual austenite grains.

Although the 3DND and 3DXRD techniques give detailed information about the microstructural evolutions in steel, they are not suited at the moment to study precipitate size distributions in the nanometer range. Precipitates have an important influence on the mechanical properties of metals. For example, NbC precipitates facilitate the formation of small ferrite grains during the austenite decomposition. In addition, precipitates form pinning centers for dislocations and thereby increase the tensile strength. Small angle neutron scattering (SANS) can be used to determine particle size distributions of precipitates that are embedded in the microstructure. SANS is a well-established technique to obtain structural information about inhomogeneities in materials with a characteristic length in the range of 1 – 100 nm. The technique has successfully been applied to the study of carbide precipitation in ultrahigh strength steels [7].

3.2. Three-dimensional neutron depolarization

The 3DND technique provides unique information about the magnetic domain structure in the bulk of ferromagnetic materials. The technique was successfully applied to study e.g. the micro-magnetic state of materials [8], magnetic recording materials [9], internal stresses and structural relaxation in amorphous metals [10], and magnetic flux lines in high-T_c superconductors [11]. More recently, the phase transformations in steel [5] and the retained austenite in transformation induced plasticity (TRIP) steel [12] were studied by neutron depolarization.

The 3DND technique is a powerful tool for the study of phase transformations in steel, because it provides a unique insight into the formation of the microstructure. The 3DND technique simultaneously probes the fraction, the mean magnetic particle size, and the spatial distribution of the forming ferromagnetic phase in the paramagnetic matrix. The

22

technique is capable of determining these three parameters in-situ and in the bulk of the material. The experimental method and theory to the study the phase transformation kinetics in steel with the 3DND technique, are briefly discussed in this section. A more detailed description can be found in the work of Rekveldt and co-workers [13-15] and in particular in the thesis of Te Velthuis [5].

3.2.1. Experimental method of three-dimensional neutron depolarization

The 3DND experiments were performed at the Poly Axis Neutron Depolarization Analyzer (PANDA) at the Interfaculty Reactor Institute (IRI). Fig. 3.1 shows a schematic drawing of the experimental method. A polarization vector P that points in the direction of the neutron spins represents the polarized neutron beam. The length of the vector is one if all the neutrons in the beam have their spin in the same direction. A small external magnetic field of approximately 5 mT is applied along the z-axis of the sample (vertical direction), as is drawn in Fig. 3.1.

The sample contains ferromagnetic ferrite domains in a paramagnetic austenite matrix during the austenite to ferrite and pearlite phase transformations in steel. During transmission through the sample the neutron spin interacts with the local magnetic induction of the magnetic domains. The neutron spins precess (rotate) around the local magnetic induction vector. Each neutron passes a different part of the steel sample within the cross-section of the beam and thus precesses over a different angle. The transmitted neutron beam is characterized by an average direction and spread in the orientation of the neutron spins. The polarization direction of the transmitted neutron beam is represented by a vector, which points in the average direction of the neutron spins. The length of the vector is related to the spread in orientation of the neutron spins. The increase in spread in orientation of the neutron spins leading to a shortening of the polarization vector is referred to as depolarization.
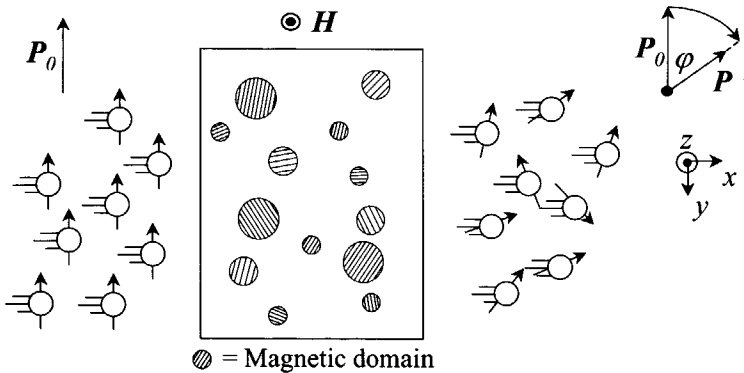

= Magnetic domain

*Fig. 3.1: Schematic drawing of the 3DND technique. The applied magnetic field **H** is oriented along z, out of the plane of the drawing.*
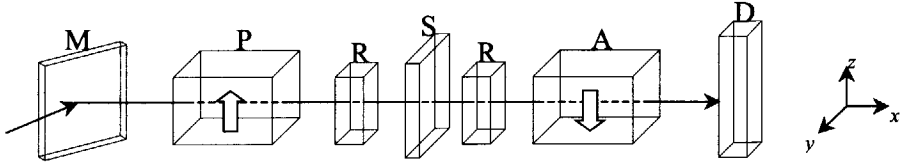
Fig. 3.2: Schematic drawing of experimental set-up for the 3DND measurements. The arrow denotes the neutron beam. The instrument consists of a Monochromator, a Polarizer, two polarization Rotators, the Specimen, a polarization Analyzer and a Detector. The convention used in this thesis is that the neutrons propagate in the x-direction and that the applied magnetic field is along the z-direction.

Fig. 3.2 shows a schematic drawing of the 3DND set-up. A white beam of thermal neutrons is obtained from a nuclear reactor. A focussed monochromatic neutron beam with a wavelength of $\lambda_n = 0.1240 \pm 0.0012$ nm is produced from pyrolytic graphite crystals (M). A polarized neutron beam is created with a supermirror neutron polarizer (P). The polarization direction of the incoming neutron beam can be set to the x-, y-, and z-direction with the first rotator (R). The neutrons interact with the sample (S). The transmitted neutron beam can be analyzed in the x-, y-, and z-direction with the use of the second rotator (R), the analyzer (A), and a ^{3}He gas-filled detector (D). The polarizer and anlyzer both have a polarization of approximately 98%. The beam size is 20×20 mm^2.

3.2.2. Theory of three-dimensional neutron depolarization

The transmission of a monochromatic polarized neutron beam through a magnetic specimen is characterized by the depolarization matrix D according to

$$P' = D \cdot P, \tag{3.1}$$

where P and P' are the polarization vectors before and after transmission, respectively. The difference between P and P' is related to the direction and length of the vectors. The rotation of the polarization vector is related to the average magnetic induction of the sample, which is a measure for the magnetic volume fraction. The shortening of the polarization vector is related to the different variations in local magnetic induction that the neutrons encounter during their interaction with the sample. Shortening of the polarization vector means depolarization of the neutron beam, which is a measure for the average magnetic domain size.

The elements of the (3×3) matrix D are experimentally determined from the measured neutron intensities I_{ij} according to

$$D_{ij} = \frac{I_s - I_{ij}}{I_s P_0}, \tag{3.2}$$

where I_s is the shim intensity that corresponds to the intensity of a fully depolarized beam and is given by

24

$$I_s = (I_{zz} + I_{zZ})/2. \tag{3.3}$$

The subscript $j = x, y, z$ represents the direction in which the initial beam is polarized, and $i = x, y, z$ represents the spin direction that is analyzed. A capital subscript indicates the negative direction. The polarization of the empty beam P_0 is determined by the combined efficiency of the polarizer and analyzer from

$$P_0 = \frac{I_{zZ}^0 - I_{zz}^0}{I_{zZ}^0 + I_{zz}^0}. \tag{3.4}$$

In the case of a non-zero average magnetization in the z-direction in the sample, which is achieved with the external magnetic field, the following matrix elements are approximately zero: D_{xz}, D_{yz}, D_{zx}, and D_{zy}.

The rotation φ of the polarization vector is determined from the experiment according to

$$\varphi = \arctan\left(\frac{D_{xy} - D_{yx}}{D_{xx} + D_{yy}}\right). \tag{3.5}$$

The measured rotation φ of the polarization vector is related to the volume fraction f of the ferromagnetic phase via

$$\varphi = \eta L_x c^{1/2} <B>, \tag{3.6}$$

where η is the shape factor that accounts for the effect of stray fields, L_x is the thickness of the sample, and $c = 2.15 \times 10^{29} \lambda_n^2 \, T^{-2} m^{-4}$. The average magnetic induction $<B>$ inside the sample is given by

$$<B> = f<m_z>\mu_0 M_s, \tag{3.7}$$

where $<m_z>$ is the average reduced magnetization in the direction of the applied magnetic field (5.16 mT) in the z-direction, $\mu_0 = 4\pi \times 10^{-7}$ H/m, and f and M_s are the fraction and saturation magnetization of the ferromagnetic phase, respectively. In the case of the formation of pro-eutectoid ferrite $f = f^\alpha$ and $M_s = M_s^\alpha$, where f^α is the volume fraction pro-eutectoid ferrite and the saturation magnetization of ferrite M_s^α [16] is given by

$$M_s^\alpha(T) = M_0^\alpha (1-\tau)^\beta \left[1 - \beta\tau + A\tau^{3/2} - C\tau^{7/2}\right]^{-1} \tag{3.8}$$

where $\mu_0 M_0^\alpha = 2.20$ T and $\tau = T/T_C^\alpha$ is the reduced temperature relative to the ferrite Curie temperature of $T_C^\alpha = 1043$ K. The constants $\beta = 0.368$, $A = 0.110$, and $C = 0.129$ were determined for pure iron. In the case of the formation of pearlite $f = f_p$ and $M_s = M_s^p$, where f_p is the pearlite fraction and the saturation magnetization of pearlite M_s^p is calculated from

$$M_s^p = f_p^\alpha M_s^\alpha, \tag{3.9}$$

25

where f_p^α is the ferrite fraction present in pearlite. Eqn. (3.9) is valid if $T > T_C^\theta = 483$ K, where T_C^θ is the Curie temperature of cementite. For the studied steels f_p^α is evaluated with the thermodynamic database MTDATA$^\circledR$.

The shape factor η that accounts for the effect of stray fields contains a macroscopic and a microscopic contribution according to

$$\eta = (1-f)\eta^P + f\eta^M \tag{3.10}$$

with the macroscopic shape factor given by [17]

$$\eta^M = \frac{2}{\pi}\arctan\left(\frac{L_z}{L_y}\right) = 0.905 \tag{3.11}$$

for the macroscopic plate-like sample with $L_x \times L_y \times L_z = 0.4 \times 15 \times 100$ mm^3 and the microscopic shape factor $\eta^P = 0.5$ for microscopic spherically shaped particles. From eqns. (3.6), (3.7), and (3.10) the formed fraction is deduced and given by

$$f = \frac{-\eta^P + \sqrt{(\eta^P)^2 + \frac{4(\eta^M - \eta^P)\varphi}{\langle m_z\rangle\mu_0 M_s L_s \sqrt{c}}}}{2(\eta^M - \eta^P)} \tag{3.12}$$

under the assumption that $<m_z>$ is constant throughout the transformation. The reduced magnetization $<m_z>$ is determined at the end of the transformation from field dependent measurements [15].

The correlation function ξ is a measure for the size of the magnetic fluctuations. It is proportional to the correlation length of the fluctuations in the magnetic induction ΔB around the mean magnetic induction along the neutron path, given by

$$\Delta B = B - <B>. \tag{3.13}$$

The depolarization of the polarized neutron beam, described by det(D), is related to the correlation function ξ in the following manner [5]:

$$\det(D) = \exp\{-2cL_x\xi\}. \tag{3.14}$$

For a narrow domain size distribution, the average magnetic domain radius δ is related to the correlation function ξ according to [18]

$$\delta = \frac{3c_3\xi}{2f(\mu_0 M_s)^2(1 - c_2c_3m_z^2)}, \tag{3.15}$$

where the constants c_2 and c_3 are given by

$$c_2 = \left(\frac{4\pi f^2}{81}\right)^{\frac{1}{3}}$$

(3.16)

and

$$c_3 = \frac{32}{9(3 - <m_z^2>)}.$$

(3.17)

As can be seen from eqn. (3.16) the calculation of δ includes the fraction f that is derived from φ. The average of the square of the z-component of the magnetization $<m_z^2>$ is given by

$$<m_z^2> = \frac{\frac{32}{9}c_2 m_z^2(\gamma_z - 1) + \frac{1}{4} - 3\gamma_z}{-(\gamma_z + \frac{5}{4})}$$

(3.18)

where

$$\gamma_z = 1 - \frac{2\ln(D_{zz})}{\ln(\det(D))}$$

(3.19)

is a measure for the magnetic texture.

The measured depolarization can be written as $\det(D) = D_\perp^2 D_{//}$, where $D_\perp$ and $D_{//}$ are the components of the depolarization matrix D that are perpendicular and parallel to the applied magnetic field, respectively. In the case that the magnetic particles are not randomly distributed over the sample, an extra depolarization of the neutron beam will arise, which is not related to the magnetic domain size. This extra depolarization will affect all the D-elements that are perpendicular to the applied magnetic field, while the component that is parallel to the magnetic field remains unaffected. In order to separate the contribution of the average magnetic domain size and clustering (non-random spatial distribution) of particles to the depolarization, a cluster factor D_c is introduced:

$$D_c = \int_0^\infty f(N)\cos\left[(N - \langle N \rangle)\varphi_p\right]dN,$$

(3.20)

where $f(N)$ is the normalized spatial distribution function of the number of particles N along a neutron path, $<N>$ is the average number of particles along the neutron path, and φ_p is the average rotation per domain [19]. The cluster factor is a measure for the degree of cluster formation in the specimen. In order to calculate the average magnetic domain size, a corrected value $D'_\perp$ is to be used, defined as $D'_\perp = D_\perp/D_c$.

The rotation φ of the polarization vector is not influenced by the manner in which the magnetic domains are distributed.

3.3. Three-dimensional x-ray diffraction microscopy

The 3DXRD microscope provides detailed information about polycrystalline materials. The power of the technique lies in the fact that it provides in-situ information about individual grains in the bulk of the material. Recent studies that used three-dimensional x-ray

microscopy have led to new insights into grain rotation during deformation [20], the elastic strain tensors in bent silicon [21], the recrystallization kinetics of grains during annealing [6], the austenite stability in TRIP steel during tensile testing [22], and the phase transformation kinetics in steel [23]. The latter study is described in chapter 6 of this thesis. The experimental method and theory to study the phase transformation kinetics in steel with the 3DXRD microscope are treated in this section. A more detailed description and broader perspective of the use of the 3DXRD microscope can be found in the work of Poulsen and co-workers [24], who developed the 3DXRD microscope, and in particular the thesis of Lauridsen [25].

3.3.1. Experimental method three-dimensional x-ray diffraction microscopy

The 3DXRD microscope used for this study is located at beamline ID11 of the European Synchrotron Radiation Facility (ESRF). Fig. 3.3 shows a schematic drawing of the experimental set-up as it was used to study phase transformation kinetics. A white synchrotron beam diffracts from a bent silicon Laue crystal, which gives a monochromatic (80keV), vertically focussed x-ray beam. Two sets of vertical and horizontal slits define the beam size at the sample, which is typically 100×100 μm^2. In order to illuminate the sample uniformly, a homogeneous flux of photons is needed over the whole cross-section of the beam. The sample is positioned out of focus. In this way the beam size can be altered with the slits during the experiment. The sample was placed in a specially designed furnace [26], which allowed the in-situ study of the austenite decomposition in steel by x-ray diffraction. The furnace is positioned on a table, which can be translated in three directions (x, y, z) and rotated over an angle ω (see Fig. 3.3). The diffracted x-rays are recorded with a 2D-detector (Frelon CCD camera).
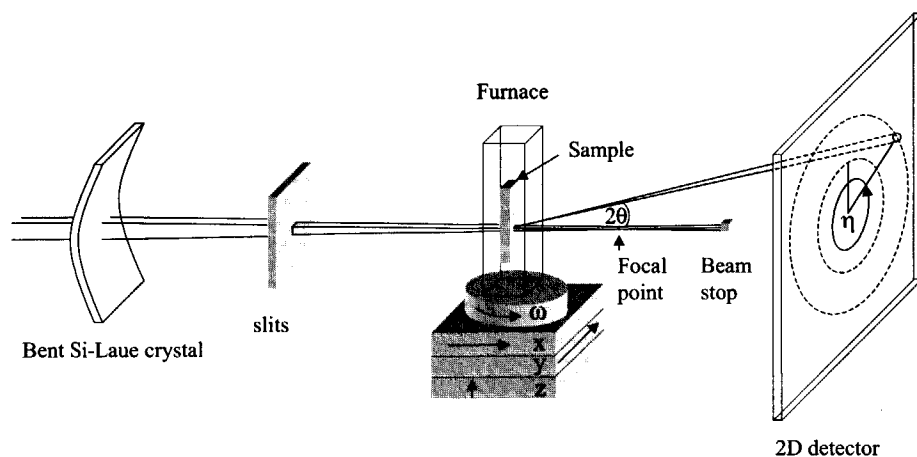
Fig. 3.3: Schematic drawing of the experimental set-up for the 3DXRD measurements. The set-up consists of a bent Si-Laue crystal, slits, and a 2D detector. The specimen is positioned in a furnace, which is mounted on a table that can be translated and rotated.
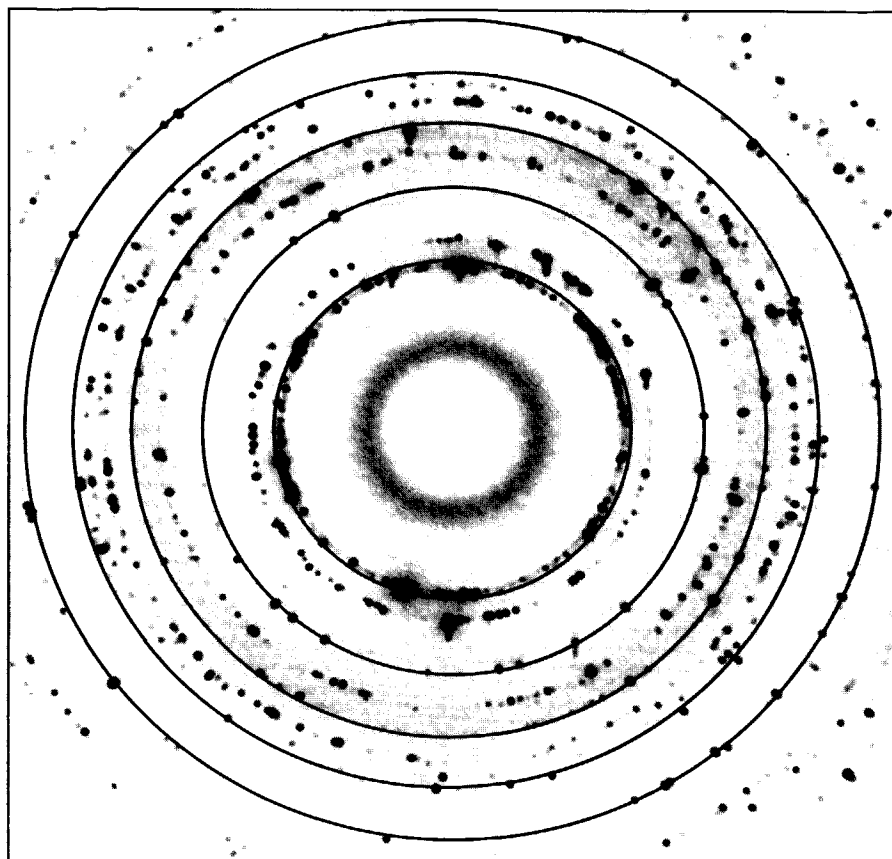
Fig. 3.4: X-ray diffraction pattern of steel showing the separate austenite and ferrite reflections at 763 °C. The solid rings indicate the expected scattering angles from the ferrite grains illuminated by the x-ray beam. From the inside towards the outside the following {hkl} diffraction rings are completely with the range of the detector: γ_{111}, α_{110} (close to γ_{111}), γ_{200}, α_{200}, γ_{220}, α_{211}, γ_{311}, γ_{222}, α_{220}, α_{310}, γ_{400} (close to α_{310}).

Separate diffraction spots appear on the recorded diffraction pattern of which an example is shown in Fig. 3.4. The detection of separate reflections is achieved by choosing a relatively small beam size of about 5 times the maximum size of the grains in the material under investigation. As a result a limited number of grains contribute to the diffraction pattern. Each diffraction spot on the detector corresponds to a single grain in the material. The typical recording time of a diffraction pattern is of the order of 1 s.

The complete Bragg intensity of an individual grain is recorded by slightly rotating the sample about the z-axis (see Fig. 3.3) over an angle $\Delta\omega$. The rotation angle $\Delta\omega$ should be larger than the mosaicity of the grain in order to measure the complete Bragg intensity. However, the rotation angle $\Delta\omega$ should be small enough to avoid overlap with reflections of other grains that are within the $\Delta\omega$-range of the measurement. An optimum value of $\Delta\omega$ needs to be found before the actual experiment is performed. However, even after the optimum value of $\Delta\omega$ is found, it is still to be verified for every diffraction spot that the central $\Delta\omega$-scan contains the complete Bragg-intensity of an individual grain without overlap of reflections from other grains. This is achieved by measuring additional $\Delta\omega$-scans on either side of the central $\Delta\omega$-scan. The $\Delta\omega$-scans on either side of the central $\Delta\omega$-scan should not contain any Bragg intensity in the case that (a) the complete Bragg intensity is measured in the central $\Delta\omega$-scan and (b) there is no overlap with reflections of other grains within the measured central $\Delta\omega$-scan. This is named the ω-validation. Moreover, the diffraction spots can overlap in the η-direction (see Fig. 3.3) on the detector, but this can be controlled with the beam size.

In addition to the ω-validation it is also necessary to verify that particular grains do not partly grow outside the illuminated volume. To verify that a grain is completely positioned within the illuminated volume, the beam size was extended to 140×140 μm² every sixth time that the central $\Delta\omega$-scan was recorded. In the case that a particular grain would partly grow outside the illuminated volume, this results in an increase in Bragg intensity of the corresponding diffraction spot. Only the Bragg intensities from grains that are completely positioned within the central beam size of 100×100 μm² can be correctly translated into grain sizes.

3.3.2. Theory of three-dimensional x-ray diffraction microscopy

3.3.2.1 Diffracted intensity from a small single crystal

The diffracted intensity I_g per unit time of a single grain, which is rotated through the Bragg-condition in order to illuminate the whole grain, can be written in the kinematic approximation as [27, 28]:

$$ I_g = \Phi_0 r_0^2 \frac{\lambda^3 |F_{hkl}|^2 V_g}{\Delta\omega v^2} L_g P \exp(-2M), \qquad (3.21) $$

where Φ_0 is the incident flux of photons, F_{hkl} is the structure factor of the $\{hkl\}$-reflection, λ is the photon wavelength, V_g is the volume of the grain, $\Delta\omega$ is the angular range over which the grain is rotated, v is the volume of the unit cell, and P is the polarization factor. The Lorentz factor of the grain is given by $L_g = 1/\sin(2\theta)$, where 2θ is the scattering angle. The Thomson scattering length r_0 is given by

$$ r_0 = \frac{e^2}{4\pi\varepsilon_0 m_e c^2} = 2.82 \times 10^{-15}\,\text{m}, \qquad (3.22) $$

where $e = 1.602\times10^{-19}$ C is the electron charge, $m_e = 9.1094\times10^{-31}$ kg is the electron mass, $c = 2.9979\times10^8$ m/s is the velocity of light, and $\varepsilon_0 = 8.85419\times10^{-12}$ F/m is the permittivity of

30

vacuum. The Debye-Waller factor exp(-2M) accounts for the thermal vibrations of the atoms, with [29]

$$M = \frac{6h^2 T}{m k_B \Theta^2} \left[\phi(x) + \frac{x}{4} \right] \left(\frac{\sin\theta}{\lambda} \right)^2 \tag{3.23}$$

where $h = 6.62608 \times 10^{-34}$ Js is the Planck constant, m is the mass of the vibrating atom ($m_{Fe} = 9.27 \times 10^{-26}$ kg), $k_B = 1.381 \times 10^{-23}$ J/K is the Boltzmann constant, Θ is the Debye temperature ($\Theta_{Fe} = 430$ K), $x = \Theta/T$ is the relative temperature, T is the temperature, and

$$\phi(x) = \frac{1}{x} \int_0^x \frac{\xi}{\exp(\xi) - 1} d\xi . \tag{3.24}$$

In the derivation of eqn. (3.21) it is assumed that the single crystal rotates at a constant angular velocity about an axis perpendicular to the scattering vector and perpendicular to the primary beam. In this case a rotation $\Delta\omega$ causes a change in the scattering angle of $\Delta(2\theta)$. In the case that the scattering vector makes an angle η with the rotation axis (see Fig. 3.3) unequal to 90°, the change in scattering-angle is given by $\Delta(2\theta) = \Delta\omega|\sin\eta|$. The total diffracted intensity of a single crystal can only be determined if $\Delta\omega|\sin\eta|$ is larger than the mosaicity of the crystal. Note that the time that a grain is in reflection during rotation depends on η. The diffracted intensity is independent of the rotation angle in the extreme case that $\eta = 0°$ (or 180°). The diffracted intensity from the {hkl}-planes of a single grain that makes an angle η with the axis of rotation can thus be written as

$$I_g = \Phi_0 r_0^2 \frac{\lambda^3 |F_{hkl}|^2 V_g(t)}{\Delta\omega|\sin\eta| v^2} L_g P \exp(-2M) . \tag{3.25}$$

3.3.2.2 Diffracted intensity from a powder

The integrated intensity I_p per unit time of a {hkl}-diffraction ring of a polycrystalline material (also named powder in diffraction terms) with randomly oriented grains is given by

$$I_p = \Phi_0 r_0^2 \frac{m_{hkl} \lambda^3 |F_{hkl}|^2 V(t)}{v^2} L_p P \exp(-2M) , \tag{3.26}$$

where m_{hkl} is the multiplicity factor of the hkl-ring and V is the volume of the diffracting phase. The Lorentz factor for a powder is given by $L_p = 1/(4\sin(\theta))$. The volume of the diffracting phase is given by

$$V = f^j V_{gauge} , \tag{3.27}$$

where f^j is the volume fraction of the diffracting phase and V_{gauge} is the gauge volume, which is defined by the beam size and the thickness of the sample.

31

3.3.2.3. Calculation of the grain volume from the measured intensities

The volume of an individual grain is calculated from the measured grain intensity I_g normalized by the powder intensity I_p of the *hkl*-ring in which the reflection from the individual grain appeared. Combining eqns. (3.25-3.27) gives

$$V_g = \frac{1}{2} m_{hkl} \Delta\omega |\sin\eta| \cos(\theta) f^j(t) V_{gauge} \frac{I_g}{I_p}. \tag{3.28}$$

3.3.3. Computational method

The volume of an individual grain can not be calculated directly from eqn. (3.28), because it requires that the time-dependent fraction of the forming phase f^j is known a priori. However, at the end of the austenite/ferrite transformation it can be assumed that the equilibrium ferrite fraction f_{eq}^α has formed, which can be calculated from the thermodynamic database MTDATA®. Therefore, the measured time-dependent ferrite grain intensity is normalized by the powder intensity at the end of the transformation $I_p(t_f)$:

$$V_g^\alpha(t) = \frac{1}{2} m_{hkl}^\alpha \Delta\omega |\sin\eta| \cos(\theta) f_{eq}^\alpha V_{gauge} \frac{I_g^\alpha(t)}{I_p^\alpha(t_f)} \frac{\Phi_0(t_f)}{\Phi_0(t)} \frac{\exp[-2M(T_f)]}{\exp[-2M(T)]}, \tag{3.29}$$

where t_f and T_f are the time and temperature at the end of the transformation, respectively. The ratio $\Phi_0(t_f)/\Phi_0(t)$ appears in eqn. (3.29), because the flux of photons from the synchrotron decreases with time. The ratio of the Debye-Waller factors appears in eqn. (3.29), because the atomic vibrations decrease the peak intensity with increasing temperature. However, the ratio of the Debye-Waller factors is exactly unity in the case of isothermal phase transformations and approximately unity for the temperature region in which the austenite decomposition takes place during continuous cooling. The decrease in the flux of photons can be determined from

$$\frac{\Phi_0(t_f)}{\Phi_0(t)} = \frac{I_b(t_f)}{I_b(t)}, \tag{3.30}$$

where $I_b(t_f)$ and $I_b(t)$ are the total intensities of a background ring on the 2D-detector, in which no diffraction spots occur, and which is arbitrary chosen between the austenite and ferrite diffraction rings at time t_f and t, respectively.

  The diffraction patterns that were recorded with the 2D-detector are analyzed with computer software written by S. Schmid and E.M. Lauridsen of the Risø national laboratory. The software was modified for the present data analysis. After a first treatment of the raw data, the analysis is split up in a part that is related to a single grain, and a part that is related to a complete *hkl*-ring. This resulted in the following 7 steps:

1. The width of a (diffraction) ring on the detector is chosen such that all the spots are within this ring during the transformation. The diffraction ring is divided into 1440

wedges ($\Delta\eta = 0.25°$), which gives the intensity per wedge as a function of the angle η along the diffraction ring $I_w(\eta)$.

The results from step 1 can be used for the single grain and powder analysis, from which I_g and I_p are obtained.

SINGLE GRAIN ANALYSIS:
2. ω-validation: check if the intensity of an individual reflection is completely contained in the central $\Delta\omega$-scan. This is the case if the two additional $\Delta\omega$-scans have intensities that correspond to the background intensity in the 2θ and η-range of the reflection.
3. Determination of the starting angle η_s and the finishing angle η_f of each diffraction peak for the central $\Delta\omega$-scan. Check if there is no peak overlap with other grains.
4. Intensity integration along the ring between the η-limits of each peak:

$$I_g^{raw} = \sum_{\eta=\eta_s}^{\eta_f} I_w(\eta),$$

(3.31)

where I_g^{raw} is the raw intensity from an individual ferrite grain.

5. Determination of the background intensity of an individual ferrite grain $I_g^b(t)$:

$$I_g^b(t) \equiv I_g^b(t_0)\frac{I_b(t)}{I_b(t_0)},$$

(3.32)

where, $I_g^b(t_0)$ is the integrated intensity between η_s and η_f of the diffraction ring, in which the ferrite reflection appeared during the austenite/ferrite transformation, but at a time t_0 at which the steel was still completely austenitic. $I_g^b(t)$ decreases with time, because the incoming flux of photons from the synchrotron decreases with time, which is determined from

$$\frac{\Phi_0(t)}{\Phi_0(t_0)} = \frac{I_b(t)}{I_b(t_0)}.$$

(3.33)

Therefore, $I_g^b(t_0)$ is multiplied by $I_b(t)/I_b(t_0)$ in order to get the time-dependent background intensity for an individual ferrite grain $I_g^b(t)$. In the case that the beam size is increased (for validation) the background intensity increases. The background intensity of a grain at a time t^v that the beam size is increased $I_g^b(t^v)$ is determined from

$$I_g^b(t^v) = I_g^b(t_0^v)\frac{I_b(t^v)}{I_b(t_0^v)},$$

(3.34)

where $I_g^b(t_0^v)$ is the integrated intensity between η_s and η_f of the diffraction ring, in which the ferrite reflection appeared during the austenite/ferrite transformation, but at a time t_0^v at which the steel was still completely austenitic, measured with the increased beam size.

33

6. Subtraction of the background intensity from the raw intensity of an individual ferrite grain:

$$I_g(t) = I_g^{raw}(t) - I_g^b(t),$$ (3.35)

where $I_g(t)$ corresponds to the intensity of an individual grain as given by eqn. (3.25). The intensity from a grain in a validation measurement is determined from

$$I_g(t^v) = I_g^{raw}(t^v) - I_g^b(t^v).$$ (3.36)

POWDER ANALYSIS

7. In analogy to the single grain analysis, the intensity of the $\{hkl\}$-ring I_p is determined from

$$I_p(t) = I_p^{raw}(t) - I_p^b(t)$$ (3.37)

with

$$I_p^{raw} = \sum_{\eta=0}^{2\pi} I_w(\eta)$$ (3.38)

and the background intensity of the powder ring $I_p^b(t)$ is determined from

$$I_p^b(t) \equiv I_p^b(t_0) \frac{I_b(t)}{I_b(t_0)}.$$ (3.39)

The powder intensity of a particular $\{hkl\}$-ring contains the summed intensity of all the grains that are fully and partly in reflection for that $\{hkl\}$-ring.

When both I_g and I_p have been determined by the described method, the volume of a single grain can now be calculated from eqn. (3.29). The fraction transformed can be calculated from the integrated intensity of the $\{hkl\}$-reflection. An average intensity $<I>$ of the ring is determined from the three $\Delta\omega$-scans (the central and the two additional validation scans that are denoted by + and -) and is given by

$$\langle I \rangle = \frac{I_p^+ + I_p + I_p^-}{3}$$ (3.40)

From the powder intensity after the transformation and the equilibrium ferrite fraction, the ferrite fraction during the transformation f^α can then be calculated as

$$f^\alpha = \langle f^\alpha \rangle = \frac{\langle I \rangle}{\langle I \rangle^f} f_{eq}^\alpha.$$ (3.41)

34

3.4. Small-angle neutron scattering

Small-angle neutron scattering (SANS) is a widely used technique to investigate the shape and size of large molecules, small particles, porous materials and structural inhomogeneities with dimensions in the range of 1 - 100 nm. The technique allows the study of colloids, polymers, biomolecules, alloys, composites, porous systems, and precipitates in metallic systems [30 - 33]. The experimental method and theory to study the NbC precipitation process in HSLA steel with the SANS technique are treated in this section.

3.4.1. Experimental method and theory of small-angle neutron scattering

The SANS experiments described in this thesis were performed at the LOQ instrument at ISIS. The principal benefit of conducting SANS experiments at ISIS is that a 'white' incident beam is combined with time-of-flight detection techniques to give LOQ a very large dynamic range in scattering vector, all of which is accessible in a single measurement without need to reconfigure the instrument [30]. This means that a large range of particle sizes can be measured in a relatively short time compared to SANS instruments that require moving the detector.

Fig. 3.5 shows a schematic drawing of the SANS method. After a neutron beam is obtained from a spallation source, choppers select the wavelength range for the experiment. The neutron beam is collimated and reduced to the appropriate size and shape by apertures. The incident neutrons are characterized by a plane wavevector k that is related to the neutron wavelength λ_n by

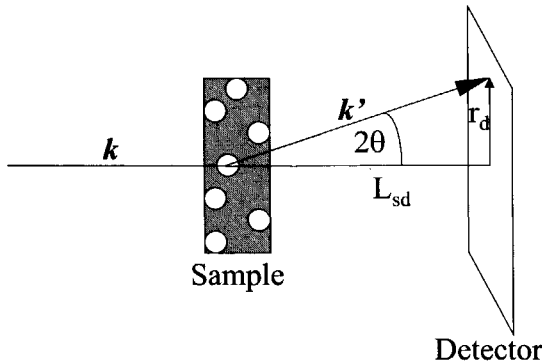$$\|k\| = k = \frac{2\pi}{\lambda_n} .$$

(3.42)

Fig. 3.5: Layout of the small-angle neutron scattering technique. The neutrons scatter from inhomogeneities in the sample over a scattering angle 2θ and are detected by a two-dimensional area detector.

The neutrons interact with the sample and scatter over an angle 2θ. The scattered wave is characterized by the wavevector k' that has the same length as k in the case of elastic scattering. The scattered intensity is recorded on a 2D position-sensitive detector.

From Fig. 3.6 it can be seen that the length of the wavevector transfer $Q = k - k'$ is given by

$$\|Q\| = Q = \frac{4\pi}{\lambda_n}\sin(\theta) \approx \frac{2\pi r_d}{\lambda_n L_{sd}}, \tag{3.43}$$

where r_d is the distance of the scattered beam on the detector to the center of the direct beam and L_{sd} is the sample-to-detector distance (see Fig. 3.5).

The wavevector transfer Q is inversely proportional to a length $2\pi/Q$ which is characteristic for the scattering particles. When the particle size is relatively large compared to the neutron wavelength the scattering is predominantly found at small angles. The scattered intensity $I(Q)$ as a function of Q can generally be described as

$$I(Q) = \Phi_n^0 \Delta\Omega \eta_d T V \left(\frac{d\Sigma}{d\Omega}\right)(Q), \tag{3.44}$$

where Φ_n^0 is the incoming neutron flux, $\Delta\Omega$ the probed solid angle element, η_d the detector efficiency, T the sample transmission, and V the sample volume in the neutron beam. The macroscopic differential scattering cross-section $(d\Sigma/d\Omega)(Q)$ is the number of neutrons scattered per second into a small solid angle $d\Omega$. After correcting for the background scattering from the furnace and the sample holder, the macroscopic scattering cross-section of the sample can be deduced from the scattered intensity by eqn. (3.44).
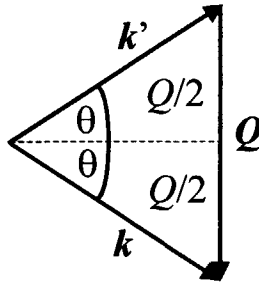

Fig. 3.6: Schematic drawing of the elastic scattering process. The incident and scattered waves are characterized by the wavevector k and k', respectively. The momentum transfer is $\hbar Q$, where Q is the wavevector transfer.

36

The macroscopic differential scattering cross-section characterizes the scattering power of the particles in the matrix. For a dilute system in which the homogeneous particles are not correlated and have a size distribution that differ only in their dimension and not in their shape, the macroscopic differential scattering cross-section is given by

$$\left(\frac{d\Sigma}{d\Omega}\right)(Q) = (\Delta\rho)^2 \int_0^\infty V_p(R) D_V(R) |F(Q,R)|^2 dR,$$ (3.45)

where $\Delta\rho = \rho_p - \rho_\gamma$ is the contrast in neutron scattering length density between the precipitates ρ_p and the austenite matrix ρ_γ. The scattering length of an atom can be regarded as the distance over which a neutron interacts with the nucleus of the atom. The scattering length density is the scattering length multiplied by the number density of the atom.

For spherical precipitates $V(R) = 4\pi R^3/3$ is the particle volume with radius R. $D_V(R)dR$ represents the volume fraction of precipitates with a radius between R and $R+dR$ for a particle volume distribution $D_V(R)$. The frequently used particle number distribution $D_N(V)$, where $D_N(V)dR$ represents the number of particles per unit volume with a radius between R and $R+dR$, is directly related to the particle volume distribution by $D_N(V) = D_V(R)/V(R)$. The form factor is given by

$$F(Q,R) = \frac{3[\sin(QR) - QR\cos(QR)]}{(QR)^3}$$ (3.46)

For small values of QR eqn. (3.46) can be approximated by a Taylor expansion

$$|F(Q,R)|^2 = \left[1 - \frac{(QR)^2}{10} + ...\right]^2 \approx \exp\left[-\frac{(QR)^2}{5}\right]$$ (3.47)

This is known as the Guinier approximation in which the Guinier radius is given by $R_G = (3/5)^{1/2}R$. For large values of QR Porod has shown that eqn. (3.46) approaches

$$|F(Q,R)|^2 \approx \frac{9}{2(QR)^4}.$$ (3.48)

Fig. 3.7 shows the dependence of $|F(Q,R)|^2$ on QR and the regions in which the Guinier and Porod approximations are valid.
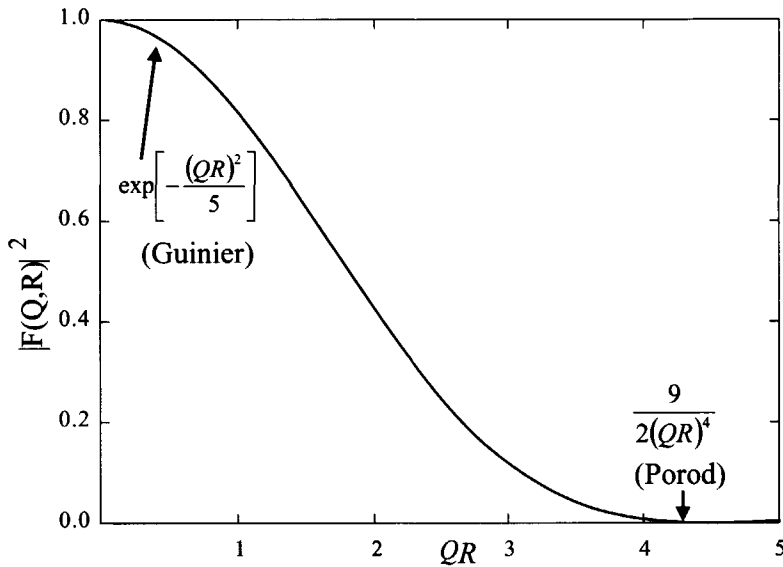
Fig. 3.7: The dependence of the form factor squared $|F(Q,R)|^2$ on QR. The regions in which the Guinier and Porod approximations are valid are indicated by arrows.

References

[1] M. Onink, F.D. Tichelaar, C.M. Brakman, E.J. Mittemeijer, and S. van der Zwaag, *J. Mat. Sci.*, 30 (1995) 6223.
[2] M. Militzer, *Science*, 298 (2002) 975.
[3] U. Lienert, H.F. Poulsen, and Å. Kvick, *Proc. 40th conference of AIAA on Structures, Structural Dynamics and Materials*, St. Louis (USA), April 1999, 2067.
[4] G.P. Krielaart, M.Th. Rekveldt, C.M. Brakman, and S. van der Zwaag, *Z. Metallk.*, 85 (1994) 709.
[5] S.G.E. te Velthuis, *Phase transformations in steel, a Neutron depolarization study*, PhD thesis, Delft University of Technology, 1999.
[6] E. M. Lauridsen, D. J. Jensen, H. F. Poulsen, and U. Lienert, *Scripta Mater.*, 43 (2000) 561.
[7] A.J. Allen, D. Gavillet, and J.R. Weertman, *Acta Metall. Mater.*, 41 (1993) 1869.
[8] R. Rosman, *Magnetic particles studied with neutron depolarization and small-angle neutron scattering*, PhD thesis, Delft University of Technology, 1991.
[9] P.Por, *Neutron depolarization in Magnetic recording materials*, PhD thesis, Delft University of Technology, 1995.
[10] M. de Jong, *A polarized neutron study of amorphous $Fe_{40}Ni_{40}B_{20}$: Internal stresses and structural relaxation*, PhD thesis, Delft University of Technology, 1996.
[11] W. Roest, *Magnetic flux in high-T_c superconducters: a Neutron depolarization*

study, PhD thesis, Delft University of Technology, 1995.

[12] N.H. van Dijk, L. Zhao, M.Th. Rekveldt, H. Frederikze, E. Brück, J. Sietsma, and S. van der Zwaag, in preparation.

[13] M.Th. Rekveldt, *Z. Phys.*, 259 (1973) 391.

[14] Rosman and M.Th. Rekveldt, *J. Magn. Magn. Mater.*, 95 (1991) 319.

[15] S.G.E. te Velthuis, N.H. van Dijk, M.Th. Rekveldt, J. Sietsma, and S. van der Zwaag, *Acta Mater.*, 48 (2000) 1105.

[16] A.S. Arrott and B. Heinrich, *J. Appl. Phys.*, 52 (1981) 2113.

[17] N.H. van Dijk, S.G.E. te Velthuis, M.Th. Rekveldt, J. Sietsma, and S. van der Zwaag, *Physica B*, 267-268 (1999) 88.

[18] S.G.E. te Velthuis, N.H. van Dijk, M.Th. Rekveldt, J. Sietsma, and S. van der Zwaag, *J. Appl. Phys.*, 89 (2001) 1275.

[19] R. Rosman and M.Th. Rekveldt, *Phys. Rev.*, B 43 (1991) 8437.

[20] L. Margulies, G. Winther, and H. F.Poulsen, *Science*, 292 (2001) 2392.

[21] B.C. Larson, Wenge Yang, G.E. Ice, J.D. Budal, and J.Z. Tischler, *Nature*, 415 (2002) 887.

[22] S. Kruijver, J. Sietsma, S.E. Offerman, N. van Dijk, L. Margulies, E.M. Lauridsen, S. Grigull, H.F. Poulsen, and S. van der Zwaag, *Steel Res.*, 73 (2002) 236.

[23] S.E. Offerman, N. H. van Dijk, J. Sietsma, S. Grigull, E. M. Lauridsen, L. Margulies, H. F. Poulsen, M. Th. Rekveldt, and S. van der Zwaag, *Science*, 298 (2002) 1003.

[24] H.F. Poulsen, S.F. Nielsen, E.M. Lauridsen, S. Schmidt, R.M. Suter, U. Lienert,

L. Margulies, T. Lorentzen, and D. Juul Jensen, *J. Appl. Cryst.*, 34 (2001) 751.

[25] E. M. Lauridsen, In *The 3D X-Ray Diffraction microscope and its application to the study of recrystallization kinetics*, PhD-thesis, 2001.

[26] L. Margulies, M.J. Kramer, R.W. McCallum, S. Kycia, D.R. Haeffner, J.C. Lang, and A.I. Goldman, *Rev. Sci. Instrum.*, 70 (1999) 3554.

[27] J. Als-Nielsen and D. McMorrow, In: *Elements of Modern X-ray Physics*, Wiley, West Sussex, 2001.

[28] B.E. Warren, In: *X-ray Diffraction*, Dover Publications, New York, 1990.

[29] B.D. Cullity and S.R. Stock, In: *Elements of X-ray Diffraction*, Prentice-Hall, New Jersey, 2001.

[30] S.M. King, In: *Modern Techniques for Polymer Characterization*, R.A. Pethrick and J.V. Dawkins eds., Wiley, 1999.

[31] G. Kostorz, In: *Treatise on Materials Science and Technology*, G. Kostorz Ed., Vol. 15, Academic Press, 1979.

[32] A.D. Sequeira, J.S. Pedersen, and G. Kostorz, In: *Modern Aspects of Small-Angle Scattering*, H. Brumberger Ed., Kluwer, 1995.

[33] L.A. Feigin and D.I. Svergun, In: *Structure Analysis by Small-Angle X-ray and Neutron Scattering*, Plenum Press, 1987.
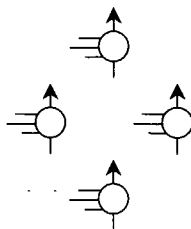
4. Ferrite/pearlite band formation in hot rolled medium carbon steel

S. E. Offerman, N. H. van Dijk, M. Th. Rekveldt, J. Sietsma, and S. van der Zwaag,

Abstract

The influence of the micro-segregation of Mn, Si, and Cr on the austenite decomposition during isothermal transformations in hot rolled medium carbon steel has been studied by neutron depolarization, electron probe micro analysis (EPMA), and optical microscopy. Eight specimens of the same alloy were held at 1173 K for 30 min and were rapidly cooled to different isothermal transformation temperatures. Two-dimensional EPMA maps of the specimen annealed at 1013 K showed that micro-segregation of alloying elements in hot rolled steel is strongly related to the ferrite/pearlite band formation. The local variations in alloying element concentration lead to variations in local transition temperatures, which were calculated with the thermodynamic database MTDATA®. Similar EPMA maps for the specimen transformed at 953 K demonstrate the presence of microchemical bands, while optical microscopy reveals the absence of microstructural bands. It is shown that the formation of microchemical bands is a prerequisite for band formation, but that the kinetics of the phase transformation determines the actual formation of microstructural bands. A quantitative model has been developed, which describes the observations in terms of the relative difference between ferrite nucleation rates in regions with a high and low local undercooling and the subsequent growth of the ferrite. The isothermal transformation experiments have led to generalized nucleation and growth criteria for the formation of microstructural bands.

4.1. Introduction

Ferrite/pearlite banding is a common phenomenon in hot rolled, low alloy steels, which has been known for more than forty years.[1,2] Recent studies reveal a renewed scientific and technological interest in the origin of microstructural banding.[3-6] The technological importance of ferrite/pearlite banding is related to the reduced resistance to hydrogen-induced cracking and the reduced impact toughness after an intercritical heat treatment and subsequent rapid cooling of these steels.[3] The scientific interest arises from the anisotropic behavior of steels with microstructural bands. A recent study showed the anisotropic dilatation of steels with ferrite/pearlite bands,[6] which significantly alters the interpretation of dilatometry experiments. It can be expected that microstructural bands also influence the interpretation of neutron depolarization (ND) experiments on the phase transformation in steel.[7]

Microstructural banding is the term used to describe a microstructure consisting of alternating bands of proeutectoid ferrite and pearlite (or martensite for dual phase steels). Banding mainly depends on three factors: the micro-segregation of alloying elements, the cooling rate (or in general the imposed temperature profile) during the transformation, and the austenite grain size. Großterlinden et al.[3] and Thompson and Howell[4] have shown by means of Electron Probe Micro Analysis (EPMA) that the ferrite/pearlite bands are strongly related to the micro-segregation of alloying elements. Removal of the micro-segregation of alloying elements by annealing for several hours at a high austenization temperature eliminates the microstructural bands. Both studies demonstrate that the occurrence of microstructural bands also depends on the cooling rate. A low cooling rate results in strong banding, while a high cooling rate results in the absence of bands. Microstructural banding does not occur when the austenite grain size is larger than two or three times the microchemical band spacing.[4] This result indicates the importance of the ferrite nucleation process, which predominantly takes place at the austenite grain boundaries. In steels with large austenite grains only a limited number of ferrite nucleation sites are available, which is not sufficient to form ferrite bands.

The sequence of events that results in the formation of bands starts with the solidification process. The alloying elements having partition coefficients less than unity (e.g. Mn, Si, S, P) are rejected from the first formed δ-ferrite dendrites, resulting in interdendritic regions of high solute content, which is retained during the transformation from δ-ferrite to austenite. Subsequent hot rolling in the austenitic condition leads to elongated high-solute regions. The variation in alloying element concentrations may cause an inhomogeneous distribution of the carbon in the austenite.[2] Certain elements (e.g. Mn and Cr) effectively attract carbon, while other elements reject carbon (e.g. Si). Due to its relatively high diffusivity, the carbon in the austenite can be distributed according to thermodynamic equilibrium. Calculations of Verhoeven[8] have shown that variations in Mn-concentration (ΔC_{Mn}) result in variations in carbon concentration (ΔC_C), which can significantly alter the local A_3-transition temperature. The variation in alloying element concentration by itself also raises (e.g. Si) or lowers (e.g. Mn and Cr) the A_3-transition temperature.

The ferrite starts to nucleate in the regions with a high A_3-transition temperature, which causes the carbon to redistribute. Entire grains of austenite transform to proeutectoid ferrite, which grows across austenite grain boundaries,[4] resulting in the so-called 'bamboo' structure. The carbon is piled up in regions with a low A_3-transition temperature. The increase in carbon content will lower the local A_3-transition temperature even further. Eventually, the composition in these regions becomes eutectoidic and pearlite can form if the temperature is below the A_1-transition temperature.

Despite the broad interest, mainly qualitative descriptions on the formation of bands can be found in literature. The first quantitative description of the formation of bands was given by Kirkaldy et al.,[2] who gave a semi-empirical expression for the critical cooling rate. Thirty years later Großterlinden et al.[3] developed a finite difference analysis to predict the distance a planar austenite/ferrite interface can move as a function of the cooling rate, and was able to predict a critical cooling rate for the steels studied. Little research has been done on the effect of isothermal transformations on the formation of microstructural bands, and hence there are no models that predict the formation of bands during annealing at a constant temperature.[9] The present research aims to provide such a model by quantifying nucleation and growth criteria for the isothermal austenite to ferrite phase transformation in steels showing micro-segregation of alloying elements.

4.2. Experimental

The hot rolled medium carbon steel used had the following chemical composition: Fe - 0.364C - 0.305Si - 0.656Mn - 0.014P - 0.021S - 0.177Cr - 0.016Mo - 0.092Ni - 0.226Cu - 0.017Sn (wt-%). Eight specimens of the same hot rolled medium carbon steel, of which the chemical composition is listed in Table 4.1, were heated in a nitrogen atmosphere to 1173 K and held for 30 min, in order to form a single-phase austenite structure. The specimens were cooled at a rate of 20 K/s to 953, 961, 975, 987, 1000, 1013, 1023, and 1031 K respectively, subsequently held there for approximately 4.5 hours, and then furnace cooled to room temperature. The specimen dimensions are $150 \times 10 \times 0.4$ mm^3, which is suitable for ND during isothermal transformation. The rolling direction is along the long axis of the specimen. The specimens were studied with optical microscopy and ND.

As part of a larger program on the kinetics of ferrite formation the isothermal transformation kinetics of this steel was investigated using ND. This ND technique has the intrinsic advantage over other techniques such as dilatometry that it not only provides the total ferrite fraction transformed, but also the average ferrite grain size.[10] In this work we make use of the fractional transformation data only. The ND measurements have been performed at the PANDA instrument at the nuclear reactor of the Interfaculty Reactor Institute. During the heat treatment, the transmission of a polarized monochromatic neutron beam, with a wavelength of $\lambda = 1.240 \pm 0.012$ Å, is directed along the short axis of the specimen and an external magnetic field of $\mu_0 H = 5.16$ mT is applied along the long axis of the specimen. The average rotation of the polarization vector of the neutron beam was measured during annealing, which yields the ferrite fraction in the specimen as a function of time.[7,11] The full results of the ND investigation on the ferrite formation kinetics will be published in a subsequent paper.

The micro-segregation of Mn, Si, and Cr in this steel has been studied with EPMA. Only the specimens that were annealed at 953 and 1013 K were investigated with this technique. The EPMA measurements have been performed on a JEOL JXA 8900R micro probe with a wavelength dispersive spectrometer. Two-dimensional scans were made with a step size of 2 μm over an area of 512×512 μm^2, which gives qualitative information about the local concentrations of Mn, Si, and Cr. Two additional sets of five line scans were taken with a step size of 3 μm over a distance of 300 μm, which give quantitative information about the local concentrations of Mn, Si, and Cr. The specimens were prepared for optical microscopy by grinding, polishing, and etching in 2% Nital for 20 s. Optical micrographs were taken of the areas studied with EPMA.

4.3. Results

The imposed temperature profile and the ferrite fraction f as a function of time, which was measured with neutron depolarization, are shown in Fig. 4.1 for the specimen that was annealed at 1013 K. The figure shows that only pro-eutectoid ferrite forms during the isothermal annealing stage. Pearlite starts to form below the A_1-transition temperature during continuous cooling to room temperature. Similar transformation characteristics were observed for the specimens that were annealed at 975, 987, 1000, 1023, and 1031 K. Figure 4.2 shows the distribution of Mn, Si, and Cr as measured with EPMA, compared to the final microstructure at room temperature. The figure shows that the pearlite bands coincide with the solute-rich regions, while the ferrite bands are present in the solute-lean regions. The average wavelength of the chemical bands is approximately 96 μm. The variation in alloy element concentration across several ferrite/pearlite bands of the specimen that was annealed at 1013 K is shown in Fig. 4.3. The minimum and maximum alloying element concentration that was measured with EPMA is given in Table 4.1. These concentration differences originated from the (partial) rejection of alloying elements during the early stages of δ-ferrite solidification.

Fig. 4.1: *The imposed temperature profile and the ferrite fraction f as a function of time, measured with neutron depolarization, for the specimen that was annealed at 1013 K.*
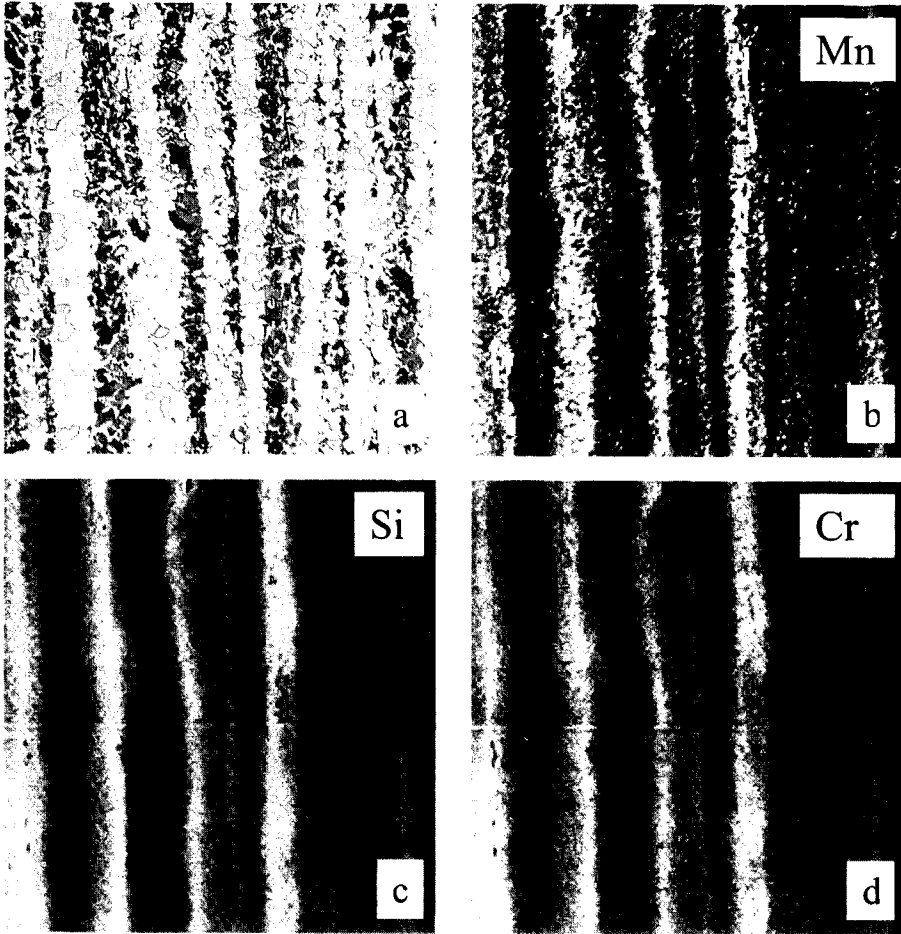
Fig. 4.2: Microstructure and the Mn-, Si-, and Cr-distribution (same area) of the specimen annealed at 1013 K. a) Optical micrograph of the area (512×512 μm^2) at which the 2D EPMA scans were taken; b) Mn distribution; c) Si distribution; d) Cr distribution. The light regions indicate a high concentration.

Table 4.1: The minimum and maximum concentration of the alloying element as measured with EPMA and calculated with MTDATA®

Element	MTDATA®	EPMA
Mn (wt.%)	0.50 – 0.88	0.57 – 0.87
Si (wt.%)	0.19 – 0.50	0.25 – 0.48
Cr (wt.%)	0.16 – 0.20	0.10 – 0.22

45

Fig. 4.3: Optical micrograph with EPMA-line-scan (white line, 300 μm), related to the Mn, Si, and Cr distribution and the calculated local variation in A₃, A₁⁺, and A₁⁻ temperatures with MTDATA® for the specimen annealed at 1013 K.

The imposed temperature profile and the ferrite fraction *f* as a function of time, which was measured with neutron depolarization, are shown in Fig. 4.4 for the specimen that was annealed at 953 K. The figure shows that the equilibrium fraction pro-eutectoid ferrite is formed within the first two minutes of the isothermal annealing stage. The complete transformation to pearlite takes place in the next three minutes. The only other specimen that showed similar transformation characteristics was the one annealed at 961 K.
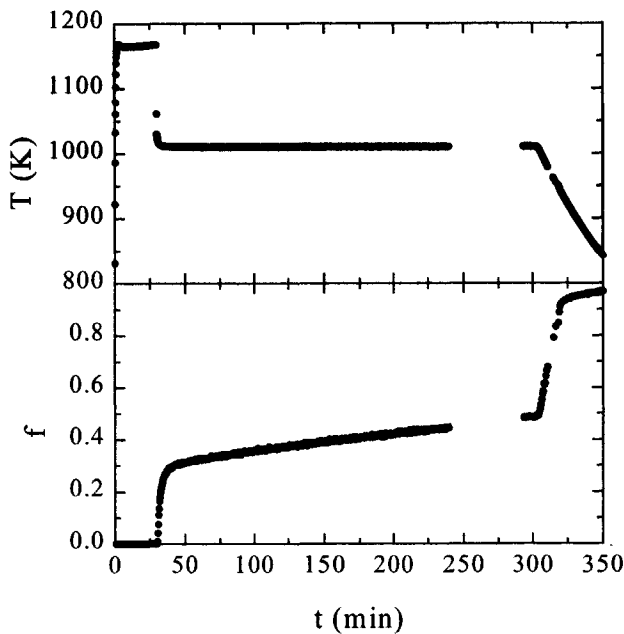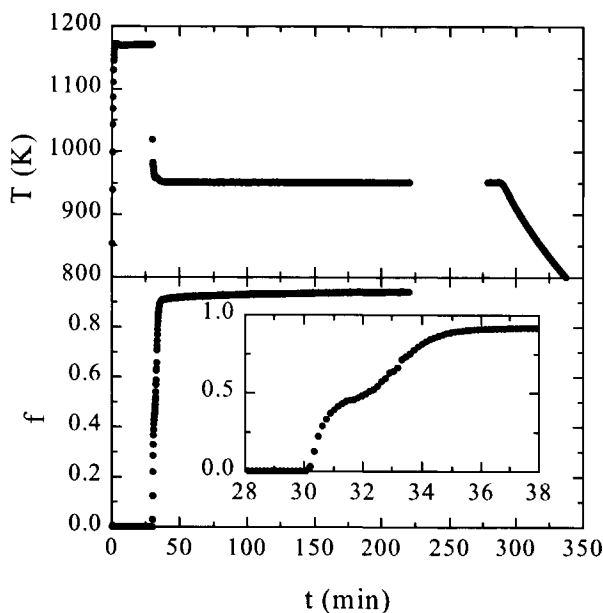
Fig. 4.4: The imposed temperature profile and the ferrite fraction f as a function of time, measured with neutron depolarization, for the specimen that was annealed at 953 K.

The equilibrium fraction of pro-eutectoid ferrite of this specimen was reached after seven minutes of isothermal annealing. The 2D-EPMA scans in Fig. 4.5 demonstrate the presence of chemical bands in the specimen annealed at 953 K, while the optical micrograph reveals the absence of ferrite/pearlite bands. Although it is hard to quantify the degree of banding,[12,13] it was concluded from the micrographs that for isothermal transformation temperatures of 961 K and higher, microstructural bands were observed. In Fig. 4.6 the concentration variations of the alloying elements across several ferrite/pearlite bands are shown for the specimen annealed at 953 K, which is essentially the same as the other specimen investigated by EPMA.
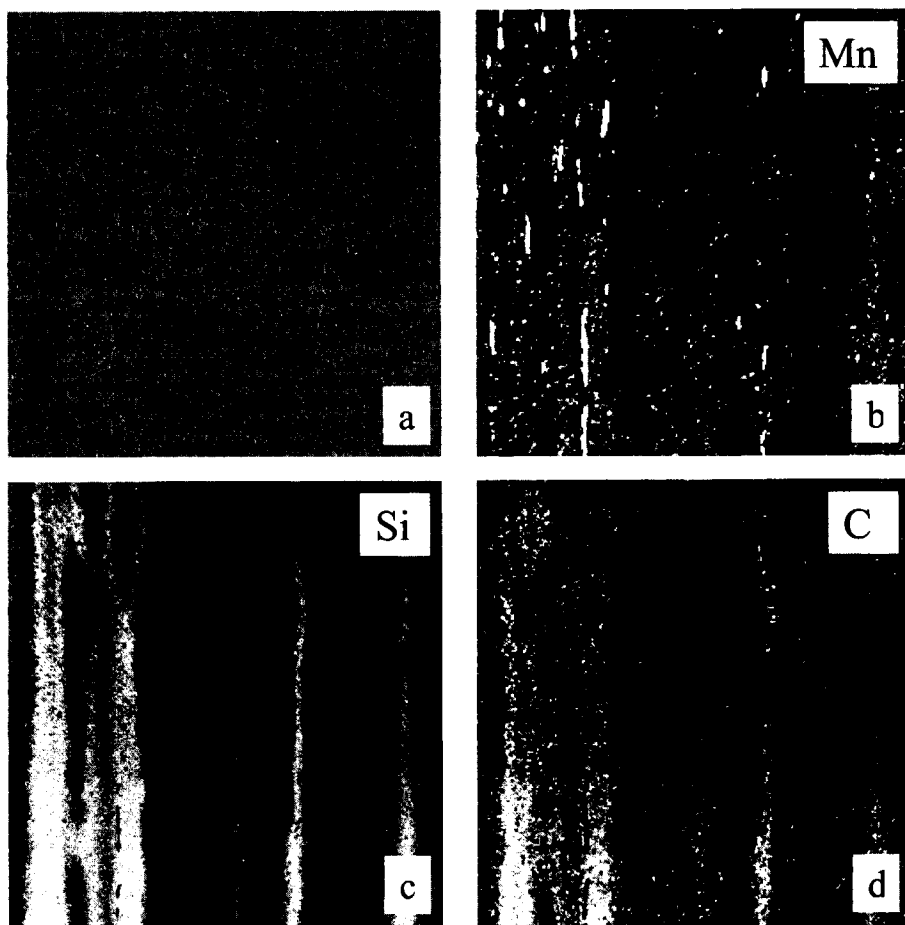
Fig. 4.5: Microstructure and the Mn-, Si-, and Cr-distribution (same area) of the specimen annealed at 953 K. a) Optical micrograph of the area (512×512 µm²) at which the 2D EPMA scans were taken; b) Mn distribution; c) Si distribution; d) Cr distribution. The light regions indicate a high concentration.
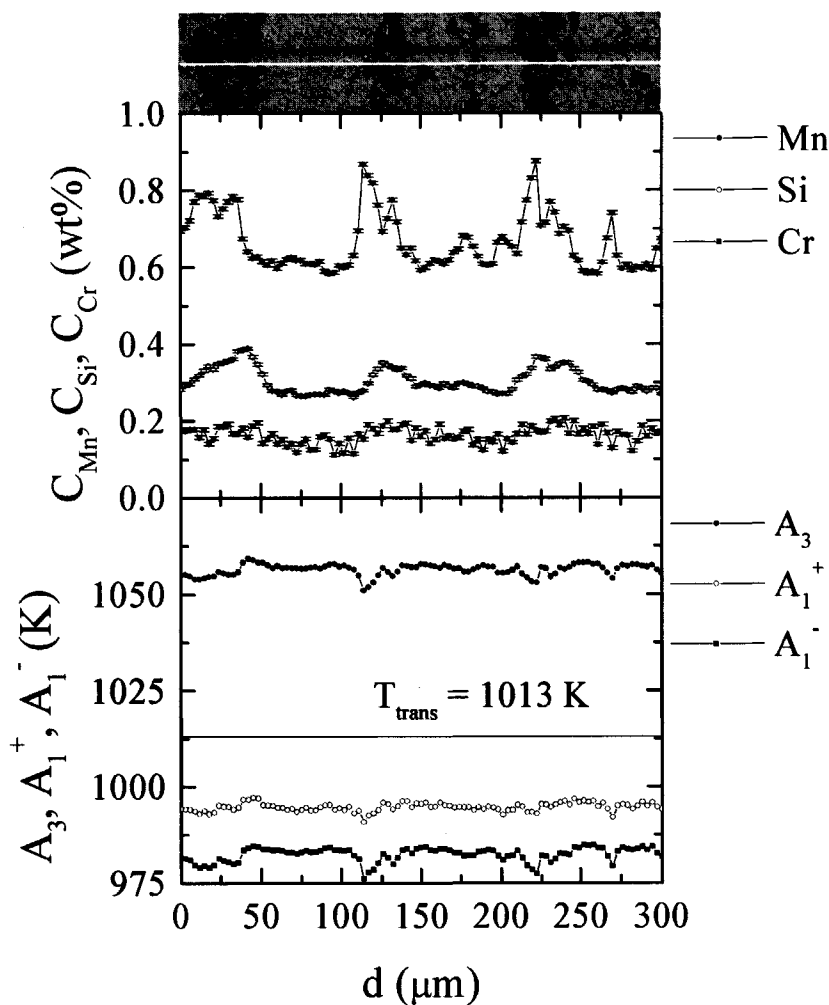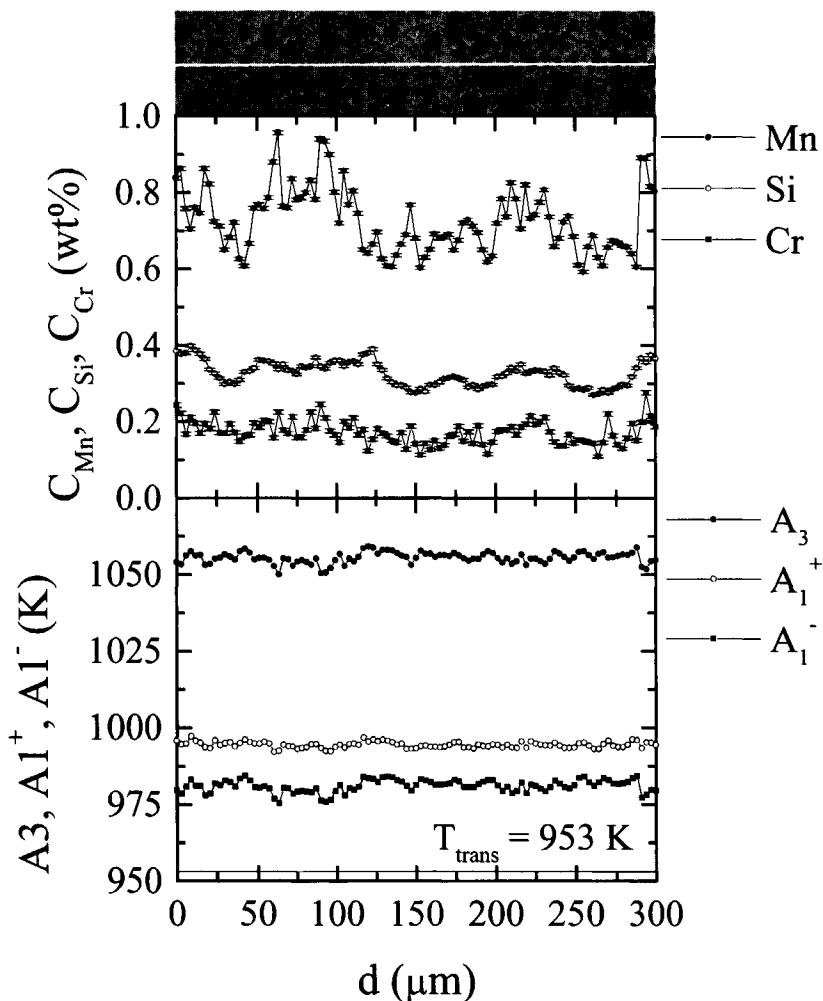
Fig. 4.6: Optical micrograph with EPMA-line-scan (white line, 300 μm), related to the Mn, Si, and Cr distribution and the calculated local variation in A_3, A_1^+, and A_1^- temperatures with MTDATA® for the specimen annealed at 953 K.

4.4. Discussion

DISTRIBUTION OF CARBON IN THE AUSTENITE

The minimum and maximum concentrations of Mn, Si, and Cr that result from the solidification process were calculated with MTDATA® and are given in Table 4.1. The calculated values (except the minimum concentration of Cr) agree well with the concentrations that were measured with EPMA. Based on the method developed by Brown

and Kirkaldy[14] and the observed concentration ranges (Table 4.1), we calculated the variation in carbon concentration in the austenite phase ΔC_C as a result of the Mn, Si and Cr segregation. The differences between the maximum and minimum in manganese (ΔC_{Mn}), silicon (ΔC_{Si}), and chromium (ΔC_{Cr}) concentration result in

$$\Delta C_C = 0.061\Delta C_{Mn} - 0.138\Delta C_{Si} + 0.156\Delta C_{Cr} \sim 0.005 \text{ wt.\%} \tag{4.1}$$

for a nominal carbon concentration of 0.364 wt.%. The influence of the Mn- and Cr-segregation on the variation in carbon concentration in the austenite is partly cancelled by the opposite effect of the Si-segregation for the given composition. Since ΔC_C is small in comparison to C_C, effectively, a homogeneous distribution of carbon in the austenite is present in our specimens, since the Mn, Si, and Cr are accumulated in the same regions.

LOCAL VARIATION IN THE TRANSITION TEMPERATURE

The local variation in the transition temperatures as a function of the Mn, Si, and Cr concentration was calculated with the thermodynamic database MTDATA®. Since the expected concentration variations of the other alloying elements are too small to significantly alter the transition temperatures for the given composition, they have not been measured and their nominal values were taken. The local transition temperature from austenite to ferrite, A_3, as calculated with MTDATA® for a carbon concentration of 0.364 wt.% has been fitted to a linear equation which is given by

$$A_3 = -23.56C_{Mn} + 26.58C_{Si} - 6.66C_{Cr} + 1065, \tag{4.2}$$

where the temperature is in K and the concentrations in wt.%.

Manganese and silicon have an opposite effect on the local A_3-transition temperature, with a magnitude that is of the same order. The local transition temperatures above (A_1^+) and below (A_1^-) the three-phase region are for a carbon concentration of 0.364 wt.% given by

$$A_1^+ = -15.45C_{Mn} + 19.64C_{Si} + 26.72C_{Cr} + 995, \tag{4.3}$$
and

$$A_1^- = -28.34C_{Mn} + 13.06C_{Si} + 13.26C_{Cr} + 995. \tag{4.4}$$

The variation in the local transition temperatures as shown in Figs. 4.3 and 4.6 for the specimens that were annealed at $T = 1013$ and 953 K respectively, were calculated with equations (4.2-4.4). The two specimens show, as expected, similar fluctuations in A_3-temperature ranging from 1051 to 1059 K. The former specimen has microstructural bands, while the latter specimen has not. This leads to the conclusion that the formation of ferrite/pearlite bands depends on both the presence of chemical bands and the isothermal transformation temperature. The formation of strong bands can already occur for relatively

50

small fluctuations of 8 K in the local A_3-temperature, as compared to fluctuations of 50 K that were found for the steels that were studied by Großterlinden et al.[3]

NUCLEATION AND GROWTH MODEL

The experimental data of Figs. 4.1-6 show that the formation of ferrite/pearlite bands depends on both the presence of chemical bands and the isothermal transformation temperature. The fundamental processes that govern the formation of bands are the ferrite nucleation and growth processes during the phase transformation. In this section the nucleation and growth criteria are derived that have to be fulfilled for the formation of bands.

In the classical nucleation theory, the rate of ferrite nucleation grain is given by[15,16]

$$\frac{\mathrm{d}N}{\mathrm{d}t} = N_n \frac{kT}{h} \exp\left(-\frac{\Delta G^* \lambda}{kT}\right) \exp\left(-\frac{Q_D}{kT}\right), \tag{4.5}$$

where N is the number of nuclei, N_n the number of potential nucleation sites, $k = 1.38 \cdot 10^{-23}$ J/K the Boltzmann constant, $h = 6.626 \cdot 10^{-34}$ Js Planck's constant, $\lambda = 10^{-4}$ a scaling factor,[17] Q_D the activation energy for self diffusion. The ferrite nucleation, which takes place at the austenite/austenite grain boundaries, is an important parameter in describing the formation of bands. An insufficient density of ferrite nucleation sites can prevent the formation of microstructural bands. It is of great importance to model the shape of the austenite grains accurately, since it determines the number of available nucleation sites. Van Leeuwen et al.[17] showed that the geometry of the austenite grain can be approximated by a tetrakaidecahedron. The energy barrier ΔG^* for nucleation on austenite/austenite grain boundaries in a tetrakaidecahedron is given by[18]

$$\Delta G^* = \frac{4(z_2 \gamma_{\alpha\gamma} - z_1 \gamma_{\gamma\gamma})^3}{27 z_3 \Delta G_V^2}, \tag{4.6}$$

where $\gamma_{\alpha\gamma}$ is the surface free energy of the austenite/ferrite-interface (0.6 J/m^2),[18] $\gamma_{\gamma\gamma}$ the surface energy of an austenite grain boundary (0.85 J/m^2),[18] and z_1, z_2, and z_3 are geometrical parameters that depend on the type of nucleation site in the austenite grain (boundary, edge or corner). For nucleation at the edge of a tetrakaïdecahedron $z_1 = 0.72$, $z_2 = 1.3$, and $z_3 = 0.096$.[18] The driving force for nucleation ΔG_V is determined via the parallel-tangent construction for an Fe-C-Mn system with standardized data from the Scientific Group Thermodata Europe (SGTE). The effect of the silicon and chromium concentrations on ΔG_V is taken into account by using an effective manganese concentration, which accounts for the effect of silicon and chromium on the A_3-transition temperature according to equation (2). The effective manganese concentration at the minimum and maximum A_3-transition temperature then becomes $C_{Mn,c} = 0.59$ wt.% and $C_{Mn,e} = 0.25$ wt.%, respectively.

The relative difference r between the ferrite nucleation rates in regions with the maximum and the minimum A_3-transition temperature is defined as

$$r = \frac{\left(\dfrac{dN}{dt}\right)_{A3\,max} - \left(\dfrac{dN}{dt}\right)_{A3\,min}}{\left(\dfrac{dN}{dt}\right)_{A3\,max}} = 1 - \exp\left(\frac{\lambda}{kT}\left(\Delta G^{*}_{A3\,max} - \Delta G^{*}_{A3\,min}\right)\right). \tag{4.7}$$

Figure 4.7 shows how the relative difference between the ferrite nucleation rates changes as a function of the isothermal transformation temperature in the case that $A_{3min} = 1051$ K in the solute-rich regions and $A_{3max} = 1059$ K in the solute-lean regions. In the figure the experiments are indicated by squares and the critical undercooling, which marks the transition between band formation and no band formation is indicated by a dashed line. The critical undercooling for this material is approximately 100 K.

The ferrite nucleation behavior largely differs for the two specimens investigated by EPMA. At 1013 K, the relative difference of the ferrite nucleation rate is $r = 0.80$. This means that 80% less nucleation events take place in the regions with the lowest A_3-temperature compared to regions with the highest A_3-temperature. The redistribution of the carbon (towards the regions with a low local transition temperature) during the phase transformation enhances the difference in nucleation rate even further. At 953 K the relative difference of the ferrite nucleation rate is only 6.4%. This indicates that the nucleation rate was approximately homogeneous in the specimen, and hence no ferrite/pearlite bands are formed.

The formation of microstructural bands does not only depend on the relative difference r of the ferrite nucleation rates between regions with the maximum and minimum A_3-transition temperature, but also on the distance d over which the carbon can diffuse in the austenite before the pearlite formation takes place. If the relative difference of the ferrite nucleation rates would be large enough to form microstructural bands, but the ferrite grains could not become large enough to fill the regions with a high A_3-temperature, microstructural bands could not form (or only partly). In these medium carbon steels the ferrite growth rate is dominated by the diffusion rate of carbon in the austenite. The distance over which the carbon can diffuse in the austenite can be approximated by

$$d \approx \sqrt{D_C^{\gamma} t}, \tag{4.8}$$

where t is the time in which the carbon can diffuse in the austenite before the pearlite formation takes place and D_C^{γ} is the diffusion coefficient of the carbon in the austenite, which depends on the temperature and the nominal carbon concentration. D_c^{γ} is given by[19]

$$D_C^{\gamma} = 4.53 \cdot 10^{-7}\left(1 + Y_C(1 - Y_C)\frac{8339.9}{T}\right)\exp\left\{-\left(\frac{1}{T} - 2.221 \cdot 10^{-4}\right)(17767 - 26436 Y_C)\right\}, \tag{4.9}$$

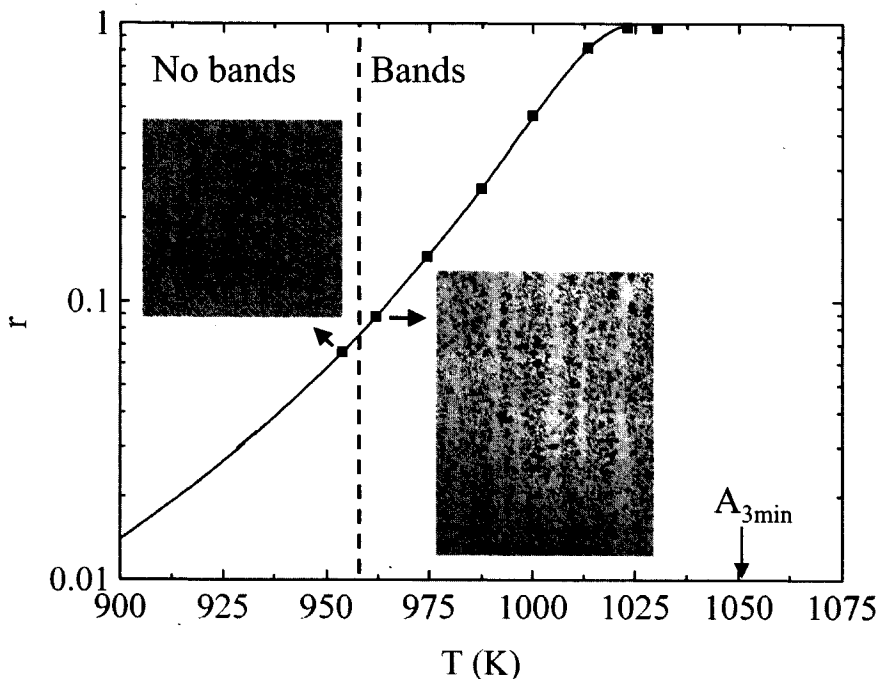where D_c^{γ} is in m^2/s and the temperature in K.

Fig. 4.7: The relative difference of the ferrite nucleation rate r as a function of isothermal transformation temperature in the case that A_{3min} = 1051 K in the solute-rich regions and A_{3max} = 1059 K in the solute-lean regions. The experiments are indicated by squares. The critical undercooling, which marks the transition between band formation and no band formation, is indicated by a dotted line. The photos show the microstructures of the specimens that were annealed at 953 (area of 512×512 μm^2) and 961 K (area of 420×550 μm^2).

The site fraction Y_C of carbon on the interstitial sub-lattice is given by

$$Y_C = \frac{x_C}{1-x_C}, \tag{4.10}$$

where x_C (= 0.016704) is the atom fraction of carbon in the alloy. The distance over which the carbon diffuses in the austenite before the pearlite formation takes place is shown in Fig. 4.8 for the eight specimens that were studied. For the specimens with an annealing temperature above (or equal to) the minimum A_1-transition temperature the time was taken to be 4.5 h. For annealing temperatures of T = 953 and 961 K, the time was taken to be t = 2 and 7 min respectively, which is the period of time between the onset of the ferrite formation and

53

the onset of the pearlite formation. As can be seen from this figure, there is a steep decrease in the distance over which the carbon diffuses, below the minimum A_1-transition temperature.

NUCLEATION AND GROWTH CRITERIA

The growth criterion can be established by considering that the ferrite nucleation predominantly takes place in the regions with a high A_3-temperature. The width of these regions is denoted by w, which does not have to be equal to half the wavelength of the chemical bands. The maximum distance d_c over which the carbon has to diffuse in order to form microstructural bands is then given by

$$d_c = \frac{1}{2}w.$$ (4.11)

The width w can be estimated from Fig. 4.2: $w \approx 60$ μm. As can be seen from Fig. 4.8, the growth criterion was fulfilled for all the specimens that were annealed above the minimum A_1-transition temperature. This criterion was not fulfilled for the specimens that were annealed at $T = 961$ and 953 K. However, the former specimen does exhibit microstructural banding (see Fig. 4.7), since the relative difference in ferrite nucleation rate is still significant at this undercooling. The overall nucleation rate in this specimen is so large that the equilibrium fraction pro-eutectoid ferrite is reached after 7 min, after which the pearlite formation starts. At annealing temperatures below the minimum A_1-transition temperature, the influence of the ferrite growth on the formation of microstructural bands can be neglected.

The specimen that was annealed at $T = 953$ K does not have microstructural bands (Fig. 4.5), since the relative difference in ferrite nucleation rate is too small at this temperature. The overall nucleation rate in this specimen is so large that the equilibrium fraction pro-eutectoid ferrite is reached within 2 min, after which the pearlite formation starts. This results in a critical value r_c for the relative difference of the ferrite nucleation rate, which is in the order of

$$r_c \approx 6 - 8 \%$$ (4.12)

If the austenite grain size is larger than 2-3 times the chemical band spacing, there will be too few nucleation sites available to result in a significant difference in ferrite nucleation rate between regions with a high and a low A_3-transition temperature. In hot rolled steel this is usually not the case. With the model developed in section 4.3, and the criteria established in this section, the formation of microstructural bands can be predicted for a given heat treatment and a given hot rolled medium carbon steel. The width w, which is needed as an input parameter for the model, depends on the solidification conditions and is found to depend on the primary dendrite arm spacing,[8] which could in principle be obtained from a solidification model. Another method is to slowly cool a piece of the steel under investigation from the austenite state to room temperature and obtain w from the width of the ferrite bands that have formed.

Since the criteria are expressed in nucleation and growth processes, they can in principle also be used for continuous cooling experiments. For a continuous cooling experiment an integrated nucleation rate and a growth have to be used.
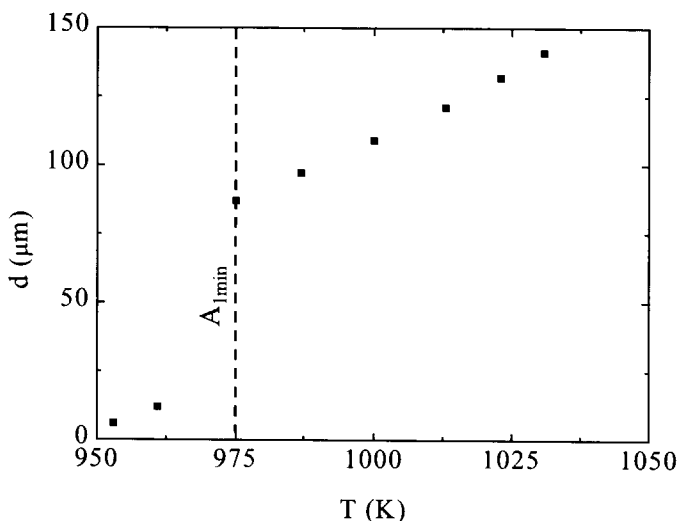

54

Fig. 4.8: The distance d over which the carbon diffuses in the austenite before the pearlite formation takes place for the eight specimens that are studied.

4.5. Conclusions

Two-dimensional EPMA-scans across several ferrite/pearlite bands show that microstructural banding in hot rolled medium carbon steel is related to the microchemical banding of manganese and silicon. The experiments show that the degree of banding decreases as the isothermal transformation temperature decreases, since the relative difference between the ferrite nucleation rates in regions with a low and a high A_3-transition temperature decreases. It is shown that the formation of microchemical bands is a prerequisite for band formation, but the kinetics of the phase transformation determines the actual existence of microstructural bands. A quantitative model has been developed, with which the formation of microstructural bands can be predicted. The nucleation and growth criteria that have to be satisfied in order to form microstructural bands are:

1. The relative difference between the ferrite nucleation rates in regions with the maximum and the minimum A_3-transition temperature should be larger than 6 - 8 %.
2. In the case that the annealing temperature is above the minimum A_1-transition temperature, the carbon has to diffuse over a critical distance larger than half the width of a region with a high A_3-temperature. At annealing temperatures below the minimum A_1-transition temperature, the influence of the ferrite growth on the formation of microstructural bands can be neglected.

Acknowledgements

References

1. P. G. BASTIEN: *J. Iron Steel Ins.*, 1957, **187**, 281.
2. J. S. KIRKALDY, J. von DESTINON-FORSTMANN, and R. J. BRIGHAM: *Can. Metall. Q.* 1962, **1**, 59.
3. R. GROβTERLINDEN, R. KAWALLA, U. LOTTER, and H. PIRCHER: *Steel research*, 1992, **63**, 331.
4. S. W. THOMPSON and P. R. HOWELL: *Mat. Sci. Techn.*, 1992, **8**, 777.
5. F. A. KHALID, M. FAROOQUE, A. UL HAQ, and Q. KHAN: *Mat. Sci. Techn.*, 1999, **15**, 1209.
6. T. A. KOP, J. SIETSMA, and S. van der ZWAAG: accepted by *J. Mat. Sci. Techn.*.
7. S. G. E. te VELTHUIS: *Ironmaking and Steelmaking*,1995, **1**, 81.
8. J. D. VERHOEVEN: *J. Mat. Eng . Perf.*, 2000, **9**, 286.
9. H. G. KIM and P. R. HOWELL: Proc. Int. Conf. on 'Solid-to-solid phase transformations', 183, 1994, Farmington, Pennsylvania, USA.
10. G. P. KRIELAART, M. Th. REKVELDT, C.M. BRAKMAN, and S. van der ZWAAG: *Z. Metallkd.*, 1994, **85**, 709
11. S. E. OFFERMAN, N. H. van DIJK, M. Th. REKVELDT, J. SIETSMA, and S. van der ZWAAG: *Physica B*, 2000, **276-278**, 868.
12. J. KOMENDA and R. SANDSTRÖM: *Mater. Char.*, 1993, **31**, 143.
13. A. FROM and R. SANDSTRÖM: *Mater. Char.*, 1998, **41**, 11.
14. L. C. BROWN and J. S. KIRKALDY: *Trans. Mat. Soc. AIME*, 1964, **230**, 223.
15. M. VOLMER and A. WEBER: *Z. Phys. Chem.*, 1925, **119**, 277.
16. R. BECKER and W. DÖRING: *Ann. Phys.*, 1935, **24**, 719.
17. Y. van LEEUWEN, S. I. VOOIJS, J. SIETSMA, and S. van der ZWAAG: *Metall. Mat. Trans. A*, 1998, **29A**, 2925.
18. P. J. CLEMM and J. C. FISCHER: *Acta Met.*, 1955, **3**, 70.
19. J. ÅGREN: *Scripta Metall.*, 1986, **20**, 841.
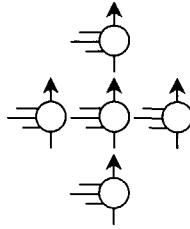
5. Evolving microstructures in carbon steel studied by neutron depolarization

5.1. 3D neutron depolarization experiments on the γ/α phase transformation in steel

S.E. Offerman, N.H. van Dijk, M.Th. Rekveldt, J. Sietsma, and S. van der Zwaag,

Abstract

Three-dimensional neutron depolarization experiments have been performed in order to study the isothermal phase transformation from austenite (γ-Fe) into ferrite (α-Fe) in medium-carbon steel. The polarization rotation during transmission through the sample is a measure of the ferromagnetic ferrite fraction, while the degree of depolarization determines the characteristic length scale of the ferrite microstructure. The application of a nickel coating is found to suppress ferrite formation at the surface, which allows for a direct analysis of the bulk transformation kinetics.

5.1.1. Experimental

The mechanical properties of medium-carbon steels strongly depend on their microstructure. Three-dimensional neutron depolarization experiments [1,2] provide a unique insight into the formation of this microstructure during the phase transformation from austenite (γ-Fe) into ferrite (α-Fe), as it is sensitive to both the fraction and the average grain size of the ferrite phase below the ferromagnetic transition temperature T_C = 1043 K [3,4]. The transmission of a polarized neutron beam through a sample is characterized by the depolarization matrix D according to P' = $D \cdot P$, where P and P' are the polarization vectors before and after transmission, respectively.

The experiments have been performed on two C45 steel samples (0.468 wt.% C, 0.715 wt.% Mn) with typical dimensions of $l \times b \times d$ = $10 \times 1.5 \times 0.04$ cm^3. In order to diminish the influence of enhanced ferrite nucleation at the surface, one of the samples was coated with a 7.6 μm thick nickel layer by means of electrochemical deposition. During the experiments, the transmission of the polarized monochromatic beam, with a wavelength of λ_n = 1.24 $\pm$ 0.012 Å, is directed along the short axis of the sample (d) and an external magnetic field of $\mu_0 H$ = 5.16 mT is applied along the long axis of the sample (l). After heating the sample for 30 minutes at 1175 K in pure nitrogen, in order to form single-phase austenite grains, the sample was cooled at a cooling rate of 20 K/s to 995 K and subsequently held at this temperature. The depolarization was measured during this isothermal anneal.

5.1.2. Results and discussion

From the measured depolarization matrix D the polarization rotation φ and the depolarization det(D) can be deduced, which are plotted in Fig. 5.1 for the steel samples with (C45 + Ni) and without (C45) a nickel coating. A clear difference is observed in the rotation and depolarization of both samples, which is consistent with the formation of a surface layer of ferrite with a thickness of 17 μm for the uncoated sample. The presence of such a surface layer was confirmed metallographically. The presence of the nickel coating suppresses decarburization and preferential ferrite formation on the surface.

The development of the ferrite fraction f and the mean ferrite grain radius δ of C45 + Ni is shown in Fig. 5.2. The rotation φ of the polarization vector is given by $\varphi = \eta c^{1/2} d \mu_0 <M>$, where η is a shape factor for the demagnetizing field of the sample, $c = 2.15 \times 10^{29} \lambda_n^2$ T^{-2}m^{-4}, and $<M>$ is the average magnetization of the sample. The shape factor $\eta = (1-f)\eta^P + f\eta^M$ is determined by a microscopic shape factor $\eta^P = 0.5$ of the ferrite grains and a macroscopic shape factor $\eta^M = 0.905$ of the sample [4]. The average magnetization inside a sample with a magnetic fraction f, a saturation magnetization M_s and an average reduced magnetization $<m_z>$, is given by $<M> = f <m_z> M_s$. For the temperature-dependent saturation magnetization M_s the value of pure iron [5] is used. The reduced magnetization $<m_z>$ = 0.63 is estimated from the fraction of pro-eutectoid ferrite as observed by optical microscopy of the final microstructure and the corresponding rotation. As shown in Fig. 5.2, the ferrite fraction f rapidly increases at the start of the transformation and grows slowly in the later stages.

The mean ferrite grain radius $\delta = <\rho^4>/<\rho^3>$, with ρ the radius of a spherical particle, can be evaluated from det(D) = $\exp\{-2cd\delta <(\Delta B)^2>\}$, where $<(\Delta B)^2> = \{3 - <m_z^2> - 2 f<m_z>^2\} f$ ($\mu_0 M_s)^2/4$ is the variance in the local magnetic induction along the transmission direction. Throughout the transformation δ (Fig. 5.2) is about 2.5 μm and seems to show a weak increase. The interpretation of the nucleation and growth kinetics is not unambiguous for the reported experiment.

58
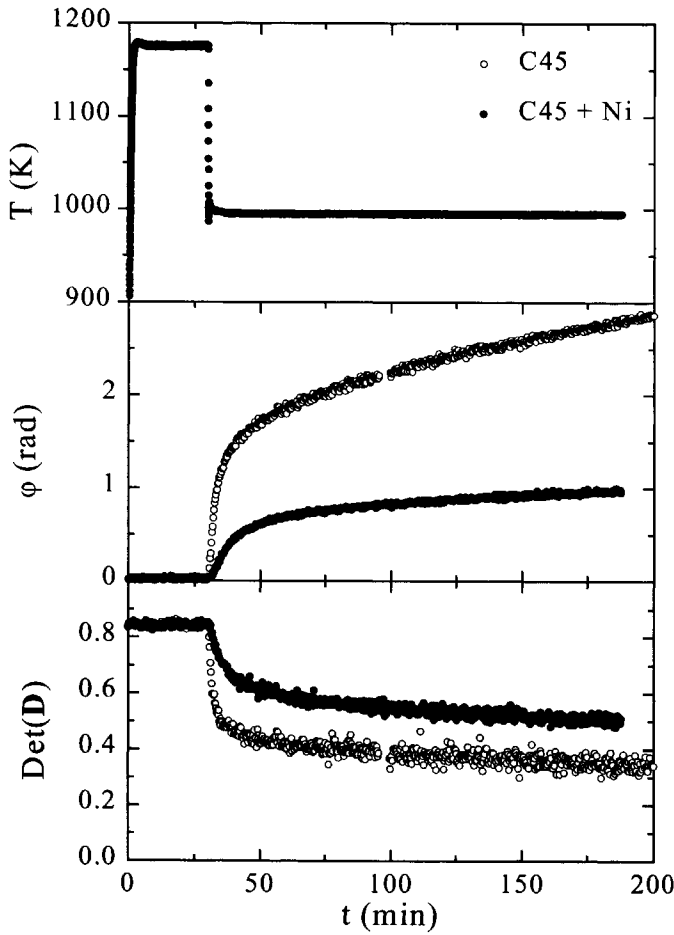
*Fig. 5.1: The temperature T, polarization rotation φ and depolarization det(**D**) as a function of time t for the isothermal transformation of C45 steel with (closed circles) and without (open circles) a nickel coating.*

It seems that the fast nucleation and growth processes at the early stage of the phase transformation changes into a ripening process [6]. The final ferrite nucleus density $n = f/(4/3)\pi\delta^3$, is about $2.0 \cdot 10^{15}$ nuclei m^{-3}.
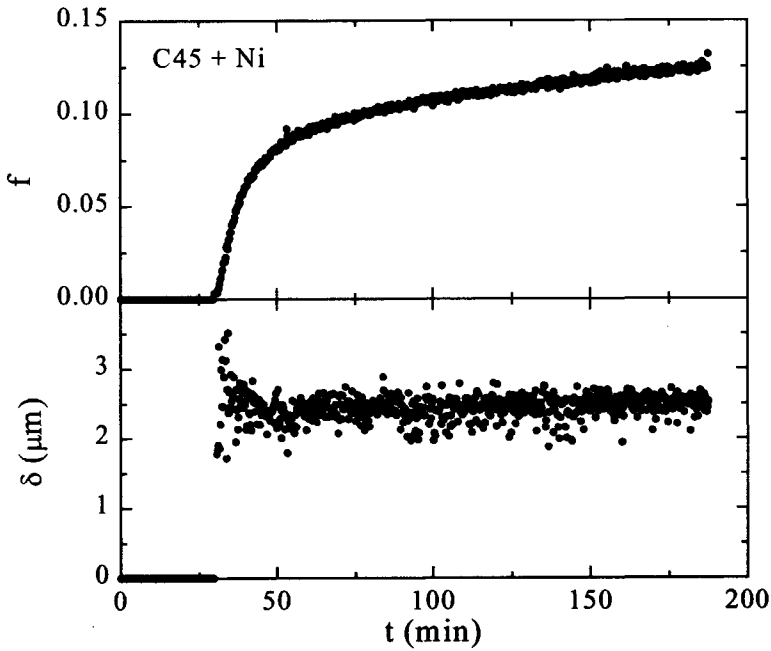
Fig. 5.2: The ferrite fraction f and the mean ferrite grain radius δ as a function of time t for C45 steel with a nickel coating.

References

[1]   M.Th. Rekveldt, Z. Phys. 259 (1973) 391.
[2]   R. Rosman and M.Th. Rekveldt, J. Magn. Magn. Mater. 95 (1991) 319.
[3]   S.G.E. te Velthuis, M.Th. Rekveldt, J. Sietsma, and S. van der Zwaag,
        Physica B 234-236 (1997) 1027; 241-243 (1998) 1234.
[4]   N.H. van Dijk, S.G.E. te Velthuis, M.Th. Rekveldt, J. Sietsma,
        and S. van der Zwaag, Physica B 267-268 (1999) 88.
[5]   N. Stüsser, M. Th. Rekveldt, and T. Spruijt, Phys. Rev. B 9 (1985) 5905.
[6]   S.G.E. te Velthuis, N.H. van Dijk, M.Th. Rekveldt, J. Sietsma, and S. van der
        Zwaag, to be published in Mat. Sci. Eng. A.

5.2. Neutron depolarization study of the austenite/pearlite phase transformation in steel

L.J.G.W. van Wilderen, S.E. Offerman, N.H. van Dijk, M.Th. Rekveldt, J. Sietsma, and S. van der Zwaag, *Appl. Phys. A*, 74 (2002) S1052 - S1054.

Abstract

Three-dimensional neutron depolarization experiments have been performed to study in-situ the isothermal phase transformation from austenite to pearlite in eutectoid steel. The interaction between the polarized neutron beam and the pearlite colonies (alternating plates of ferromagnetic ferrite and paramagnetic cementite) yields information about the fraction of pearlite and the average magnetic particle size. A comparison is made between neutron depolarization and dilatometry experiments, resulting in the introduction of a variable reduced magnetization during the transformation, which corresponds to the evolution of the magnetic structure from isolated pearlite colonies, via a transition region, to an interconnecting network.

5.2.1. Introduction

The kinetics of the phase transformations in steel has a large influence on the final microstructure and, as a consequence, on the mechanical properties of steel. A better understanding of the nucleation and growth processes contributes to the development of tailor-made steels. The Neutron Depolarization technique (ND) [1, 2] makes it possible to study the transformation from paramagnetic austenite (γ) into ferromagnetic pearlite (p), as it probes the fraction and mean magnetic particle size of the ferromagnetic phase [3]. No other technique capable of determining these two parameters in-situ has been reported so far, making it a powerful tool for the study of phase transformations in bulk ferromagnetic materials. The aim of this research is to relate the magnetic structure to the evolving microstructure. Previous ND studies have focused on the austenite to ferrite phase transformation in medium-carbon steel [3–6].

5.2.2. Experimental

The composition of the presently studied nearly eutectoidic steel is 0.715 wt.%C, 0.611wt.%Mn, 0.266 wt.%Cr and 0.347 wt.% Si. The sample with dimensions $100\times15\times 0.4$ mm^3 has a nickel coating of approximately 15 μm to avoid decarburization [6].

The transmission of a monochromatic polarized neutron beam through the sample is characterized by the depolarization matrix D according to $P' = DP$, where P and P' are the polarization vectors before and after transmission, respectively. The rotation of the polarization vector is a measure for the magnetic volume fraction and the degree of depolarization is a measure for the average magnetic domain size. The rotation of the polarization vector is given by $\varphi = \eta Lc^{1/2}<B>$, where η is a shape factor for the demagnetizing field of the sample, $L = 0.4$ mm denotes the thickness of the sample, $c = 2.15\times10^{29} \lambda_n^2$ $T^{-2}m^{-4}$, and the neutron wavelength $\lambda_n = 1.24\pm0.01$Å. The average magnetic induction inside the sample is given by $<B> = f^{nd}<m_z>\mu_0 M_s^p$, where f^{nd} is the volume fraction pearlite as determined with ND, $<m_z>$ is the average reduced magnetization in the direction

61

of the applied magnetic field (5.16 mT) along the long axis of the sample. The saturation magnetization of pearlite M_s^P can be calculated from the saturation magnetization of ferrite M_s^α multiplied by the equilibrium volume fraction of ferrite f^α inside a pearlite colony. f^α is evaluated with the thermodynamic database MTDATA® and determined to be 0.917. The shape factor which accounts for the effect of stray fields $\eta = (1-f^{nd})\eta^P + f^{nd}\eta^M$ is determined by a microscopic shape factor of $\eta^P = 0.5$ for microscopic spherically shaped particles and a macroscopic shape factor of $\eta^M = 0.905$ for our macroscopic plate-like sample [5].

The depolarization of the polarized neutron beam is caused by local variations in the magnetic induction $<(\Delta B)^2>$ inside the sample, and can be characterized for spherical particles by $det(D) = \exp\{-2cL\delta<(\Delta B)^2>\}$. The average magnetic particle radius δ can be evaluated from the experimentally determined depolarization matrix D and model equations for $<(\Delta B)^2>$ [2, 3].

With additional dilatometry experiments the fractions pearlite and austenite can be determined, by measuring the macroscopic length change of the sample (a cylinder with a length of 10 mm and a diameter of 3 mm) during the transformation. The experiments are performed on a Bähr 805a dilatometer under a vacuum of 10^{-4} mbar to prevent decarburization. The fraction pearlite f can be deduced from $f^{dl} = (l - l^\gamma)/(l^P - l^\gamma)$, where l is the observed length, and l^γ and l^P are the extrapolated lengths of the single-phase austenite and pearlite at the measured temperature [7].

The samples are annealed at 1173K for 0.5 h, subsequently cooled with 20 K/s (ND) or 10 K/s (dilatometry) to 953, 948, or 943 K and held there for 1 h. Different temperatures are studied to determine the influence of the degree of undercooling on the transformation rate.

5.2.3. Results and discussion

In Fig. 5.3 the fraction pearlite $f^{nd,c}$ is shown for three ND measurements as a function of time. The fraction curves are obtained from the experimental polarization rotation φ by assuming a constant $<m_z>$ of 0.74. For comparison the pearlite fraction as determined from dilatometry f^{dl} is shown. The value for $<m_z>$ is independently determined at the end of the transformation from field-dependent ND measurements [3] and gives the appropriate pearlite fraction $f^{nd,c} = 1$ at the end of the transformation. The pearlite fraction curve as measured with ND has a different shape from the curve measured with dilatometry. This suggests that $<m_z>$ is not constant but depends on the pearlite fraction. As $\varphi \propto f\langle m_z \rangle$ we can deduce the fraction-dependent $<m_z>$ from the experimental polatization rotation and the time-scaled pearlite fraction determined from dilatometry.

The ratio between the ND and dilatometer fraction curve, which is "time scaled" to the same temperature, determines the change in $<m_z>$ as a function of the fraction pearlite as determined with dilatometry f^{dl} (shown in Fig. 5.4). In the application of the two experimental techniques, systematic errors in the actual temperature may have occurred. Such differences, caused by different thermocouples and temperature distributions within the sample, may lead to an apparent shift on a logarithmic time scale (see Fig. 5.3).
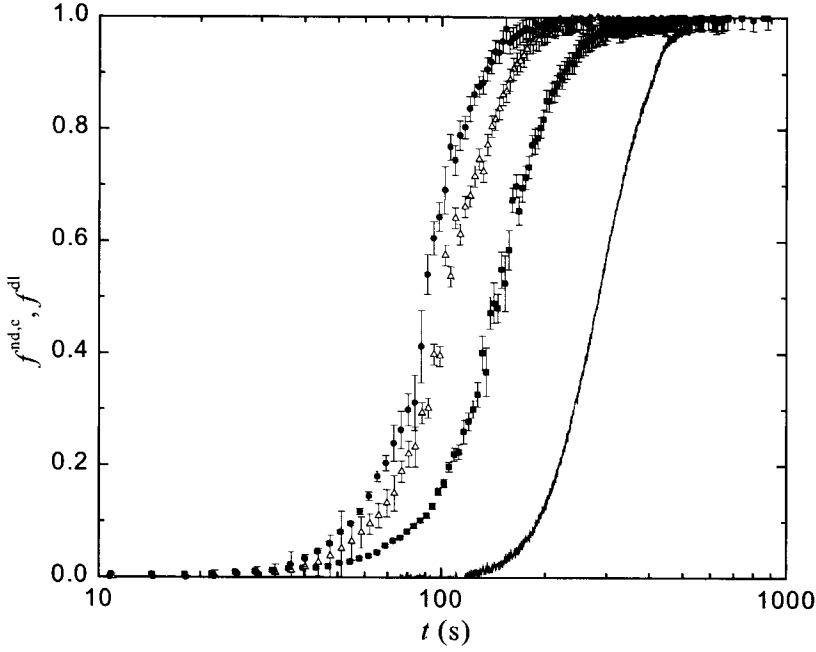
Fig. 5.3: Fraction pearlite as a function of time for ND measurements ($f^{nd,c}$) isothermally transformed at 943 ($\bullet$), 948 ($\triangle$), and 953 K ($\blacksquare$) calculated with a constant $<m_z> = 0.74$. For comparison the pearlite fraction (f^{dl}) determined from a dilatometry measurement, isothermally transformed at 953 K is shown (solid line).

From the temperature dependence of the transformation times in Fig. 5.3, the observed factor of approximately 1.5 in time scale corresponds to a temperature difference of about 5 K. To correct for the apparent temperature difference, the time scale for the dilatometry experiment is multiplied by a factor chosen to optimize the fit with the ND measurement for $f^{nd} > 0.8$, since $<m_z>$ is expected to be constant at large fractions.

In Fig. 5.4 three regimes can be distinguished, corresponding to isolated multidomain colonies ($f^{dl} < 0.3$), a transition region, and a region ($f^{dl} > 0.8$) corresponding to an interconnecting network of pearlite colonies. The first plateau with a constant $<m_z>$ up to $f^{dl} \approx 0.3$ reflects the presence of multidomain pearlite colonies. A pearlite colony effectively consists of two interpenetrating single crystals of ferrite and cementite in which the alternating plates from either phase in a colony have the same crystallographic orientation and each phase forms a continuous network via bending and branching of the plates. The formation of a domain wall in or perpendicular to the plates is energetically favorable due to the reduction of stray field energy, resulting in a low value for $<m_z>$.
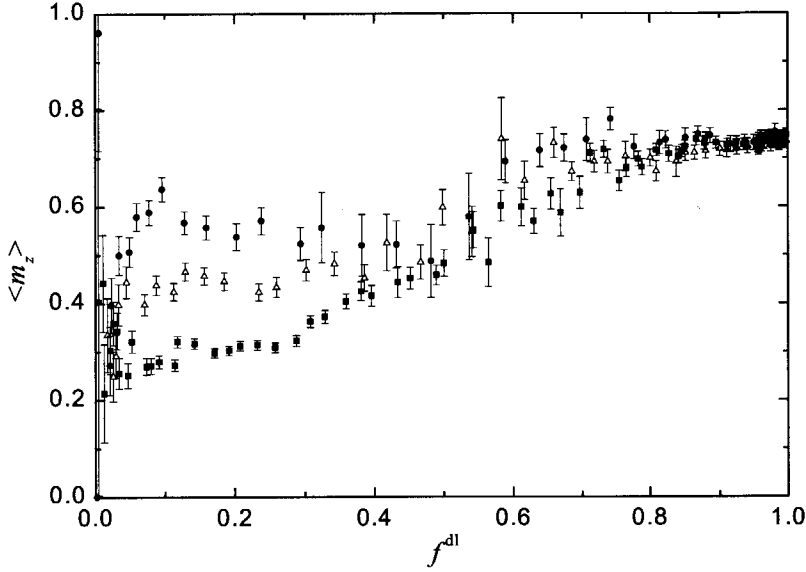
Fig. 5.4: Reduced magnetization <m$_z$> for isothermal transformations at 943 (●), 948 (Δ), and 953 K (■) as a function of the fraction pearlite determined from dilatometry f^{dl}. The value of <m$_z$> is calculated from the experimental polarization rotation φ and the time-scaled fraction curve from the dilatometry measurement.

The transition point at f^{dl} ≈ 0.3 forms the onset of an alignment of the magnetic domains in neighboring colonies in the direction of the applied field, thereby increasing the value of <m$_z$>. The value of f^{dl} ≈ 0.3 corresponds to the so called magnetic percolation threshold for heterogeneous magnetic materials, representing the concentration of magnetic material at which interactions between different magnetic particles cause a significant change in the macroscopic magnetic properties, e.g. a significant increase in the susceptibility [8].

The second transition point occurs at f^{dl} ≈ 0.8, when the pearlite colonies form a completely interconnected network, and the neighboring colonies align each other in the direction of the applied field. The shape anisotropy of the lamellae prevents a complete alignment. The (almost) completely transformed material now forms an assembly of randomly oriented magnetic plates with <m$_z$> ≈ 0.74, which is close to the theoretical value of <m$_z$> = π/4 in low fields [9]. The value for the observed second transition point corresponds to the concentration limit for which the sample starts to exhibit magnetic behavior as found to occur in dense polycrystalline magnetic materials, as demonstrated with susceptibility measurements [8]. The first plateau in Fig. 5.4 shifts to higher values for <m$_z$> for larger undercoolings.
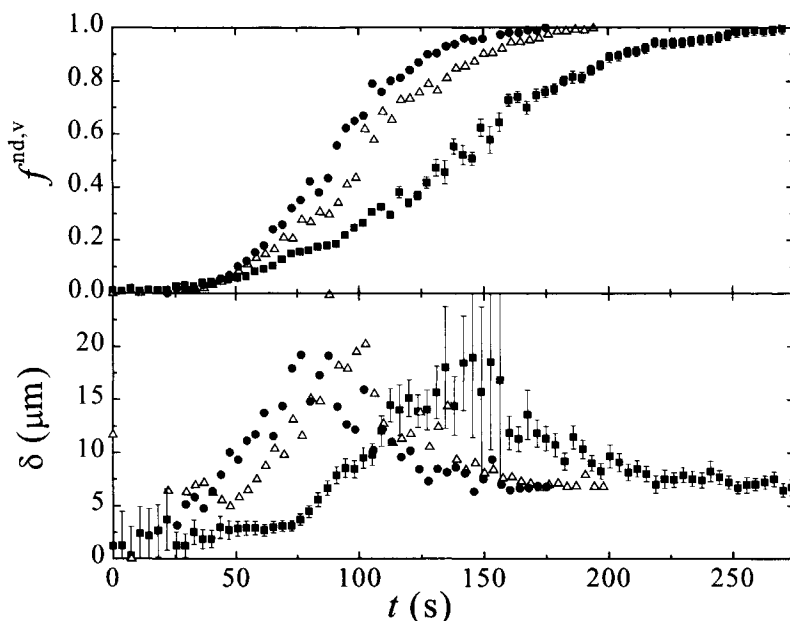
Fig. 5.5: Fraction pearlite $f^{nd,v}$ and average magnetic particle radius δ as a function of time for isothermal transformations at 943 ($\bullet$), 948 ($\triangle$), and 953 K ($\blacksquare$), calculated with a variable $<m_z>$. For clarity reasons only the error bars at 953 K are shown. Comparable errors are observed for the other two temperatures.

A higher degree of undercooling increases the nucleation rate, and a possible preferential nucleation in the direction of the applied magnetic could account for the observed behavior.

From the variable reduced magnetization as shown in Fig. 5.4, the corrected ND fraction curves $f^{nd,v}$ and the average magnetic particle radius δ as measured with ND are determined and plotted in Fig. 5.5 as a function of time. The average particle radius δ is observed to increase for all curves until $f^{nd,v} \approx 0.5$, after which it decreases somewhat to remain constant at $\delta \approx 6$ µm. The fraction curves in Fig. 5.5 demonstrate the effect of an increased undercooling, and show that higher degrees of undercooling lead to a faster completion of the austenite/pearlite transformation. It is interesting to mention that the ND-curve keeps rising slowly long after the transformation is supposed to be completed (not shown), indicating small changes in $<m_z>$, and as a consequence in the microstructure, on a relatively long time scale. The dilatometer experiments are insensitive for these changes in the (magnetic) microstructure.

The observed peak in the particle radius at $f^{nd,v} \approx 0.5$ as shown in Fig. 5.5, is probably caused by an extra depolarization due to variations in the magnetic path length [2], caused by clustering of pearlite colonies. Note the large error bars around $f^{nd,v} \approx 0.5$, which are caused by an almost complete depolarization of the beam. The final average pearlite colony radius as determined from optical micrographs is estimated to be 12 µm, and is twice the size observed

65

with ND. The presence of multidomains with small orientation differences inside a pearlite colony could explain the observed behavior.

At larger undercoolings a faster increase in particle size due to an increased growth rate of a pearlite colony is observed (see Fig. 5.5).

The nucleus density at low fractions is approximated by $n = 3f/4\pi\delta^3$, and determined to be of the order of 10^{15} m^{-3}. In conclusion, from the difference between the fraction curves as determined from ND measurements analyzed with a constant $<m_z>$ and dilatometry measurements, a variable reduced magnetization during the transformation has been deduced. The observed fraction dependence of the reduced magnetization is in agreement with the magnetic percolation theory. A transition from isolated pearlite colonies to an interconnecting network is observed. The ND-technique can be used to study the evolving magnetic structure during the austenite to pearlite transformation by taking into account a variable reduced magnetization.

Acknowledgements

References

[1] M.Th. Rekveldt: Z. Phys. **259**, 391 (1973)

[2] R. Rosman, M.Th. Rekveldt: J. Magn. Magn. Mat. **95**, 319 (1991)

[3] S.G.E. te Velthuis, N.H. van Dijk, M.Th. Rekveldt, J. Sietsma, S. van der Zwaag: Acta Mater. **48**, 1105 (2000)

[4] S.G.E. te Velthuis, M.Th. Rekveldt, J. Sietsma, S. van der Zwaag: Phys. B **234–236**, 1027 (1997); **241–243**, 1234 (1998)

[5] N.H. van Dijk, S.G.E. te Velthuis, M.Th. Rekveldt, J. Sietsma, S. van der Zwaag: Physica B **267–268**, 88 (1999)

[6] S.E. Offerman, N.H. van Dijk, M.Th. Rekveldt, J. Sietsma, S. van der Zwaag: Physica B **276–278**, 868 (2000)

[7] Th. Kop, J. Sietsma, S. van der Zwaag: J. Mater. Sci. **36**, 519 (2001)

[8] J.-L. Mattei, A.M. Konn, M. Le Floc'h: IEEE Trans. Instrum. Meas. **42**, 121 (1993)

[9] E.C. Stoner, E.P.Wohlfart: Philos. Trans. R. Soc. London **240**, 599 (1948)

5.3. Cluster formation of pearlite colonies during the austenite/pearlite phase transformation in eutectoid steel

S.E. Offerman, L.J.G.W. van Wilderen, N.H. van Dijk, M.Th. Rekveldt, J. Sietsma, and S. van der Zwaag, *Physica B*, 335 (2003) 99 - 103.

Abstract

Three-dimensional neutron depolarization experiments were performed to study in-situ the isothermal phase transformation from austenite to pearlite in the bulk of nearly eutectoid steel. It is shown that the spatial distribution of the magnetic domains gradually changes from random at the start to non-random half way the transformation, due to the cluster formation of pearlite colonies. The measured magnetic domain size can be related to the average distance over which the ferrite plates are parallel in a pearlite colony.

5.3.1. Introduction

The mechanical properties of steel strongly depend on the microstructure, which is formed during the phase transformations at high temperatures (900–1200 K) during the production process. Three-dimensional Neutron Depolarization (3DND) experiments [1,2] provide a unique insight into the formation of this microstructure as it probes the fraction and mean magnetic particle size of the forming ferromagnetic phase in a paramagnetic matrix [3]. No other technique capable of determining these two parameters in-situ and simultaneously has been reported so far, making it a powerful tool for the study of phase transformations in the bulk of ferromagnetic materials.

During the so-called eutectoid transformation, the austenite phase (FCC iron) is transformed into a mixture of ferrite (BCC iron) and cementite (orthorhombic Fe_3C). The resulting lamellar structure of ferrite and cementite is known as pearlite. A pearlite colony effectively consists of two interpenetrating single crystals of ferrite and cementite. On a local scale the structure of the pearlite colony is lamellar, but the ferrite and cementite plates can bend and branch, while the crystallographic orientation is conserved [4]. The measured magnetic domain structure is only related to the ferrite phase, since the austenite and cementite phases are paramagnetic at these elevated temperatures.

The present paper is a continuation of a previous paper on the austenite/pearlite transformation in the same steel [5]. The previous paper reported about a change in the reduced magnetization during the phase transformation, which was related to a transition from isolated magnetic domains into an interconnected network of magnetic domains. The aim of this research is to study the cluster formation of pearlite colonies by relating the measured magnetic domain structure to the evolving microstructure.

5.3.2. Neutron depolarization

The transmission of a monochromatic polarized neutron beam through the sample is characterized by the depolarization matrix D according to $P' = D \cdot P$, where P and P' are the polarization vectors before and after transmission, respectively. The rotation of the polarization vector is a measure for the magnetic volume fraction and the degree of depolarization is a measure for the average magnetic domain size.

67

The rotation φ of the polarization vector is related to the volume fraction pearlite f_p via $\varphi = \eta L c^{1/2} <B>$, where L is the thickness of the sample, $c = 2.15 \times 10^{29} \lambda^2$ T^{-2}m^{-4}, and $\lambda = 0.124 \pm 0.0012$ nm the neutron wavelength. The average magnetic induction inside the sample is given by $<B> = f_p <m_z> \mu_0 M_s^P$, where $<m_z>$ is the average reduced magnetization in the direction of the applied magnetic field (5.16 mT) along the long axis of the sample. The saturation magnetization of pearlite M_s^P can be calculated from the saturation magnetization of ferrite M_s^α [6] multiplied by the equilibrium volume fraction of ferrite f_α inside a pearlite colony. f_α is evaluated with the thermodynamic database MTDATA® and determined to be 0.90. The shape factor which accounts for the effect of stray fields $\eta = (1-f_p)\eta^P + f_p\eta^M$ is determined by a microscopic shape factor of $\eta^P = 0.5$ for microscopic spherically shaped particles and a macroscopic shape factor of $\eta^M = 0.905$ for our macroscopic plate-like sample [7].

The depolarization of the polarized neutron beam described by det(D), is caused by local variations in the magnetic induction $<(\Delta B)^2>$ inside the sample, and can be characterized for spherical particles by det(D) = $\exp\{-2cL\delta<(\Delta B)^2>\}$. The average magnetic particle radius δ can be evaluated from the experimentally determined depolarization matrix D and model equations for $<(\Delta B)^2>$, which depends on f_p [2,3]. The measured depolarization can be written as det(D) = $D_\perp^2 D_{//}$, where $D_\perp$ and $D_{//}$ are the components of the depolarization matrix D, which are perpendicular and parallel to the applied magnetic field, respectively.

In the case that the magnetic particles are not randomly distributed over the sample, then an extra depolarization of the neutron beam will arise, which is not related to the magnetic domain size. This extra depolarization will affect all the D-elements that are perpendicular to the applied magnetic field, while the component that is parallel to the magnetic field remains unaffected. In order to deduce the average magnetic domain size the perpendicular component $D_\perp$ then needs to be corrected by a factor [8]:

$$D_c = \int_0^\infty f(N)\cos\left[(N - \langle N \rangle)\varphi_p\right]dN,$$

where $f(N)$ is the normalized spatial distribution function of the number of particles along a neutron path N, $<N>$ is the average number of particles along the neutron path, and φ_p is the average rotation per domain. The rotation φ of the polarization vector is not influenced by the manner in which the magnetic domains are distributed.

5.3.3. Experimental

The composition of the presently studied nearly eutectoid steel is (in wt%): 0.715 C, 0.611 Mn, 0.266 Cr, 0.347 Si, 0.012 P, 0.03 S, 0.094 Ni, 0.235 Cu, 0.021 Mo, 0.025 Sn, and the rest is Fe. The sample for the 3DND-experiments with dimensions $100 \times 15 \times 0.4$ mm^3 is coated with a nickel layer of approximately 15 μm thickness to avoid decarburization. The sample was annealed at 1173 K for 0.5 h, subsequently cooled with 20 K/s to 943 K, and held there until the transformation was finished. This temperature cycle was repeated with the same sample for transformation temperatures of 948 and 953 K in order to study the influence of the degree of undercooling on the transformation kinetics.

In order to relate the magnetic structure to the microstructure, ex-situ quench-measurements were performed on four 10 mm long cylinders with a diameter of 5 mm. The heat-treatment of these samples was similar to the heat-treatment of the 3DND-experiments. However, the

four samples were annealed at 953 K for 50, 100, 150, or 200 s and subsequently quenched to room temperature to freeze in the high temperature microstructure. These samples were examined with an optical microscope.

5.3.4. Results and discussion

The 3DND-measurements are presented in Fig. 5.6. The final value of the rotation of the polarization vector is reached after approximately 300 s indicating that the transformation is finished. Fig. 5.6 shows that there is an extra depolarization during the transformation, represented by a dip in $D_\perp$, while $D_{//}$ is unaffected. This means that the magnetic domains are not randomly distributed during part of the transformation.

The ratio $\alpha = \ln(D_{//})/\ln(D_\perp)$ is constant if the magnetic domains are randomly distributed in the sample throughout the transformation and if the change in magnetization orientation distribution during the transformation has a negligible small effect. Near the end of the transformation α becomes constant, since the sample is then filled with magnetic domains. α_f represents the ratio $\ln(D_{//})/\ln(D_\perp)$ at the end of the transformation and is determined to be 1.4. The correction factor D_c can be determined from the experiment via $D_c = D_\perp/(\exp\{\ln(D_{//})/\alpha_f\})$, if it is assumed that the change in magnetization orientation distribution during the transformation has a negligible small effect on α. As shown in Fig. 5.6 the factor D_c continuously decreases during the first stage of the transformation until it reaches a minimum half way the transformation. For higher fractions D_c increases and finally reaches unity at the end of the transformation.

Fig. 5.7 shows the pearlite fraction f_p and average magnetic particle radius δ as a function of time for the isothermal transformations at 943, 948, and 953 K. The deduced average magnetic domain size is corrected for the extra depolarization, which is caused by a non-random distribution of magnetic domains. The large error bars, which appear in the region half way the transformation are caused by a largely depolarized neutron beam (see Fig. 5.6).

The polarized neutron beam probes the magnetic correlation length over which the local magnetic induction is oriented in the same direction. Due to the shape anisotropy the magnetic moments are preferentially aligned parallel to the ferrite plates. For bend ferrite plates, the local magnetic moment can follow the bending of the plate under certain conditions. This so-called flowing magnetization can appear in soft magnets over a distance, which is smaller than the domain wall width $\Delta \propto (A/K_c)^{1/2}$, but larger than the exchange length $\Delta_e \propto (A/K_d)^{1/2}$ [9]. A is the exchange stiffness, K_c the crystal anisotropy, and $K_d = \mu_0(M_s^\alpha)^2/2$ the stray field energy. The order of magnitude of Δ_e and Δ can be estimated by taking the values for pure iron at $T = 950$ K: $A_{Fe} \approx 2.65\times10^{-11}$ J/m [10], $K_c^{Fe} \approx 431$ J/m^3 [9,10], and $\mu_0 M_s^\alpha \approx 1.35$ T [6], which leads to $\Delta_e \approx 6$ nm and $\Delta \approx 0.25$ μm. The thickness of a ferrite plate is usually smaller than the calculated value for Δ. As a consequence the local magnetic induction is expected to follow the orientation of the ferrite plate when it bends. A comparison between the measured average magnetic domain size and the optical images of the microstructure shows that the measured domain size corresponds to the average distance over which the ferrite plates are parallel ($\delta \approx 7.5$ μm).
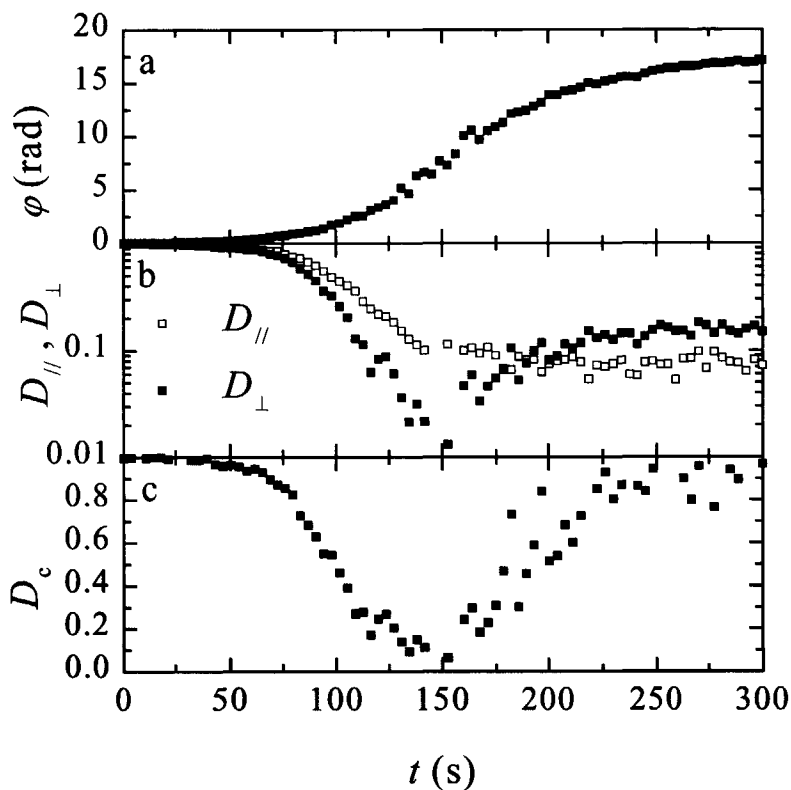
*Fig. 5.6: The measured rotation of the polarization vector φ (a), the components of the depolarization matrix **D** parallel $D_{//}$ and perpendicular $D_\perp$ to the applied magnetic field (b), and the correction factor D_c (c) as a function of time t during the isothermal transformation at 953 K.*

The obtained correction factor D_c contains information about the cluster formation of pearlite colonies during the austenite/pearlite transformation, since it represents the spatial distribution of the magnetic domains in the sample. For a random distribution D_c equals one. In Fig. 5.8 the correction factor D_c is shown as a function of the pearlite fraction f_p for isothermal transformations at 943 K, 948 K, and 953 K. The shape of the curve does not change significantly as a function of the isothermal transformation temperature, except for small values of f_p.

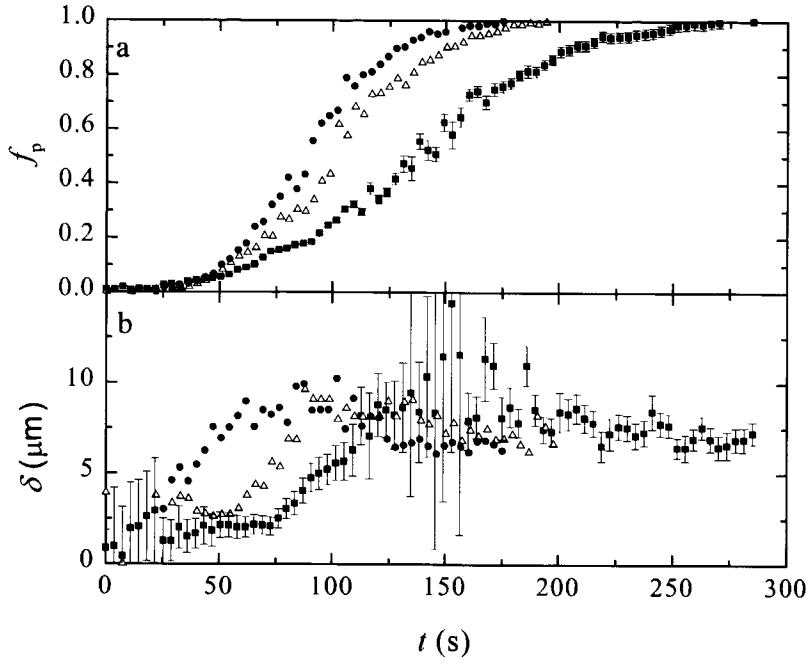*Fig. 5.7: The fraction pearlite f_p (a) and average magnetic particle radius δ (b) as a function of time for isothermal transformations at 943 K (solid sphere), 948 K (open triangle), and 953 K (solid square). For clarity reasons only the error bars at 953 K are shown. Comparable errors are observed for the other two temperatures.*

Fig. 5.8 is compared to optical microscopy images (see Fig. 5.9), which were taken after the quench-experiment. The general trend is that the pearlite colonies randomly nucleate at austenite grain corners just after the steel started to transform. Shortly thereafter, new pearlite colonies nucleate next to an existing pearlite colony. At this stage clusters of pearlite colonies are formed. However, new pearlite colonies also nucleate at austenite grain boundaries, which results in a mixture of individual pearlite colonies and clusters of pearlite colonies. The non-random distribution of pealite colonies is the strongest approximately half way the transformation. At this stage there are a few clusters of pearlite colonies, which are very large ($\sim$160 μm) and many relatively small individual pearlite colonies ($\sim$15 μm). Towards the end of the transformation, the clusters start to impinge until all pearlite colonies are connected and a homogeneous structure is formed at the end of the transformation.
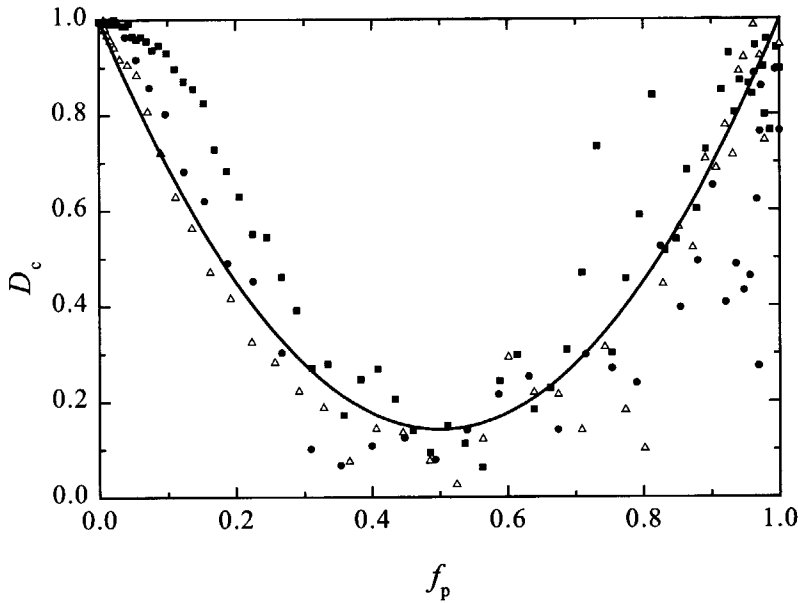
Fig. 5.8. The correction factor D_c as a function of the pearlite fraction f_p for isothermal transformations at 943 K (solid sphere), 948 K (open triangle), and 953 K (solid square). The solid line indicates a fit to the data (see text).

Our present data of D_c as a function of f_p are symmetric around $f_p = 0.5$ and are expected to be proportional to $f_p(1-f_p)$. The experimental data can be fitted with $D_c = 1-\varepsilon f_p(1-f_p)$, where ε is the cluster parameter, which is a measure for the degree of cluster formation half way the transformation ($f_p = 0.5$). For a random distribution of pearlite colonies in the sample $\varepsilon = 0$. A fit of the three data sets gives a value of $\varepsilon \approx 3.4$, which is shown in Fig. 5.8. The cluster parameter can also be estimated from the optical microscopy image which was taken half way the transformation. By comparing the optical microscopy images with Fig. 5.7 it is estimated that there are approximately $N_c = 11$ magnetic domains (colonies) with an average radius of $\delta \approx 7.5$ μm along the distance of a cluster (≈ 160 μm). It is estimated from the optical microscopy images that there are about $N_i = 4$ individual pearlite colonies over an equivalent distance outside a cluster. About 1/3 of the sample consist of clusters and about 2/3 of individual colonies. Thus, the normalized spatial distribution function can be represented by two delta-functions δ_f : $f(N) = 2/3\delta_f(N-N_i)+1/3\delta_f(N-N_c)$. From the previous paper it is known that $<m_z> \approx 0.52$ when $f_p = 0.5$ [5] leading to $\varphi_p \approx 0.55$ rad. Inserting this information in Eq. (1), gives a value for $\varepsilon \approx 4$, which is close to the value found with ND.

Acknowledgements

References

[1] M.Th. Rekveldt, Z. Phys. 259 (1973) 391.
[2] R. Rosman and M.Th. Rekveldt, J. Magn. Magn. Mater. 95 (1991) 319.
[3] S.G.E. te Velthuis et al., Acta Mater. 48 (2000) 1105.
[4] D.S. Zhou and G.J. Shiflet, Metall. Trans. A 23A (1992) 1259.
[5] L.J.G.W. van Wilderen et al., to be published in Appl. Phys. A.
[6] A.S. Arrott and B. Heinrich, J. Appl. Phys. 52 (1981) 2113.
[7] N.H. van Dijk et al., Physica B 267-268 (1999) 88.
[8] R. Rosman and M.Th. Rekveldt, Phys. Rev. B 43 (1991) 8437.
[9] A. Hubert and R. Schäfer, in: Magnetic domains (Springer, Berlin, 1998).
[10] C. Kittel, in: Introduction to Solid State Physics (Wiley, New York, 1986).

5.4. In-situ study of pearlite nucleation and growth during isothermal austenite decomposition in nearly eutectoid steel

S.E. Offerman, L.J.G.W. van Wilderen, N.H. van Dijk, J. Sietsma, M.Th. Rekveldt, and S. van der Zwaag, *Acta Materialia*, 51 (2003) 3927-3938.

Abstract

The evolution of the microstructure during the isothermal austenite/pearlite transformation in a nearly eutectoid steel was studied by the three-dimensional neutron depolarization technique, which simultaneously provides information about the pearlite fraction, the average pearlite colony size, and the spatial distribution of the pearlite colonies during the transformation. The in-situ measurements show that the pearlite nucleation rate increases linearly with time with a temperature-dependent slope. The in-situ measured average pearlite growth rate is accurately described by the Zener-Hillert theory, which assumes that volume diffusion of carbon is the rate-controlling mechanism. The measured overall transformation rate deviates from the predictions of the theory developed by Kolmogorov, Johnson, Mehl, and Avrami.

5.4.1. Introduction

Pearlite is a common constituent of a wide variety of steels and provides a substantial contribution to the strength. A pearlite colony consists of two interpenetrating single crystals of ferrite and cementite (Fe_3C), which are primarily ordered as alternating plates. Pearlite that consists of fine plates is harder and stronger than pearlite that consists of coarse plates. This morphology of pearlite is largely determined by the evolution of the austenite/pearlite phase transformation during the production process. Control of the pearlite phase transformation kinetics is thus of vital importance for the production of tailor-made steels.

Despite the large variety of austenite/pearlite phase transformation models that have been proposed and the experiments that have been performed to test them in the past 60 years, the kinetics of this transformation is still not completely understood. The reason why the pearlite nucleation mechanism is still not fully understood, lies in the experimental difficulty to measure nucleation phenomena and in particular the nucleation of pearlite. The nucleation mechanism of pearlite involves the formation of two crystallographic phases. In hypo-eutectoid steels the pro-eutectoid ferrite nucleates first and continues to grow with the same crystallographic orientation during the pearlite formation as part of a pearlite colony [1,2]. In this case the cementite nucleation is the rate-limiting step in the formation of pearlite. In hyper-eutectoid steels the roles of ferrite and cementite are reversed and in perfectly eutectoid steel the pearlite nucleation is assumed to take place at the austenite grain corners, edges, and boundaries. However, the exact nature of the pearlite nucleation mechanism is still under debate.

Another important and continuing subject of debate is the rate-controlling mechanism for the growth of pearlite. There are two different theories proposed for the growth of pearlite. The Zener-Hillert theory assumes that the volume diffusion of carbon in the austenite, ahead of the advancing pearlite, is the rate-controlling mechanism [3, 4]. The Hillert theory on the other hand assumes that grain boundary diffusion of the carbon atoms is the rate-controlling mechanism [5]. Several experimental studies were performed over the last decades in order to measure the pearlite growth rate and determine the rate-controlling

mechanism. Both volume [6-9] and grain boundary diffusion [10] were claimed to be the rate-controlling mechanism, as well as more complex mechanisms [11].

The theory developed by Kolmogorov, Johnson, Mehl, and Avrami [12-16], also known as the KJMA theory, predicts the overall transformation rate on the basis of nucleation and growth rates. The KJMA-theory is one of the oldest and most widely used models to describe the pearlite phase transformation kinetics. This concept still forms the basis of many of the current phase transformation models.

The pearlite nucleation and growth rates have so far been determined from ex-situ optical and electron microscopy measurements, in which a series of steel specimens is annealed for increasing times at a particular transformation temperature. The high-temperature microstructure is frozen in at several stages of the transformation by quenching the specimen to room temperature. At each stage the largest pearlite colony size is determined, which is a measure for the pearlite growth rate. This method has two drawbacks. The first drawback is that it only gives an estimate of the pearlite growth rate if the largest pearlite colony can be related to the first pearlite colony that nucleated. The second drawback is that the method only reflects the highest observed growth rate.

These drawbacks can be avoided by using the three-dimensional Neutron Depolarization (3DND) technique [17, 18], which has created the opportunity to study phase transformations in-situ in the bulk of steel. The 3DND technique provides a unique insight into the formation of the microstructure as it probes the volume fraction of the magnetic phase, the mean magnetic particle size, and the spatial distribution of the forming ferromagnetic phase in the paramagnetic (austenite) matrix [19]. The technique is capable of determining these three parameters in-situ and simultaneously, which makes it a powerful tool for the study of phase transformations in the bulk of ferromagnetic materials.

The aim of this research is to measure in-situ the pearlite fraction, the average pearlite colony size, and the spatial distribution as a function of the isothermal transformation time. This gives information about the nucleation rate, the rate-controlling mechanism for the growth of pearlite, and the validity of the KJMA theory for the prediction of the overall austenite/pearlite transformation rate. The present paper is related to two previous papers on the austenite/pearlite transformation in the same steel [20, 21], which reported on the relation between the magnetic domain structure and the microstructure, and gave a comparison with the results of additional dilatometry experiments.

5.4.2. Pearlite transformation kinetics

NUCLEATION

The nucleation rate of the newly formed phase during a phase transformation is described by the classical nucleation theory [22], in which the time dependent nucleation rate $\dot{N}$ is expressed as

$$\dot{N} = N_n \beta^* Z \exp\left(-\frac{\Delta G^*}{k_B T}\right) \exp\left(-\frac{\tau}{t}\right), \tag{5.1}$$

where N_n is the number of potential nucleation sites, Z is the Zeldovich non-equilibrium factor, $k_B = 1.38 \times 10^{-23}$ J/K is the Boltzmann constant, and T the absolute temperature. The rate at which the iron atoms are added onto the critical nucleus is taken into account by the frequency factor β^*. The time τ represents the incubation time and t is the isothermal

transformation time. The time-independent part of this equation is the steady state nucleation rate. The energy barrier that has to be overcome in order to form a critical nucleus is referred to as the activation energy for nucleation ΔG^*, which can in general be written as

$$\Delta G^* = \Psi / \Delta g_V^2 . \tag{5.2}$$

The driving force for nucleation is the decrease in Gibbs free energy per unit volume of the system Δg_V during the phase transformation, which depends on the chemical composition and the temperature. The creation of a new nucleus requires energy due to the formation of an interface between the nucleus and the original phase. However, in the case that the nucleus is formed at a grain boundary the removal of incoherent austenite/austenite grain boundaries releases energy that can be used for the creation of a new interface. The balance between the energy that is required for the formation of a new interface and the energy that is released due to the removal of the old interface is represented by the factor Ψ. It is the uncertainty in Ψ which makes predictions of the nucleation rate very difficult.

GROWTH

Nucleation is followed by the growth of pearlite colonies. In the Zener-Hillert model [3, 4], which assumes that volume diffusion of carbon is the rate-controlling mechanism for the growth of pearlite, the growth rate G_V is given by

$$G_V = \frac{D_{C,V}^{\gamma}}{k_V} \frac{\lambda^2}{\lambda^\alpha \lambda^\theta} \frac{C_{eq}^{\gamma\alpha} - C_{eq}^{\gamma\theta}}{C_{eq}^{\theta} - C_{eq}^{\alpha}} \frac{1}{\lambda} \left(1 - \frac{\lambda_c}{\lambda} \right), \tag{5.3}$$

where k_V is a geometrical constant related to the volume diffusion mechanism, $D_{C,V}^{\gamma}$ is the volume diffusion coefficient of carbon in austenite, and λ^α and λ^θ are the lamella thickness of the ferrite and cementite, respectively. The pearlite lamellar spacing amounts to $\lambda = \lambda^\alpha + \lambda^\theta$. $C_{eq}^{\gamma\alpha}$ and $C_{eq}^{\gamma\theta}$ are the equilibrium carbon concentrations in the austenite in contact with ferrite and cementite, respectively. C_{eq}^{α} and C_{eq}^{θ} are the equilibrium carbon concentrations in ferrite and cementite, respectively. The critical (theoretical minimum) spacing λ_c is given by

$$\lambda_c = \frac{2\gamma^{\alpha\theta} T_{A1}}{\Delta T} \frac{V_m}{\Delta H_m} , \tag{5.4}$$

where $\gamma^{\alpha\theta} = 0.94$ J/m² [23] is the interfacial free energy of the ferrite/cementite interface in the pearlite, T_{A1} (= 995 K for the studied steel) is the austenite/pearlite equilibrium transition temperature, $\Delta T = T_{A1} - T$ is the undercooling, $\Delta H_m = 4.3$ kJ/mol [23] is the change in molar enthalpy, and $V_m = 7.1 \times 10^{-6}$ m³/mol the molar volume. The volume diffusion coefficient of carbon in austenite $D_{C,V}^{\gamma}$ depends on the temperature and the nominal carbon concentration and can be described by [24]

$$D_{C,V}^{\gamma} = 4.53 \times 10^{-7} \left(1 + Y_C (1 - Y_C) \frac{8339.9}{T} \right) \exp \left\{ - \left(\frac{1}{T} - 2.221 \times 10^{-4} \right) (17767 - 26436 Y_C) \right\}, \tag{5.5}$$

where $D_{C,V}^{\gamma}$ is in m²/s and the temperature T in K. The site fraction Y_C of carbon on the interstitial sub-lattice is given by

$$Y_C = \frac{x_C}{1 - x_C},$$

(5.6)

where x_C (= 0.0323 for the studied steel) is the overall atom fraction of carbon in the alloy.

In the Hillert model [5], which assumes that grain boundary diffusion of carbon is the rate-controlling mechanism for the growth of pearlite, the growth rate G_{GB} is given by:

$$G_{GB} = 12 k_{GB} D_{C,GB}^{\gamma} \delta \frac{\lambda^2}{\lambda^\alpha \lambda^\theta} \frac{C_{eq}^{\gamma\alpha} - C_{eq}^{\gamma\theta}}{C_{eq}^{\theta} - C_{eq}^{\alpha}} \frac{1}{\lambda^2} \left(1 - \frac{\lambda_c}{\lambda}\right),$$

(5.7)

where k_{GB} is the ratio of carbon concentration in the bulk of the austenite and the grain boundary and δ is the thickness of the boundary. The grain boundary diffusion coefficient of the carbon atoms $D_{C,GB}^{\gamma}$ can be estimated by assuming that the activation energy is half that of the activation energy for volume diffusion [25]. In the present case the argument of the exponential factor in equation (4) is multiplied by 0.5.

For the eutectoid composition C_{eq}^{θ} = 6.67 wt.% , $C_{eq}^{\alpha} \approx 0.02$ wt.%, $\frac{\lambda^\alpha}{\lambda^\theta} \approx 7$, and k_V = 0.72 [9]. Further, we can assume that $C_{eq}^{\gamma\theta} - C_{eq}^{\gamma\alpha} \propto \Delta T$, and $\lambda \propto \Delta T^{-1}$ [26]. As a consequence the two different theories, represented by equations (5.3) en (5.7), can be rewritten in the following form:

$$G_X = c_X D_{C,X}^{\gamma} (\Delta T)^{\beta},$$

(5.8)

where the subscript X equals V or GB, which represents the volume or grain boundary diffusion theory, respectively. c_X is a constant, which is different for volume or grain boundary diffusion of carbon. The exponent β expresses the main difference between the two theories. For volume diffusion β = 2 and for grain boundary diffusion β = 3. Hence, the rate determining mechanism for the growth of pearlite can be determined from the exponent β.

OVERALL TRANSFORMATION

The overall pearlite transformation rate can be described by the KJMA theory, which predicts the fraction f of the formed phase as a function of the isothermal transformation time t as

$$f(t) = 1 - \exp\left(-k_g G^d \int_0^t \dot{N}_u(t')(t - t')^d \, dt'\right),$$

(5.9)

where G is a constant growth rate, d the dimensionality of the growth and k_g a constant, which depends on the geometry of the particle, e.g. k_g = $4\pi/3$ for spherical particles (d = 3). The nucleation rate $\dot{N}_u$ is defined as the number of nuclei per unit untransformed volume per

unit time. It is assumed that the nuclei are randomly distributed. The integration parameter t' can be interpreted as the time at which nucleation of grains took place.

Within the KJMA theory it is usually assumed that the nucleation rate is constant or that there is a fixed number of pre-existing nuclei throughout the transformation. However, Cahn [27] showed that when the nucleation rate, per unit untransformed volume, increases with time according to

$$\dot{N}_u(t) = k_u t^m,$$ (5.10)

where k_u and m are constants, the KJMA equation becomes

$$f(t) = 1 - \exp\left(-\frac{8\pi m!}{(d+m+1)!} k_u G^3 t^{m+4}\right),$$ (5.11)

for spherical particles that grow at a constant rate.

5.4.3. Three-dimensional neutron depolarization

The transmission of a monochromatic polarized neutron beam through the sample is characterized by the depolarization matrix D according to $P' = D \cdot P$, where P and P' are the polarization vectors before and after transmission, respectively. The rotation of the polarization vector is a measure for the magnetic volume fraction and the degree of depolarization is a measure for the average magnetic domain size.

The rotation φ of the polarization vector is, in an eutectoid steel, related to the volume pearlite fraction f_p via

$$\varphi = \eta L c^{1/2} <B>,$$ (5.12)

where L is the thickness of the sample, $c = 2.15 \times 10^{29} \lambda^2$ $T^{-2}m^{-4}$, and $\lambda = 0.124(1)$ nm the neutron wavelength. The shape factor which accounts for the effect of stray fields

$$\eta = (1-f_p)\eta^P + f_p \eta^M$$ (5.13)

is determined by a microscopic shape factor $\eta^P = 0.5$ for microscopic spherically shaped particles and a macroscopic shape factor $\eta^M = 0.905$ for our plate-like sample [28]. The average magnetic induction inside the sample is given by

$$<B> = f_p <m_z> \mu_0 M_s^P,$$ (5.14)

where $<m_z>$ is the average reduced magnetization in the direction of the applied magnetic field (5.16 mT) along the long axis of the sample. The saturation magnetization of pearlite M_s^P can be calculated from the saturation magnetization of ferrite M_s^α [29] multiplied by the equilibrium volume fraction of ferrite f_α inside a pearlite colony. For the studied steel f_α is evaluated with the thermodynamic database MTDATA$^\circledR$ and determined to be 0.90. During the experiment the temperature was higher than the Curie temperature of cementite, but was lower than the Curie Temperature of ferrite.

78

The depolarization of the polarized neutron beam, described by det(D), is caused by local variations in the magnetic induction $<(\Delta B)^2>$ inside the sample, and can be characterized for spherical particles by

$$\det(D) = \exp\{-2cL\delta<(\Delta B)^2>\}. \tag{5.15}$$

The average magnetic particle radius δ can be evaluated from the experimentally determined depolarization matrix D and model equations for $<(\Delta B)^2>$, which depends on f_p [18,19]. The measured depolarization can be written as det(D) = $D_\perp^2 D_{//}$, where $D_\perp$ and $D_{//}$ are the elements of the depolarization matrix D perpendicular and parallel to the applied magnetic field, respectively.

The polarized neutron beam probes the magnetic correlation length over which the local magnetic induction is oriented in the same direction, which means that δ represents the average distance over which the ferrite plates within a pearlite colony are more or less parallel [21]. In this paper it is assumed that the volume of a pearlite colony can be approximated by the volume in which the ferrite and cementite plates are more or less parallel. To a first approximation this assumption is valid, however from a crystallographic point of view a pearlite colony can be larger.

In the case that the magnetic particles are not randomly distributed over the sample, an extra depolarization of the polarized neutron beam will arise, which is not related to the magnetic domain size. This extra depolarization will affect all the elements of the depolarization matrix that are perpendicular to the applied magnetic field, while the component that is parallel to the magnetic field remains unaffected. In order to separate the contribution of the average magnetic domain size and the clustering (non-random spatial distribution) of particles to the depolarization, a cluster factor D_c is introduced:

$$D_c = \int_0^\infty f(N)\cos\left[\left(N-\langle N\rangle\right)\varphi_p\right]dN, \tag{5.16}$$

where $f(N)$ is the normalized spatial distribution function of the number of particles N along a neutron path, $<N>$ is the average number of particles along the neutron path, and φ_p is the average rotation per domain [30]. The cluster factor is a measure for the degree of cluster formation in the specimen. It was shown [21] that the cluster factor can be deduced under certain conditions from the experiment according to

$$D_c = D_\perp \exp\left[-\frac{\ln(D_{//})}{\alpha_f}\right] \tag{5.17}$$

where, α_f represents the ratio $\ln(D_{//})/\ln(D_\perp)$ at the end of the transformation. In order to calculate the average magnetic domain size, the measured perpendicular component $D_\perp$ is multiplied by a factor $1/D_c$ [21]. The rotation φ of the polarization vector is not influenced by the manner in which the magnetic domains are distributed.

5.4.4. Experiment

The composition of the studied nearly eutectoid steel (in wt.%) is 0.715 C, 0.611 Mn, 0.266 Cr, 0.347 Si, 0.012 P, 0.03 S, 0.094 Ni, 0.235 Cu, 0.021 Mo, 0.025 Sn, and the rest is Fe. The austenite/pearlite phase transformation kinetics was studied by neutron depolarization and optical microscopy. The sample for the 3DND-experiments with dimensions $100 \times 15 \times 0.4$ mm^3 is coated with a nickel layer of approximately 15 μm thickness to avoid decarburization. The sample was annealed at 1173 K for 0.5 h in a nitrogen atmosphere, subsequently cooled with 20 K/s to 943 K, and held until the transformation was finished. This temperature cycle was repeated with the same sample for transformation temperatures of 948 and 953 K in order to study the influence of the degree of undercooling on the transformation kinetics. The 3DND measurements have been performed at the PANDA instrument at the nuclear reactor of the Interfaculty Reactor Institute.

Four cylindrical samples were prepared with a diameter of 5 mm and a length of 10 mm for examination with the optical microscope. The samples were annealed at 1173 K for 0.5 h under a vacuum of 10^{-4} mbar, cooled with 20 K/s to 953 K, held for either 50, 100, 150, or 200 s, and subsequently quenched to room temperature to freeze in the high-temperature microstructure.

5.4.5. Results

Fig. 5.9 shows the optical microscopy images of the microstructure at different stages of the isothermal austenite/pearlite phase transformation at $T = 953$ K ($\Delta T = 42$ K). When the transformation has proceeded for 50 s, the microstructure consists of individual pearlite colonies. After 100 s, also a few large clusters of pearlite colonies are observed besides the individual pearlite colonies. After 150 s more large clusters are formed, while individual pearlite colonies are still present. After 200 s the pearlite colonies have formed an interconnecting network, which encloses a number of untransformed austenite grains.

The corresponding 3DND measurements during the isothermal transformation at 953 K are presented in Fig. 5.10. Similar results were obtained for the isothermal transformations at 948 and 943 K. Fig. 5.10a shows that after approximately 300 s the rotation of the polarization vector φ reaches its final value, which indicates that the transformation is finished. Fig. 5.10b shows the components of the depolarization matrix D, which are perpendicular, $D_\perp$, and parallel, $D_{//}$, to the applied magnetic field, as a function of the transformation time. Around 150 s $D_\perp$ has a minimum, which is not present in $D_{//}$. From an earlier treatment of the data [21] we concluded that the magnetic domains are not randomly distributed during part of the transformation. The cluster factor D_c is obtained from equation (5.17) and α_f is determined to be 1.4.

The cluster factor D_c contains information about the cluster formation of pearlite colonies during the austenite/pearlite transformation, since it represents the spatial distribution of the magnetic domains in the sample. For a random distribution D_c equals one. As shown in Fig. 5.10c the factor D_c continuously decreases during the first stage of the transformation until it reaches a minimum half way the transformation. This indicates that the microstructure evolves from a random to a non-random distribution of pearlite colonies. For higher fractions D_c increases and finally reaches unity at the end of the transformation. This indicates that the pearlite clusters start to form an interconnected network resulting in a more homogeneous structure. This behavior corresponds to the evolution of the microstructure as shown in Fig. 5.9.
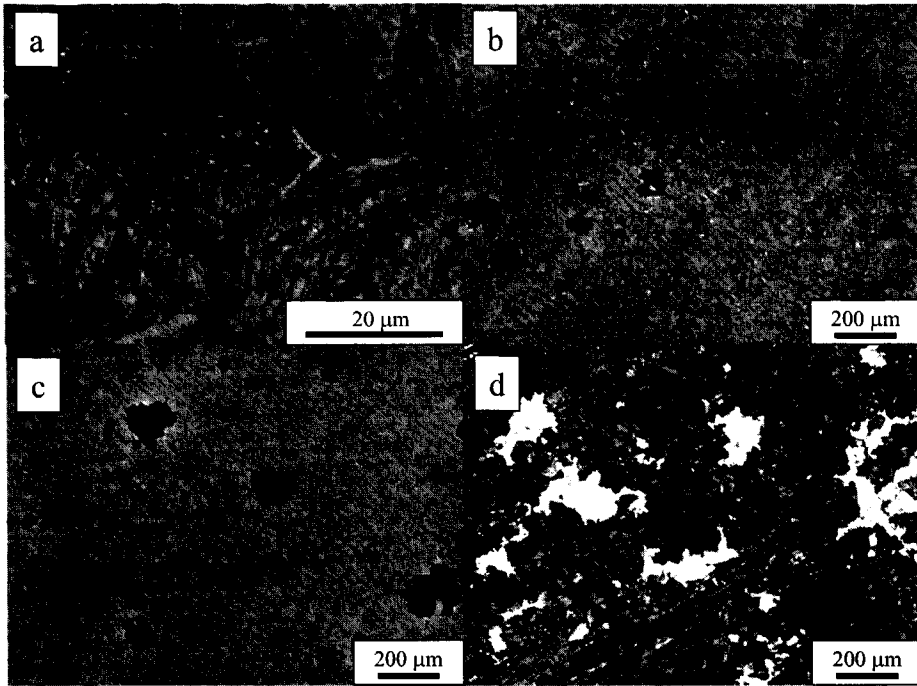
Fig. 5.9: Optical microscopy images of the microsture at different stages of the isothermal austenite/pearlite phase transformation at T = 953 K. The samples were quenched to room temperature after 50 s (a), 100 s (b), 150 s (c), and 200 s (d). Note that the magnification for (a) is 20x larger than for (b), (c), and (d).

Fig. 5.11 shows the formed fraction f and average magnetic particle radius δ, which were determined from 3DND measurements as a function of time for the three isothermal transformations. The deduced average magnetic domain size is corrected for the extra depolarization, which is caused by a non-random distribution of magnetic domains. A largely depolarized neutron beam (see Fig. 5.10b) causes the large error bars, which appear in the region half way the transformation. The increase in average particle size between $f = 0.1$ and 0.5 in Fig. 5.11b represents to the average pearlite growth rate G, which is given in Table 5.1.

5.4.6. Discussion

At a moderate undercooling the austenite/pearlite transformation in eutectoid steel is characterized by a non-random distribution of pearlite colonies during the transformation. The optical microscopy and 3DND measurements show that a first small amount of pro-eutectoid ferrite is formed. The pearlite colonies randomly nucleate at the formed pro-eutectoid ferrite grains and austenite grain corners just after the steel started to transform. Shortly thereafter, new pearlite colonies nucleate next to the existing pearlite colonies. At this stage large clusters of pearlite colonies are formed.
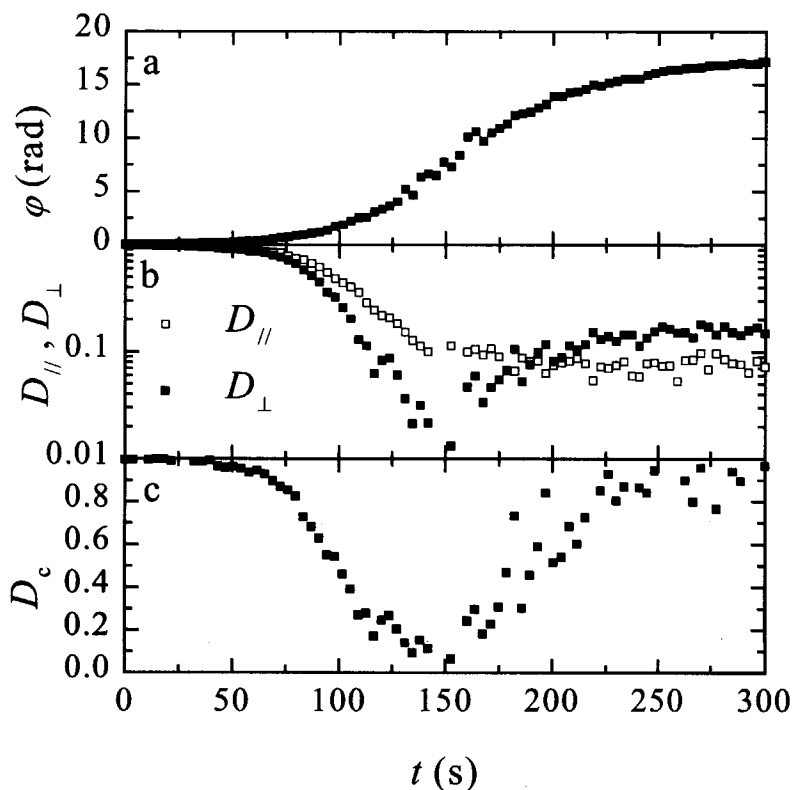
81

Fig. 5.10: The measured rotation of the polarization vector φ (a), the components of the depolarization matrix **D** parallel (D//) and perpendicular (D⊥) to the applied magnetic field (b), and the correction factor Dc (c) as a function of time t during the isothermal transformation at T = 953 K.

However, new pearlite colonies also nucleate at austenite grain boundaries, which results in a mixture of individual pearlite colonies and clusters of pearlite colonies. At this stage there are a few clusters of pearlite colonies, which are very large (≈160 µm) and many relatively small individual pearlite colonies (≈15 µm), as indicated in Fig. 5.9. Towards the end of the transformation, the clusters start to impinge until all pearlite colonies are connected and a homogeneous structure is formed at the end of the transformation.

The increase in average particle size during the first 75 s of the transformation at T = 953 K (see Fig. 5.11b) corresponds to the growth of pro-eutectoid ferrite, of which the radius R^α increases as a function of time according to the Zener-theory (solid line in Fig. 5.11b) [31]. The analytical results can be approximated by the following relation:
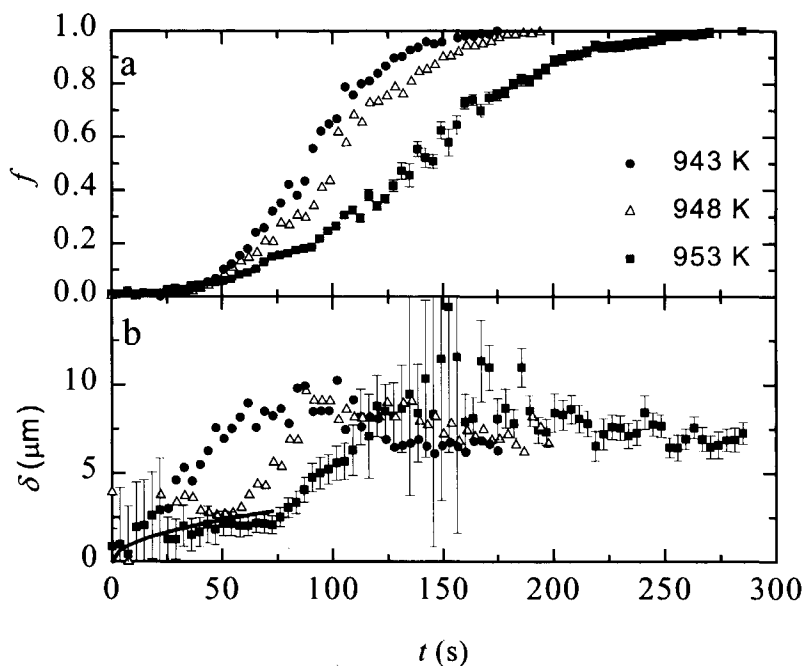
Fig. 5.11: The fraction pearlite f (a) and average magnetic particle radius δ (b) as a function of time for isothermal transformations at 943 K (solid sphere), 948 K (open triangle), and 953 K (solid square). For clarity reasons only the error bars at 953 K are shown. Comparable errors are observed for the other two temperatures. The solid line represents the Zener theory for the formation of pro-eutectoid ferrite.

$$R^{\alpha} = 2.102 \left(\frac{C_{\infty}^{\gamma} - C_{eq}^{\gamma}}{C_{eq}^{\alpha} - C_{\infty}^{\gamma}} \right)^{0.5871} \sqrt{D_c^{\gamma} t} \,, \tag{5.18}$$

where C_{eq}^{γ} (≈ 0.77 wt.%) and C_{eq}^{α} (≈ 0.02 wt.%) are the equilibrium carbon concentrations in the austenite and ferrite, respectively. C_{∞}^{γ} is the carbon concentration in the austenite matrix away from the interface. In the present case C_{∞}^{γ} is assumed to be equal to the average carbon concentration (0.715 wt.%). The average carbon concentration in the remaining austenite will hardly change throughout the transformation, because this is a nearly eutectoid steel. With increasing undercooling the pro-eutectoid ferrite has less time to grow and less pro-eutectoid ferrite will form.

83

NUCLEATION

The fraction f of the phases formed can be expressed as

$$f = \frac{4}{3}\pi\delta_\alpha^3 N_\alpha + \frac{4}{3}\pi\delta_p^3 N_p \qquad (5.19)$$

where δ_α and δ_p are the average pro-eutectoid ferrite grain and pearlite colony radius, respectively. N_α and N_p represent the number of pro-eutectoid ferrite grains and pearlite colonies, respectively. From eqn. (5.19) the number of pearlite nuclei N_p can be estimated as a function of transformation time t, which is shown in Fig. 5.12 for the three isothermal transformations. The number of pearlite nuclei is found to increase quadratically with time. In literature it is reported that the number of pearlite nuclei scales with the third power of time [32-34].

The measured number of pearlite colonies N_p can be compared to the classical nucleation theory, after integration of equation (5.1) with respect to time. The integrated equation that gives the number of pearlite colonies as a function of time can be approximated by

$$N_p = k_n t^2 \qquad (5.20a)$$

for times between $t = 0$ and 2τ, with

$$k_n \propto \exp\left(-\frac{\Psi}{\Delta g_V^2 k_B T}\right). \qquad (5.20b)$$

The fact that the number of pearlite nuclei increases quadratically with time, as we have observed, means that the pearlite transformation is finished before the steady state nucleation rate is reached. The lines in Fig. 5.12 represent the fits to Eq. (5.20), which resulted in the values for k_n that are given in Table 5.1.

The rate controlling mechanism for the nucleation of pearlite in hypo-eutectoid steels is the nucleation of cementite, since the pro-eutectoid ferrite continues to grow into the pearlite [6]. The driving force for cementite nucleation Δg_V^θ is calculated for the binary Fe-C system from the thermodynamic database MTDATA®. The common tangent along the ferrite and austenite Gibbs free energy curves was constructed to calculate Δg_V^θ, which means that it is assumed that the ferrite and austenite are in equilibrium before the cementite nucleates. The values for Δg_V^θ are given in Table 1. A best fit of $\ln(k_n)$ to $-\left[\left(\Delta g_V^\theta\right)^2 k_B T\right]^{-1}$ gives a value of $\Psi_0 = 2.2(2)\times10^{-3}$ J^3/m^6 for cementite nucleation during the pearlite formation.

The activation energy for nucleation is directly proportional to the factor Ψ, as can be seen from Eq. (5.2). If for example the energy that is required for the formation of a new interface is almost balanced by the energy that is released by transformation, nucleation can take place relatively easily, because the activation energy is then relatively small. From in-situ synchrotron measurements it was recently determined that for the austenite/ferrite phase transformation in medium carbon steel $\Psi_\alpha = 5\times10^{-8}$ J^3/m^6 for the nucleation of ferrite [1].
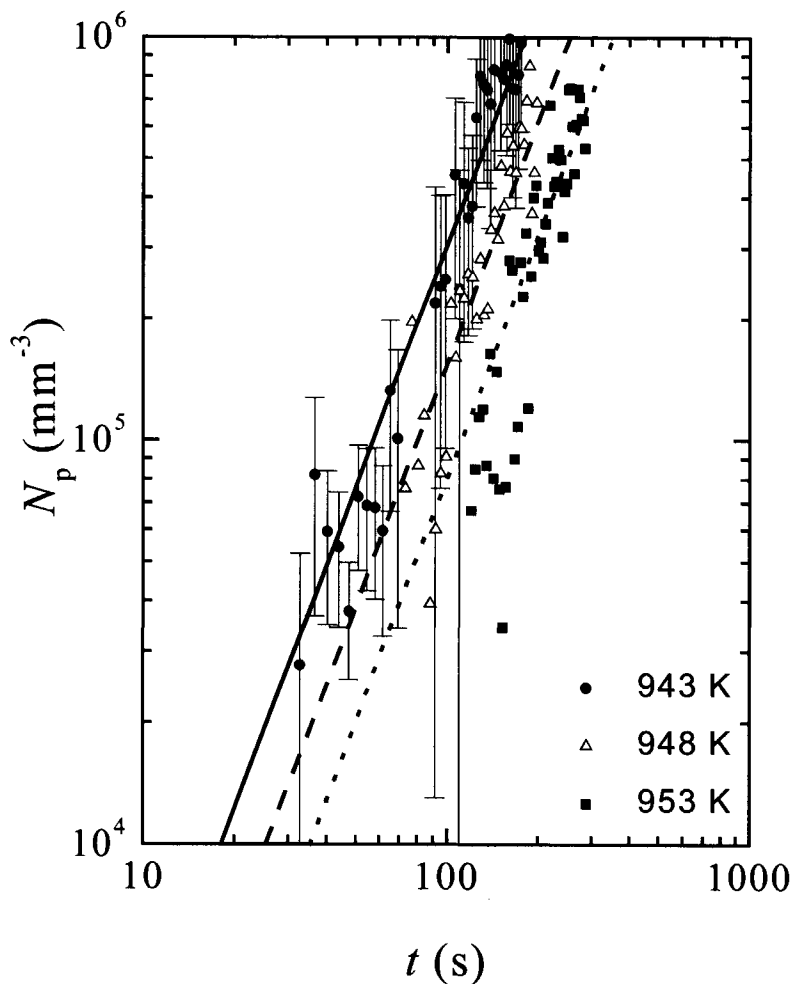
Fig. 5.12. The number of pearlite colonies N_p as a function of the transformation time t for the isothermal transformations at 943 K (solid sphere, straight line), 948 K (open triangle, dashed line), and 953 K (solid square, dotted line).

A comparison between Ψ_α and Ψ_θ shows that the effect of interfacial energies on the activation energy for the cementite nucleation during the pearlite formation is approximately 10^5 times higher than for the ferrite nucleation. This is probably related to the fact that during the nucleation of pro-eutectoid ferrite high-energy austenite/austenite grain boundaries are replaced by mainly low-energy or almost coherent austenite/ferrite interfaces.

Table 5.1: Thermodynamic and kinetic parameters of the studied nearly eutectoid steel for the three isothermal transformation temperatures. ΔT is the undercooling. Δg_V^θ is the driving force for cementite nucleation. k_n is a temperature dependent prefactor that is related to the time dependent nucleation rate. G is the measured pearlite growth rate. $t_{1/2}$ is the time to transform half of the volume. n is the Avrami exponent.

T (K)	ΔT (K)	Δg_V^θ (J/mol)	k_n (mm^{-3}s^{-2})	G (μm/s)	$t_{1/2}$ (s)	N
943	52	-1613	61(3)	0.15(2)	88(1)	3.31(7)
948	47	-1486	31(2)	0.14(1)	101(1)	3.14(8)
953	42	-1359	16(1)	0.119(5)	135(1)	2.77(4)

The pro-eutectoid ferrite continues to grow with the same crystallographic orientation during the pearlite formation as part of a pearlite colony [1]. This means that cementite nucleation forms the rate-limiting step during pearlite nucleation. During the cementite nucleation, all the energy that is released by the removal of the low-energy austenite/ferrite interface is probably used for the formation of the low-energy ferrite/cementite interface. There is not enough energy left to compensate the energy that is necessary for the formation of the austenite/cementite interface. The main difference between the nucleation of pro-eutectoid ferrite and pearlitic cementite is that the former takes place at high-energy grain boundaries, while the latter takes place at low-energy interfaces. This difference results in a relatively high value for Ψ_θ compared to Ψ_α, which means that the nucleation of pro-eutectoid ferrite is relatively easy compared to the nucleation of pearlitic cementite.

The relatively high value for Ψ_θ may explain the general observation (see e.g. [1]) that during continuous cooling the formation of ferrite may take place at exactly the equilibrium transition temperature, while the subsequent formation of pearlite takes place below its equilibrium transition temperature. In order to form a cementite nucleus during the pearlite formation, Δg_V^2 needs to increase to compensate for the large value of Ψ_θ. As Δg_V^2 increases with increasing undercooling, the temperature at which pearlitic cementite forms is distinctly below the equilibrium transition temperature.

PEARLITE GROWTH

The average growth rate of the pearlite colonies was only measured during the first half of the transformation. In the second half of the transformation the average colony size remained constant. The measured average growth rate at 953 K is $G = 0.12$ μm/s, which is approximately a factor 8 smaller than the value found from a series of quenched specimens of an Fe-0.8C-0.6Mn alloy at 963 K [33]. This difference is possibly caused by the fact that the quench-method gives an estimate of the highest measured pearlite growth rate rather than the average growth rate, given by the 3DND method.

In order to determine the rate-controlling mechanism for the growth of pearlite, $\ln(G/D_{C,V}^\gamma)$ and $\ln(G/D_{C,GB}^\gamma)$ are plotted as a function of the undercooling ΔT in Fig. 5.13. The measured average pearlite growth rate G is either scaled by the volume or grain boundary diffusion coefficient of the carbon atoms. The transition temperature was estimated from MTDATA$^\circledR$ to be $T_{A1} = 995$ K.
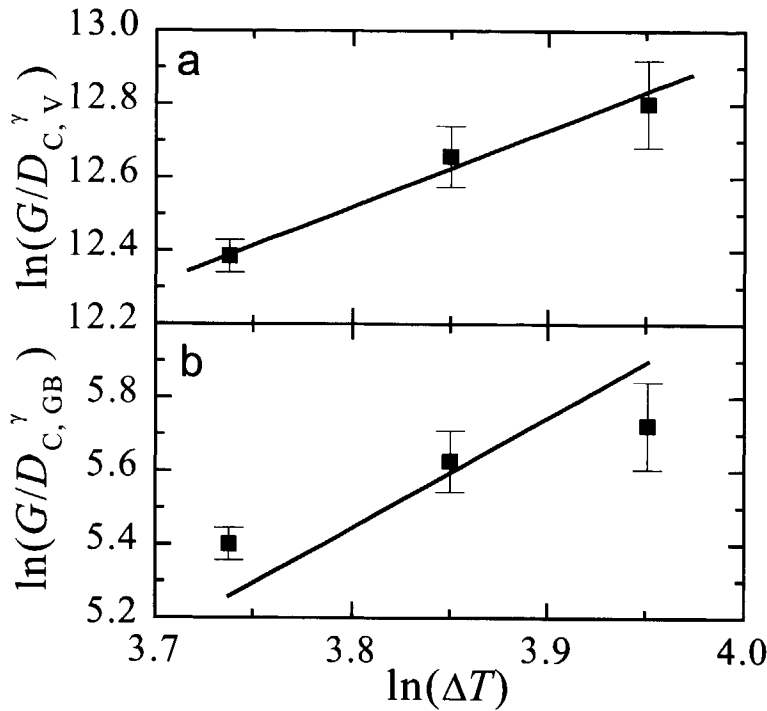
Fig. 5.13: The average growth rate of the pearlite colonies, which was scaled by the temperature dependent volume diffusion coefficient of the carbon atoms $ln(G/D_{C,V}^{\gamma})$ (a) and by the grain boundary diffusion coefficient of the carbon atoms $ln(G/D_{C,GB}^{\gamma})$ (b) as a function of the undercooling $ln(\Delta T)$. The solid lines represent the theory that volume diffusion ($\beta = 2$) (a) or grain boundary diffusion ($\beta = 3$) (b) is the rate-controlling mechanism for pearlite growth.

The solid line in Fig. 5.13a represents a fit of the data to equation (8) with the volume diffusion coefficient of carbon ($D_{C,V}^{\gamma}$) and $\beta = 2$. A best fit of the data in Fig. 5.13a to equation (8) gives a slope of $\beta = 2.1(3)$, which is consistent with the theoretical prediction of $\beta = 2$ for volume diffusion of carbon.

Fig. 5.13b shows the same data points as in Fig. 5.13a, but scaled by the grain boundary diffusion coefficient of the carbon atoms $D_{C,GB}^{\gamma}$. The solid line in Fig. 5.13b represents a fit to equation (8) with the grain boundary diffusion coefficient ($D_{C,GB}^{\gamma}$) and the theoretical value $\beta = 3$. A best fit of the data in Fig. 5.13b with Eq. (8) gives $\beta = 1.7(3)$, indicating a large discrepancy with the theoretical prediction. This means that volume

87

diffusion of the carbon atoms is the rate-controlling mechanism for the pearlite growth at temperatures that are relatively close to the transition temperature. However, in the case that site saturation of the available pearlite nucleation sites takes place on the former austenite grain boundaries, grain boundary diffusion of the carbon atoms can be the rate-controlling mechanism for pearlite growth.

OVERALL TRANSFORMATION

Fig. 5.14 shows a comparison between the measured and the calculated formed fraction as a function of the transformation time for the three isothermal transformation temperatures. The experimental data can be fitted to a generalized KJMA equation

$$f(t) = 1 - \exp(-kt^n),$$ (5.21)

where $k = \ln(2)(t_{1/2})^{-n}$ is a rate constant and n is referred to as the Avrami exponent. The time to transform half of the volume is represented by $t_{1/2}$. A best fit of the experimentally observed fraction curves of Fig. 5.14 with the generalized KJMA equation shows that $n \approx 3$ (see Table 5.1).

The lines in Fig. 5.14 represent the fractions formed, which were calculated by inserting the observed nucleation rate $\dot{N}_p$ and growth rate G_V in equation (5.11). The experimental nucleation rate $\dot{N}_p$ is, however, normalized to the sample volume instead of the untransformed volume. We can write

$$\dot{N}_u = \frac{\dot{N}_p}{1-f} \approx \dot{N}_p.$$ (5.22)

for small fractions of pearlite. Note that the classical nucleation theory in the form of equation (5.20) is the same as equation (5.10) after integration with respect to time with $m=1$.

From Fig. 5.12 we found that the number of pearlite colonies increases quadratically with time, which means that $m = 1$, and from Fig. 5.11 we found that the growth rate is approximately constant. If we assume that the growth is radial ($d = 3$), the Avrami exponent becomes $n = d+m+1 = 5$. From Fig. 5.14 it is apparent that the calculated fraction curve deviates from the experimental observation ($n \approx 3$).

A likely explanation for the difference between the calculated fraction curve and the experimental observation is the following. At the start, the transformation proceeds faster than predicted from equation (5.11) with $n = 5$, because of the formation of pro-eutectoid ferrite. At the end, the transformation proceeds slower than predicted, which is expected to be due to the non-random distribution of nuclei. In that case the growing colonies impinge at an earlier stage than if the nuclei were randomly distributed, which reduces the overall transformation rate. Furthermore, the average pearlite growth rate at the end of the transformation can be different than that measured during the first half of the transformation and Eq. (5.22) no longer holds for large fractions.
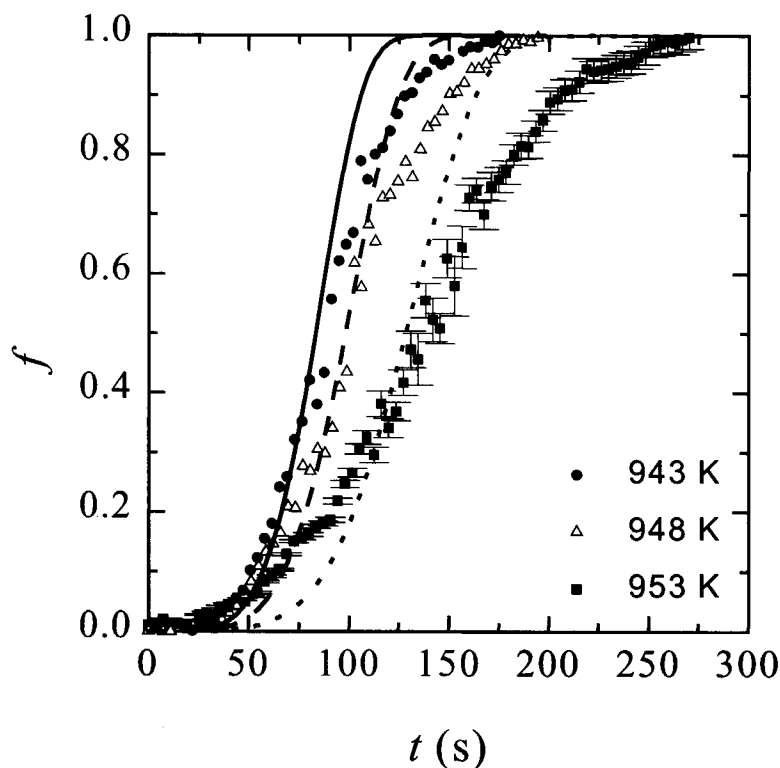
88

Fig. 5.14: Comparison between the measured and calculated formed fraction as a function of the transformation time for the isothermal transformations at 943 K (solid sphere, straight line), 948 K (open triangle, dashed line), and 953 K (solid square, dotted line).

Although, the experimentally observed nucleation and growth rates are used in the calculation of the fraction transformed from the KJMA theory, the comparison with experimentally observed fraction transformed shows once more that the KJMA theory does not give an exact prediction unless its restrictive assumptions are completely fulfilled [35].

5.4.7. Conclusions

Three-dimensional neutron depolarization and optical microscopy measurements were performed in order to study the evolution of the microstructure during the austenite/pearlite transformation in a nearly eutectoid steel. At temperatures that are relatively close to the transition temperature, the transformation is characterized by a non-random distribution of

89

pearlite colonies. The in-situ measurements show that the pearlite nucleation rate is a transient nucleation process, which can be described by the classical nucleation theory. The number of pearlite colonies increases quadratically with time. We find that the effect of interfacial energies on the activation energy for cementite nucleation during the pearlite formation is approximately 10^5 times higher than for the nucleation of pro-eutectoid ferrite. The average pearlite growth rate, which was measured in-situ during the first half of the transformation, corresponds to the theoretical prediction for volume diffusion as the rate-controlling mechanism for the growth of pearlite. A KJMA type of model, which includes the measured nucleation and growth rates deviates from the measured overall transformation rate, because of the presence of pro-eutectoid ferrite and a non-random distribution of pearlite colonies.

Acknowledgements

References

[1] Offerman SE, Van Dijk NH, Sietsma J, Grigull S, Lauridsen EM, Margulies L, Poulsen HF, Rekveldt MTh, Van der Zwaag S. Science 2002;298:1003.
[2] Thompson SW, Howell PR. Scripta Metall. 1988;22:1775.
[3] Zener C. Trans. AIME 1945;167: 550.
[4] Hillert M. Jerkont. Ann. 1957;141:757.
[5] Hillert M. Met. Trans. 1972;3:2729.
[6] Frye JH, Stansbury EE and McElroy DL. Trans. AIME 1953;197:219.
[7] Cheetman D, Ridley N. J. Iron Steel Inst. 1973;211:648.
[8] Pearson DD, Verhoeven JD, Metall. Trans. A 1984;15A:1037.
[9] Ridley N. In: Phase Transformations in Ferrous Alloys, TMS-AIME, Warrendale, PA, 1984.
[10] Sundquist BE. Acta Metall. 1968;16:1413.
[11] Whiting MJ. Scipta Mater. 2000;43:969.
[12] Kolmogorov AN. Izv. Acad. Nauk SSSR, Ser. Materm. 1937;3:355.
[13] Johnson J, Mehl R. Trans. AIME 1939;135:416.
[14] Avrami M. J. Chem. Phys. 1939;7:1103.
[15] Avrami M. J. Chem. Phys. 1940;8:212.
[16] Avrami M. J. Chem. Phys. 1941;9:117.
[17] Rekveldt MTh. Z. Phys. 1973;259:391.
[18] Rosman R, Rekveldt MTh. J. Magn. Magn. Mater. 1991;95:319.
[19] Te Velthuis SGE, Van Dijk NH, Rekveldt MTh, Sietsma J, Van der Zwaag S. Acta Mater. 2000;48:1105.
[20] Van Wilderen LJGW, Offerman SE, Van Dijk NH, Rekveldt MTh, Sietsma J, Van der Zwaag S. Appl. Phys. A 2002;74;1052.
[21] Offerman, SE, Van Wilderen LJGW, Van Dijk NH, Rekveldt MTh, Sietsma J, Van der Zwaag S. To be published in Physica B
[22] Aaronson HI, Lee JK. In: Lectures on the Theory of Transformations, TMS-AIME, Warrendale, PA, 1975.

[23] Jena AK, Chaturvedi MC. In: Phase Transformations in Materials, Prentice-Hall, London, 1992.
[24] Ågren J. Scripta Metall. 1986;20:841.
[25] Porter DA, Easterling KE. In: Phase Transformations in Metals and Alloys. London, Chapman & Hall; 1993. p. 101.
[26] Howell PR. Mat. Char. 1998;40: 227.
[27] Cahn JW. Trans. AIME 1957;209:140.
[28] Van Dijk, NH, Te Velthuis SGE, Rekveldt MTh, Sietsma J, Van der Zwaag S. Physica B 1999;267-268:88.
[29] Arrott AS, Heinrich B. J. Appl. Phys. 1981;52:2113.
[30] Rosman R, Rekveldt MTh. Phys. Rev. B 1991;43:8437.
[31] Zener C. J. Appl. Phys. 1949;20:950.
[32] Scheil E, Langeweise A. Arch. Eisenhttenw. 1937;11:93.
[33] Hull FC, Colton RA, Mehl RF. Trans. AIME 1942;150:185.
[34] Cahn JW, Hagel WC. In: Zackay VF, Aaronson HI editors. Decomposition of austenite by Diffusional processes 1962. Interscience, New York.
[35] Cahn JW. Mat. Res. Soc. Proc. 1996;398:425.
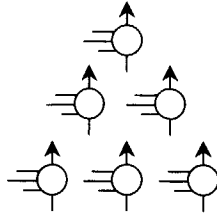
6. Evolving microstructures in carbon steel studied by x-ray diffraction microscopy

6.1. Grain Nucleation and Growth during Phase Transformations

S. E. Offerman, N. H. van Dijk, J. Sietsma, S. Grigull, E. M. Lauridsen, L. Margulies, H. F. Poulsen, M. Th. Rekveldt, and S. van der Zwaag, *Science*, 298 (2002) 1003 - 1005.

Abstract

The mechanical properties of polycrystalline materials are largely determined by the kinetics of the phase transformations during the production process. Progress in x-ray diffraction instrumentation at synchrotron sources has created an opportunity to study the transformation kinetics at the level of individual grains. Our measurements show that the activation energy for grain nucleation is at least two orders of magnitude smaller than that predicted by thermodynamic models. The observed growth curves of the newly formed grains confirm the parabolic growth model, but also show three fundamentally different types of growth. Insight into the grain nucleation and growth mechanisms during phase transformations contributes to the development of materials with optimal mechanical properties.

6.1.1. Introduction

Grain nucleation and growth are important phenomena in polycrystalline materials like metals and most ceramics. They govern the kinetics of many phase transformations and recrystallization processes that take place during processing. The final average grain size after the transformation is directly related to the strength of the material. In general a smaller average grain size results into a stronger material. Despite the various transformation models that have been proposed in the last 60 years, the kinetics of these phase transformations is still poorly understood. Most of these models are based upon the Classical Nucleation Theory (CNT) (*1*) and the law of parabolic grain growth as derived by Zener (*2*), which describe the behavior of individual grains in the bulk of the material.

The experimental techniques which have been available to verify these nucleation and growth models are either limited to observations at the surface or the determination of the average grain growth behavior in the bulk (*3*). The development of x-ray microscopes at synchrotron sources with focused high-energy x-rays has opened the opportunity to study individual grains in the bulk of a material (*4-7*). In addition, these measurements give unique information about the grain nucleation during the phase transformation. Due to a combination of fundamental scientific interest and technological importance the phase transformations in steel have been investigated more extensively than in any other material, and is the material studied here.

Carbon steel consists of iron and carbon (up to 2 wt.%) with small quantities of alloying elements, and exists in three stable crystalline phases: austenite with a face-centered cubic structure, ferrite with a body-centered cubic structure, and cementite (Fe_3C) with an orthorhombic structure. The principal transformation reaction in steel, which is a typical diffusion-controlled solid-state transformation, is from the high-temperature austenite phase to the low-temperature ferrite phase. Since the solubility of carbon in ferrite is much lower than in austenite, the transformation is accompanied by a carbon enrichment of the austenite. At lower temperatures the carbon-rich austenite decomposes into pearlite, which consists of a lamellar structure of two interpenetrating single crystals of ferrite and cementite, and is shown in Fig. 6.1.

6.1.2. Experimental

In order to study the time evolution of individual grains during the phase transformations, a relatively small volume of steel is illuminated with a monochromatic beam of hard x-rays from a synchrotron source. For the experiment we used the 3D X-Ray Diffraction Microscope (3DXRD) at beam line ID11 of the European Synchrotron Radiation Facility in transmission geometry. The energy of the monochromatic x-rays corresponds to 80 keV (wavelength of 1.55×10^{-2} nm), the beam size to 94×97 μm^2, and the thickness of the sample to 400 μm. By slightly rotating the sample around an axis perpendicular to the beam, a number of grains give rise to diffraction spots on a 2D-detector. Fig. 6.2 shows a diffraction pattern halfway through the austenite to ferrite transformation. From the standard diffraction theory it can be shown that the intensity of each spot is proportional to the volume of the grain it originates from.
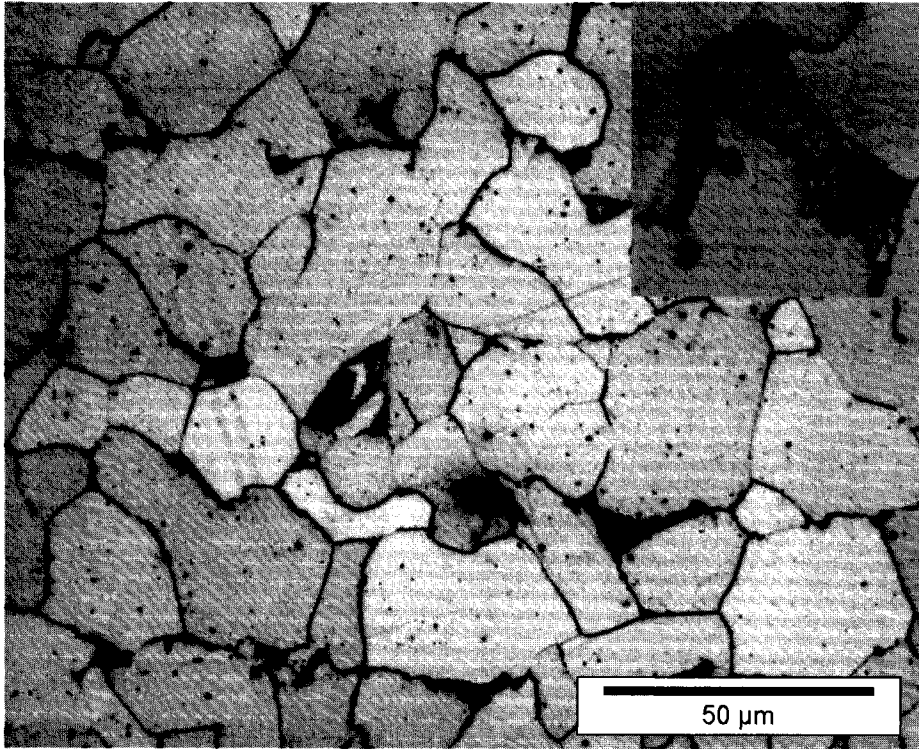
Fig. 6.1: Optical microscopy images of the construction steel (0.21 wt.% C, 0.51 wt.% Mn, 0.20 wt.% Si) at room temperature. The light regions correspond to ferrite and the dark regions to pearlite. The insert at the top right corner shows the lamellar structure of pearlite (3× main image).

During the exposure the sample is continuously rotated around the vertical axis over an angle from -0.8 ° to 0.8 °. In order to verify if a diffraction spot is valid, we took additional exposures for rotation angles from -2.4 ° to -0.8 ° and 0.8 ° to 2.4 °, which tell us whether the complete integrated intensity is observed in the central exposure. Once every six exposures the beam size is expanded to 139×139 μm^2 in order to check whether the total volume of the grain is illuminated by the small central beam. The intensity of the spot is normalized with respect to the total intensity of the diffraction ring at the end of the transformation (*4*), by assuming that the equilibrium ferrite fraction is then reached. By repeated acquisition of images the nucleation and growth of the individual grains is studied with a typical time resolution of 10 seconds.
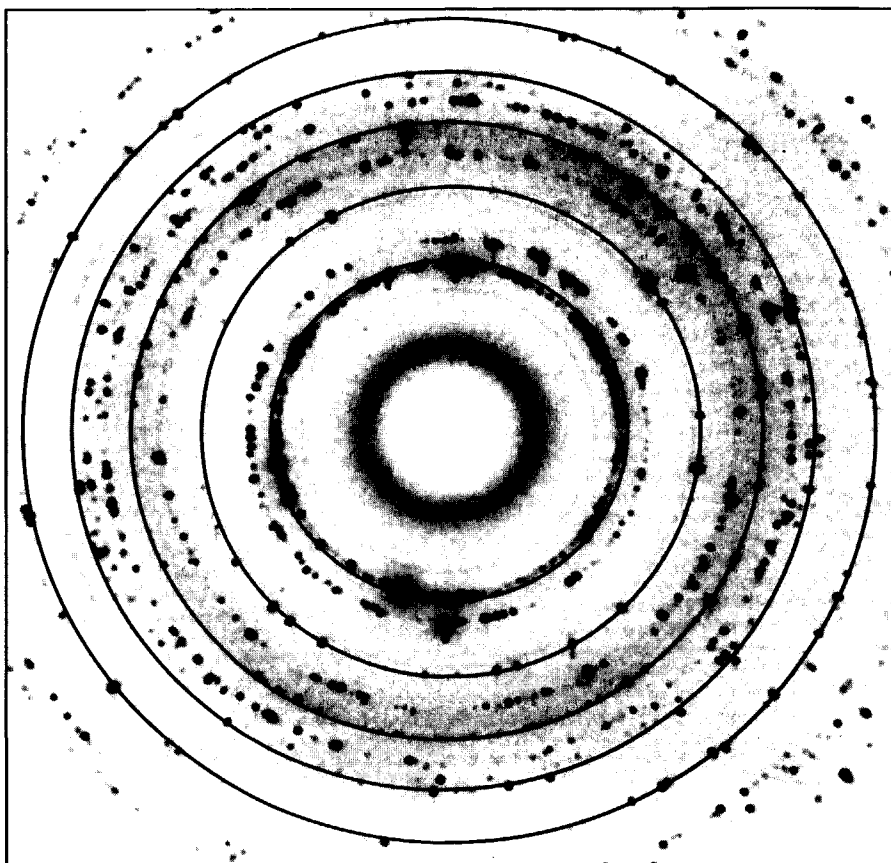
Fig. 6.2: X-ray diffraction pattern of the steel showing the austenite and ferrite reflections at 763 °C. The solid rings indicate the expected scattering angles from the ferrite grains illuminated by the x-ray beam.

6.1.3. Results and discussion

The steel was annealed at 900 °C for 10 min in order to form the austenite phase, and subsequently continuously cooled to 600 °C in 1 hour. By counting the number of valid diffraction spots, the number of ferrite grains (with a grain radius above the detection limit of about 2 μm) is obtained as a function of temperature, as shown in Fig. 6.3A. The number of ferrite nuclei increases most rapidly just below the austenite/ferrite transition temperature of 822 °C for this steel, but new ferrite nuclei are continuously formed over a large temperature range until the austenite/pearlite transformation starts at 685 °C.
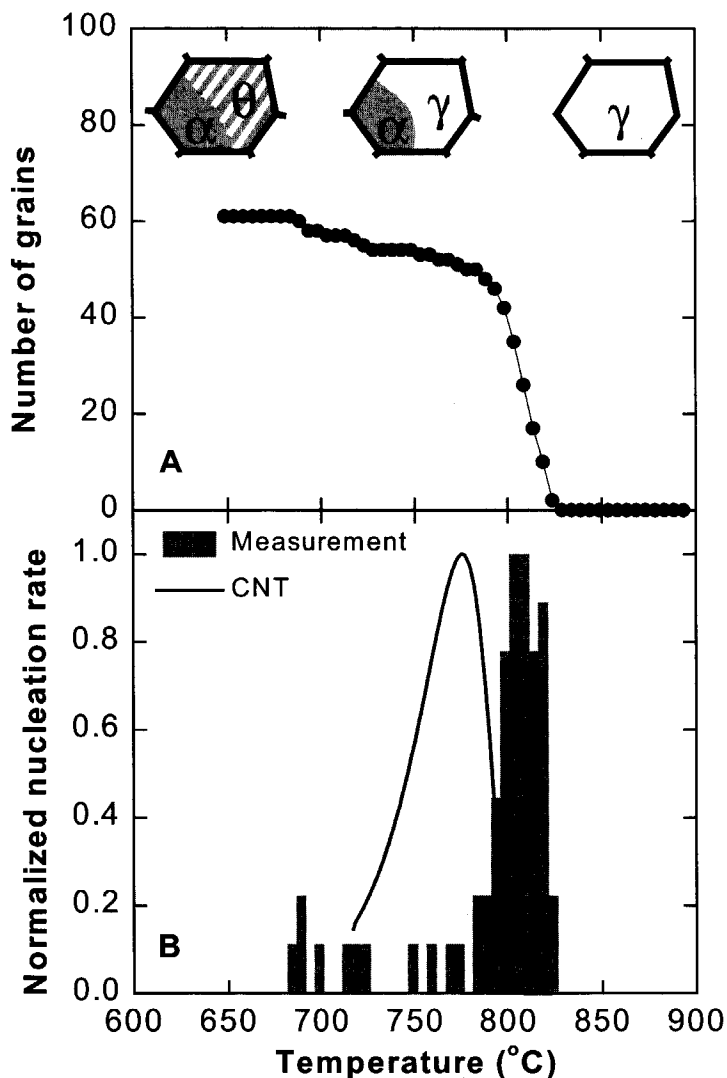
Fig. 6.3: Nucleation as a function of temperature during continuous cooling of the steel from 900 °C to 600 °C in 1 hour. A, The total number of valid ferrite reflections. B, The normalized experimental nucleation rate (bars) compared to the CNT (line) as given by Eq. 6.1. The different stages during the phase transformations in steel are schematically drawn at the top of the figure, which shows the three phases: Austenite (γ), ferrite (α), and cementite (θ).

Only a very small number of new pearlitic ferrite nuclei are formed at the pearlite transition temperature range. Fig. 6.3B shows the normalized experimental nucleation rate, which is compared to the CNT (1). The shape of the theoretical curve is in qualitative agreement with

the measurements. The most striking difference is that the maximum nucleation rate occurs at a higher temperature than predicted by the CNT.

According to the CNT the driving force for nucleation is the decrease in Gibbs free energy per unit volume of the system during the phase transformation Δg_V, which depends on the chemical composition and temperature. However, the creation of a new nucleus also requires energy due to the formation of an interface between the nucleus and the original phase. According to the CNT the nucleation rate can be expressed as:

$$\frac{dN}{dt} \propto (1-f)\frac{kT}{h}\exp\left[-\frac{\Delta G^* + Q_D}{kT}\right], \tag{6.1}$$

where the factor $(1-f)$ takes into account the decrease in the number of potential nucleation sites with increasing fraction f (in this case the ferrite fraction f^{α}), k is the Boltzmann constant, h the Planck constant, and T the temperature. The mobility of the (iron) atoms in the original (austenite) phase is taken into account by the activation energy for diffusion Q_D. The energy that is necessary to form a critical nucleus is referred to as the activation energy for nucleation ΔG^*, which can in general be written as $\Delta G^* = \Psi / \Delta g_V^2$. The factor Ψ accounts for the energy of the interface (boundary) between the nucleus and the original phase and the geometry of the nucleus.

It is the uncertainty in Ψ which makes predictions of the nucleation rate very difficult, and so models have been developed in order to estimate Ψ (8,9). These models have in common that a certain shape is assumed for the nucleus, which is then applied to all the nuclei in the system. One of the early models by Clemm and Fisher (8) predicts $\Psi_{CF} = 3.3 \times 10^{-3}$ J^3/m^6 for grain corner nucleation of nuclei with incoherent grain boundaries. A more recent model by Lange, et al. (9) gives $\Psi_{LEA} = 2.1 \times 10^{-6}$ J^3/m^6 for a pillbox shape of the nucleus with coherent and semi-coherent interfaces. A best fit of our experimental data to Eq. 6.1 gives $\Psi_{exp} = 5 \times 10^{-8}$ J^3/m^6, when $Q_D = 4.72 \times 10^{-19}$ J (10). This means that the activation energy for nucleation as determined in this experiment is at least two orders of magnitude smaller than the models predict.

In the calculation, the ferrite fraction f^{α} is assumed to develop according to thermodynamic equilibrium and was calculated from the thermodynamic database MTDATA®. The driving force for nucleation Δg_V is determined via the parallel-tangent construction with the standardized data from the Scientific Group Thermodata Europe (SGTE) under the assumption that the alloying elements are homogeneously distributed. For Ψ the value determined by Lange et al. (9) was used: $\Psi_{LEA} = 2.1 \times 10^{-6}$ J^3/m^6. The nucleation rate was normalized to the maximum nucleation rate.

The difference between experiment and theory can not solely be explained by varying Δg_V and/or Q_D within a realistic range. The low experimental value for the activation energy for nucleation indicates a close balance between the energy that is released by the removal of incoherent austenite/austenite grain boundaries and the energy that is required for the formation of coherent and incoherent austenite/ferrite grain boundaries. This could be related to recent computer simulations on the nucleation in a system of colloidal particles. These calculations indicate that it is possible that the initial nucleus has a metastable crystallographic structure, which transforms in a stable structure upon growth (11). Moreover, it may be questioned whether conventional continuum thermodynamics accurately predicts the driving force Δg_V, as the critical nucleus only consists of ten to hundred atoms.

We determined the growth behavior of individual ferrite grains and pearlite colonies by continuously monitoring the intensity of the diffraction spots as shown in Fig. 6.4. The ferrite

grain volume V^α that was derived from the measured intensity is transformed into a grain radius R^α by assuming a spherical grain shape. Four types of ferrite growth could be distinguished, as shown in the four panels of Fig. 6.4. In each panel the experimental growth curves are compared with the theoretical prediction of the classical Zener model (2), which predicts a parabolic growth for a spherical grain when the growth rate is limited by diffusion. This theory is commonly used to describe the growth of ferrite grains in construction steels during the transformation from austenite. As the solubility of carbon in ferrite is two orders of magnitude lower than in austenite, the carbon piles up at the moving interface and diffuses into the bulk of the austenite phase. This forms the rate-limiting process for the ferrite grain growth during the phase transformation. According to the Zener model, R^α as a function of time t is given by:

$$R^\alpha(t) = \chi\sqrt{D_C^\gamma(t-t_s)},\qquad\qquad(6.2)$$

where in the case of the austenite/ferrite transformation χ is a parameter which is determined by the carbon solubilities in ferrite and austenite, D_C^γ is the carbon diffusion coefficient in the bulk of the austenite, which depends on temperature and carbon concentration (12), and t_s is the moment of nucleation of the grain. Eq. 6.2 only applies to the initial stages of the transformation, during which the growth of the individual grain is not limited by interactions with neighboring grains due to overlapping diffusion fields (soft impingement) or existing grain boundaries (hard impingement).

The first and most frequently observed type of ferrite grain growth is initially in agreement with the theory, as shown in Fig. 6.4A. This means that the grains initially do not interact with growing neighboring grains. For each of the grains the growth curves start to deviate from the Zener theory at different levels, depending on the local impingement conditions. Fig. 6.4B shows the second type of growth, in which some ferrite grains continue to grow with the same crystallographic orientation during the pearlite formation as part of a pearlite colony. This remarkable behavior has so far only been observed by Thompson and Howell (13), who performed transmission electron microscopy measurements at the interface between ferrite and pearlite. This mechanism of continued growth of pre-existing ferrite appears to be the dominant mechanism for pearlite formation. This is evidenced by the fact that very few new pearlite nuclei were found in the pearlite transformation temperature range (Fig. 6.3A). These growth curves also show that the pearlite colony reaches a larger final size when the initially formed ferrite grain is smaller. Another difference between the austenite/ferrite and austenite/pearlite transformation is that at the low imposed cooling rate all the pearlite colonies start to grow at a well-defined temperature of 685 °C for this steel. Once pearlite formation is initiated the intercalated cementite takes up all the carbon, which increases the growth rate.

The final two types of grain growth have not been observed or postulated before. Fig. 6.4C shows the third type of ferrite growth, in which the ferrite nucleation and growth are retarded. An enrichment of carbon in the austenite causes a local decrease in transition temperature, which leads to a retarded nucleation. The retarded growth is caused by an indirect interaction with growing neighboring grains. The neighboring grains do not directly touch each other, but interfere via surrounding diffusion and stress fields (14). The last class of ferrite grain growth is characterized by a complex growth behavior, as shown in Fig. 6.4D.
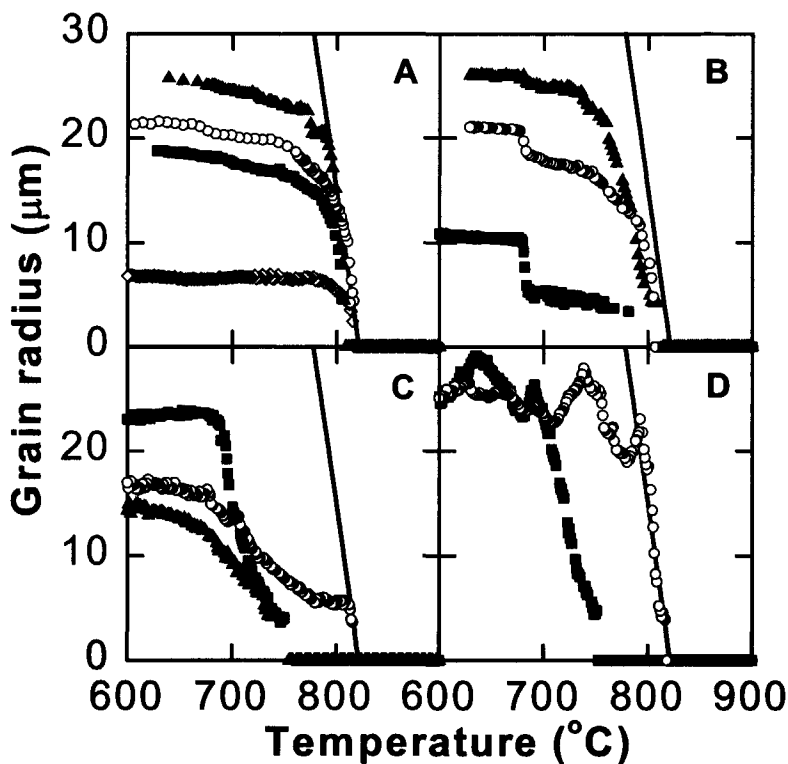
Fig. 6.4: Particle radius of individual ferrite grains as a function of temperature during continuous cooling of the steel from 900 °C to 600 °C in 1 hour. A, Ferrite grains that started to grow according to the classical Zener theory (line). B, Ferrite grains that continued to grow with the same crystallographic orientation during the pearlite formation as part of a pearlite colony. C, Retarded ferrite growth. D, Complex ferrite growth.

In this least frequently observed growth mode, ferrite grains not only grow, but also temporarily shrink upon continued transformation. This behavior is due to a complex grain-boundary migration caused by a direct interaction with neighboring grains. The neighboring grains directly touch, but their grain boundaries are not yet in their equilibrium position. It is known that some grain boundaries are more stable than others depending on the curvature (15). As the growth is a dynamic process, the forces on the grain boundaries may change irregularly, resulting in the growth behavior shown in Fig. 6.4D. Thus, on the level of individual grains we can distinguish four types of grain growth. There are grains that do not interact with neighboring grains, grains that continue to grow with the same crystallographic

orientation into another phase, grains that indirectly interact, and grains that directly interact with neighboring grains.

6.1.4. Conclusions

Our measurements show that the activation energy for grain nucleation is at least two orders of magnitude smaller than that predicted by thermodynamic models. The observed growth curves of the newly formed grains confirm the parabolic growth model, but also show three fundamentally different types of growth. We conclude that the current models do not accurately predict the phase transformation kinetics in polycrystalline materials. Future nucleation models should give a better prediction of the optimum size and shape of the critical nucleus, which initially may have a metastable crystallographic structure, with respect to the energy of the interfaces. Future growth models should incorporate the interactions between growing neighboring grains. From a technological perspective these new insights are of importance to the modern materials production process, which relies heavily on grain nucleation and growth models to produce tailor-made materials.

Acknowledgement

References

[1] J. W. Christian, *The Theory of Transformations in Metals and Alloys* (Pergamon Press, Oxford, 1981).
[2] C. Zener, *J. Appl. Phys.* **20**, 950 (1949).
[3] C. E. Krill III *et al., Phys. Rev. Lett.* **86**, 842 (2001).
[4] E.M. Lauridsen, D.J. Jensen, H.F. Poulsen, U. Lienert, *Scripta Mater.* **43**,561 (2000).
[5] L. Margulies, G. Winther, H. F.Poulsen, *Science* **292**, 2392 (2001).
[6] H.F. Poulsen *et al., J. Appl. Crystallogr.* **34**, 751 (2001).
[7] B.C. Larson, W. Yang, G.E. Ice, J.D. Budal, J.Z. Tischler, *Nature* **415**, 887 (2002).
[8] P.C. Clemm, J.C. Fisher, *Acta Metall.* **3**. 70 (1955)
[9] W. F. Lange III, M. Enomoto, H. I. Aaronson, *Metall. Trans. A* **19A**, 427 (1988).
[10] J. Kučera, K. Stránský, *Mater. Sci. Eng.* **52**, 1 (1982).
[11] S. Auer, D. Frenkel *Nature* **409**, 1020 (2001).
[12] J. Ågren, *Scripta Metall.* **20**, 1507 (1986).
[13] S.W. Thompson, P.R. Howell, *Scripta Metall.* **22**, 1775 (1988).
[14] M. Onink, F.D. Tichelaar, C.M. Brakman, E.J. Mittemeijer, S. van der Zwaag, *J. Mater. Sci.* **30**, 6223 (1995).
[15] D.A. Porter and K.E. Easterling, *Phase Transformations in Metals and Alloys* (Chapman & Hall, London, 1981).

6.2. In-situ observation of individual austenite grains transforming into ferrite and pearlite

6.2.1. Introduction

Section 6.1 described the austenite decomposition into ferrite and pearlite in medium carbon steel that was studied by 3DXRD microscopy [1]. In section 6.1, the diffraction spots of ferrite were analyzed, which has led to a classification of four types of ferrite grain growth: 1) Ferrite grains that started to grow according to the classical Zener theory, 2) Ferrite grains that continued to grow with the same crystallographic orientation during the pearlite formation as part of a pearlite colony, 3) Retarded ferrite growth, and 4) Complex ferrite growth. In this section the austenite diffraction spots are analysed of the same 3DXRD microscopy measurements presented in section 6.1, in which the two continuous cooling experiments were performed on the same specimen.

6.2.2. Results and discussion

Fig. 6.5 shows the measured ferrite (f^α) and austenite (f^γ) volume fractions as a function of temperature compared to the equilibrium fractions as calculated from the thermodynamic database MTDATA$^\circledR$. The calculated transition temperature from austenite to ferrite is $A_3 = 826°C$ and the upper and lower transition temperatures from austenite to cementite are $A_1^+ = 718°C$ and $A_1^- = 711°C$, respectively. The final ferrite fraction at the end of the transformation as calculated with MTDATA$^\circledR$ is $f_f^\alpha = 0.98$, which includes the pearlitic ferrite. The measured ferrite fraction is obtained by averaging the intensities of the three $\Delta\omega$–scans of the (200) powder ring that were measured each time the beam size was extended to 140×140 μm^2 (see eqn. (3.40)). This average intensity $\langle I \rangle$ was then normalized to the intensity at the end of the transformation $\langle I \rangle_f$ and multiplied by the final ferrite fraction at the end of the transformation that is calculated with MTDATA$^\circledR$, leading to:

$$f^\alpha = \frac{\langle I \rangle}{\langle I \rangle_f} f_f^\alpha.$$

(6.3)

Each ferrite fraction in Fig. 6.5 is the average of the ferrite fractions obtained from the (200) and (211) powder rings for each continuous cooling experiment. In an analogous manner the austenite fractions of Fig. 6.5 are determined from the (200) and (220) reflections of the austenite powder rings.

Fig. 6.5 shows that the ferrite and austenite fractions change approximately according to thermodynamic equilibrium during the austenite to ferrite phase transformation. The difference between the starting temperature for the increase of the ferrite fraction and the decrease of the austenite fraction is the result of the small number of ferrite grains and the large number of austenite grains that are present at the start of the transformation. The intensity from a small number of ferrite grains is more difficult to distinguish from the background of the powder ring, than the intensity of a large number of austenite grains.
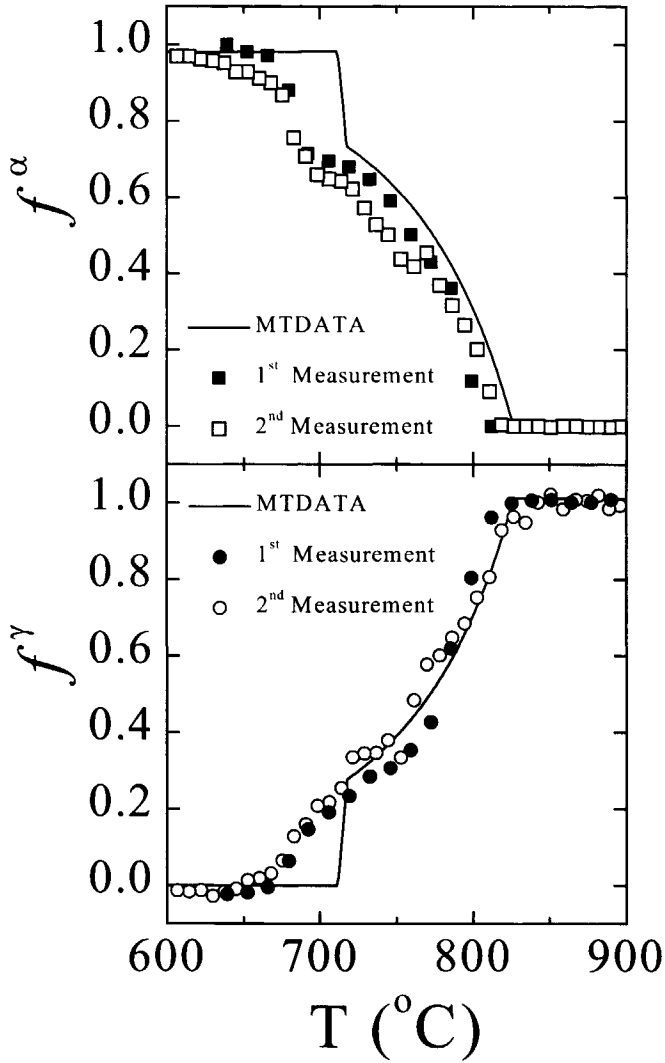
Fig. 6.5: The measured ferrite (f^α) and austenite (f^γ) volume fractions as determined from the intensity of the powder rings compared to the equilibrium fractions as determined from MTDATA®.

The difference in fraction between the two measurements results from the relatively small beam size and $\Delta\omega$–range that was used compared to a powder measurement in which the sample is rotated over 360° and a larger beam is used. In the latter case more grains

103

contribute to the intensity of the powder rings. The previous analysis of the individual ferrite grains [1] (see Fig. 6.4) showed that the austenite to pearlite phase transformation started at precisely 685°C (see also Fig. 6.5), which is at least 33°C lower than the thermodynamic equilibrium transition temperature range that was calculated from MTDATA®. This is possibly related to the relatively high energy barrier for the nucleation of pearlitic cementite compared to the nucleation of pro-eutectoid ferrite, as discussed in sections 5.4 and 6.1.

Figs. 6.6 to 6.8 show the transformation behavior of single austenite grains in comparison with the first three types of ferrite grain growth. The curves of the transforming austenite grains in Figs. 6.6 to 6.8 are nearly the mirror image of the first three types of ferrite grain growth. An important reason that they are not the exact mirror image is that the austenite grains do not transform into the same ferrite grains to which they are compared. The ferrite grain in which the austenite grain transformed is most probably not in reflection and therefore not measured. However, Figs. 6.6 to 6.8 suggest that each transforming austenite grain has a mirror image of a growing ferrite grain for the present heat-treatment of this medium carbon steel.

Fig. 6.6 shows a single austenite grain that transformed into a ferrite grain that started to grow according to the classical Zener theory of diffusional grain growth (represented by the solid line) [2]. During the initial stages of the transformation, in which the growth of an individual ferrite grain is not limited by interactions between neighboring grains due to overlapping diffusion fields (soft impingement) or existing grain boundaries (hard impingement), the radius of a ferrite grain R^α as a function of time t is given by the Zener model as

$$R^\alpha(t) = \chi \sqrt{D_{C,V}^\gamma (t - t_s)}, \tag{6.4}$$

where t_s is the moment of nucleation of the grain and χ is a parameter that is determined by the carbon solubilities in ferrite and austenite and can be approximated by [3]

$$\chi = 2.102 \left(\frac{C_\infty^\gamma - C_{eq}^\gamma}{C_{eq}^\alpha - C_\infty^\gamma} \right)^{0.5871}, \tag{6.5}$$

where C_{eq}^α and C_{eq}^γ are the equilibrium carbon concentrations in ferrite and austenite, respectively, obtained form the phase diagram, and C_∞^γ is the carbon concentration in the austenite matrix far away form the austenite/ferrite interface. In a first approximation the carbon concentration in the austenite matrix far away form the austenite/ferrite interface C_∞^γ equals the initial or average carbon concentration C_0.

The volume diffusion coefficient of carbon in austenite $D_{C,V}^\gamma$ depends on the temperature and the nominal carbon concentration and can be described by [4]

$$D_{C,V}^\gamma = 4.53 \times 10^{-7} \left(1 + Y_C(1 - Y_C) \frac{8339.9}{T} \right) \exp \left\{ -\left(\frac{1}{T} - 2.221 \times 10^{-4} \right)(17767 - 26436 Y_C) \right\}, \tag{6.6}$$

where $D_{C,V}^\gamma$ is in m²/s and the temperature T in K. The site fraction Y_C of carbon on the interstitial sub-lattice is given by
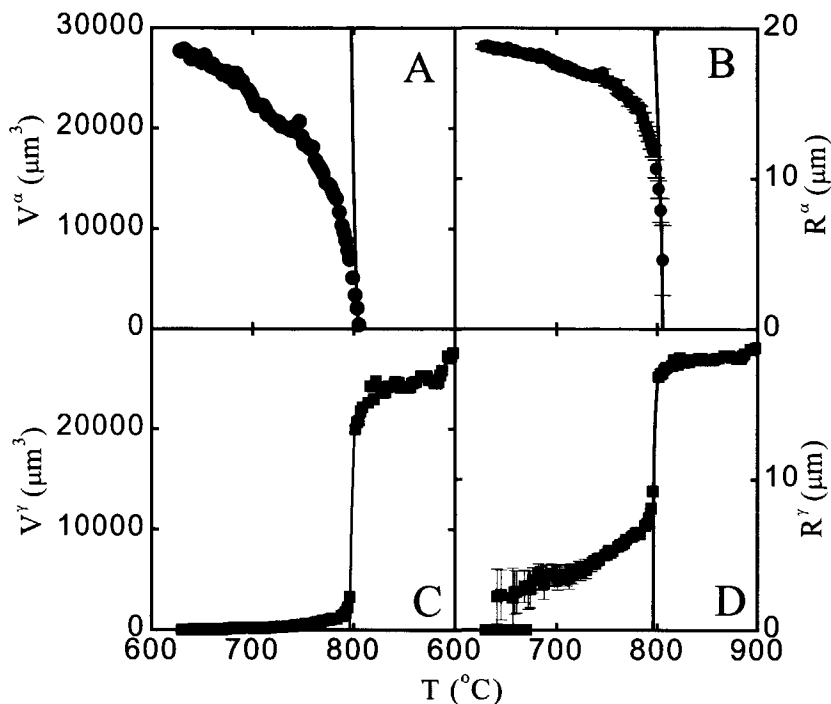
Fig. 6.6: The grain volume (A) and radius (B) of a single ferrite grain that started to grow according to the classical Zener theory. The grain volume (C) and radius (D) of a single austenite grain that seems to have transformed into a single ferrite grain that started to grow according to the classical Zener theory of diffusional grain growth (represented by the solid line). The austenite grain and the ferrite grain are not related. The measured grain volume is converted into a grain radius under the assumption that the grains are spherical.

$$Y_C = \frac{x_C}{1 - x_C}, \tag{6.7}$$

where x_C (≈ 0.00985) is the overall atom fraction of carbon in the alloy.

The austenite grain in Fig. 6.6 transforms probably completely into one single ferrite grain (within the detection limit of about $R^\gamma \approx 2$ μm). In the case that two ferrite grains would start to grow at the same time, in the same austenite grain, at a rate predicted by the Zener theory, the austenite grain would transform two times faster than shown in Fig. 6.6. In the case that two ferrite grains would nucleate at different times, this would be visible as an extra decrease in austenite grain size at the moment that the second ferrite grain starts to grow, which is apparently not the case in Fig. 6.6. For the same reason there is not another ferrite grain that nucleated in a neighboring austenite grain that continued to grow in the austenite grain of Fig. 6.6. Furthermore, it is unlikely that two ferrite grains grow slowly in the same

105

austenite grain, like the third type of ferrite grain growth that was shown in Fig. 6.4C, and thereby result in the decrease in austenite grain size that corresponds to the Zener theory, as shown in Fig. 6.6. Therefore, only one ferrite grain nucleates in the austenite grain, which is in good agreement with the findings of Militzer *et al.* [5], who estimate the number N_γ^α of ferrite grains nucleated per austenite grain as

$$N_\gamma^\alpha = f_f^\alpha \left(\frac{d_\gamma}{d_\alpha}\right)^3 \qquad (6.8)$$

where f_f^α is the final fraction of pro-eutectoid ferrite at the end of the transformation, and d_γ and d_α are the austenite and ferrite grain size, respectively. For our measurements $f_f^\alpha \approx 0.8$ and $d_\gamma \approx d_\alpha$, which gives $N_\alpha = 0.8$. This means that eqn. (6.7) predicts that approximately one ferrite grain nucleates per austenite grain, as we have observed.

The austenite grain in Fig. 6.6 did not transform into pearlite (within the detection limit of about $R^\gamma \approx 2$ μm), because there is not a sharp decrease in the austenite grain volume at 685°C that would indicate the formation of pearlite (see e.g. Fig. 6.7). This can be the result of two processes. Firstly, the carbon atoms may not be homogeneously distributed over the austenite grains before the transformation. This can be the case if alloying elements that attract or repel carbon atoms are not homogeneously distributed. The high mobility of carbon atoms at the austenizing temperatures can thereby lead to an inhomogeneous equilibrium distribution of carbon atoms in the austenite phase before the transformation. Secondly, the carbon atoms can diffuse out of the transforming austenite grain into neighbouring austenite grains. These processes are known to take place during the formation of ferrite/pearlite bands (see chapter 4) [6] in which the final microstructure after the transformation consists of alternating bands of ferrite and pearlite. In order to form microstructural bands the carbon needs to diffuse over distances that are of the order of the several austenite grains. The high mobility of carbon atoms along grain boundaries [7] can result in a fast redistribution of the carbon atoms during the transformation. Fig. 6.6 shows that the carbon atoms do not only diffuse between austenite grains in steel that transformed into a microstructure consisting of ferrite/pearlite bands, but also in medium carbon steel that transformed into a microstructure consisting of a random spatial distribution of ferrite grains and pearlite colonies.

The austenite grain in Fig. 6.6 transforms into a ferrite grain that starts to grow according to the Zener theory, but retards at a later stage. This retardation at a later stage of the transformation can not be the result of carbon enrichment of the austenite grain, because then the austenite grain would transform into pearlite at 685°C. It is unlikely that the solute drag accounts for the retardation of the transformation, because in that case it should also have taken place during the first stage of the transformation. Therefore, the ferrite grain that grows inside the austenite grain impinges onto the former austenite/austenite grain boundary and thereby retards the transformation of the austenite grain.

Fig. 6.7 shows a single austenite grain that transformed into ferrite and at 685°C the remaining part of the austenite grain transformed into pearlite. As was observed for the growth of pro-eutectoid ferrite grains that continued to grow into a pearlite colony during the pearlite transformation, the austenite grain transforms at precisely 685°C into pearlite for the current medium carbon steel and heat-treatment. During the transformation of an austenite grain into ferrite the remaining austenite grain enriches in carbon, because the solubility of carbon is much lower than the average carbon concentration of the steel. As the remaining austenite grain reaches the eutectoid composition of approximately 0.77 wt.% of carbon, it is

likely to transform into pearlite. The remaining austenite grain volume V_{eut}^γ at which the eutectoid carbon composition is reached can be estimated from the austenite grain size before the transformation V_0^γ as

$$V_{eut}^\gamma = \frac{C_0 - C_{eq}^\alpha}{C_{eut} - C_{eq}^\alpha} V_0^\gamma \tag{6.9}$$

where C_0 is the average carbon concentration, C_{eq}^α is the equilibrium carbon concentration in the ferrite (approximately 0.02 wt.% C) and C_{eut} = 0.77 wt.% C is the eutectoid carbon concentration. In the case that 1) The carbon atoms are homogeneously distributed over all the austenite grains before the transformation, 2) The carbon atoms remain in the same austenite grain during the transformation, and 3) The average carbon concentration of the steel is C_0 = 0.214 wt.% C, approximately one quarter of the original austenite grain would transform into pearlite (see also the ferrite fraction in Fig. 6.5).

However, Fig. 6.7C shows that less than a quarter of the original austenite grain transformed into pearlite. This is the result of either an inhomogeneous distribution of carbon atoms before the transformation, or the carbon atoms could have diffused to neighbouring austenite grains during the transformation, or both processes take place. The same processes probably took place during the growth of the small pro-eutectoid ferrite grain in Fig. 6.7B that continued to grow into a much larger pearlite colony. In the case that this ferrite grain is the mirror image of a transforming austenite grain, the original austenite grain volume transformed for approximately three quarters into pearlite. Another explanation could be that this pealite colony crossed a former austenite/austenite grain boundary and grew into a neighbouring austenite grain that was enriched in carbon. Pearlite colonies have been observed before to cross austenite/austenite grain boundaries [8].

Fig. 6.8 shows a single austenite grain that slowly transformed completely into a single ferrite grain. The austenite grain did not transform into pearlite within the detection limit. The retarded transformation with respect to the Zener theory is likely the result of an enriched carbon concentration in the austenite grain.

None of the transforming austenite grains in the data set was the mirror image of the fourth type of ferrite grain growth (see Fig. 6.4D). An austenite grain of the fourth type would display a oscillating grain volume as a function of temperature during continuous cooling. This observation supports our earlier hypothesis that the complex ferrite grain growth, as shown in Fig. 6.4D, is the result of a direct interaction between ferrite grains rather than a reversed transformation into austenite [1].

The inhomogeneous carbon distribution before the transformation and the carbon diffusion between neighboring austenite grains during the transformation has serious consequences for the predictability of the austenite decomposition in steel by single-grain models. Single-grain models have the advantage over multi-grain phase transformation models that they can calculate the phase transformation kinetics in great detail without too much computer time. The single-grain model of Vandermeer [9] describes a spherical austenite grain that transforms into a shell of ferrite on the austenite grain boundary that thereafter grows towards the center. A more realistic model was recently developed by Van Leeuwen *et al.* [10], who describe an austenite grain that has the shape of a tetrakaidecahedron, which closely resembles the average geometry of an austenite grain.
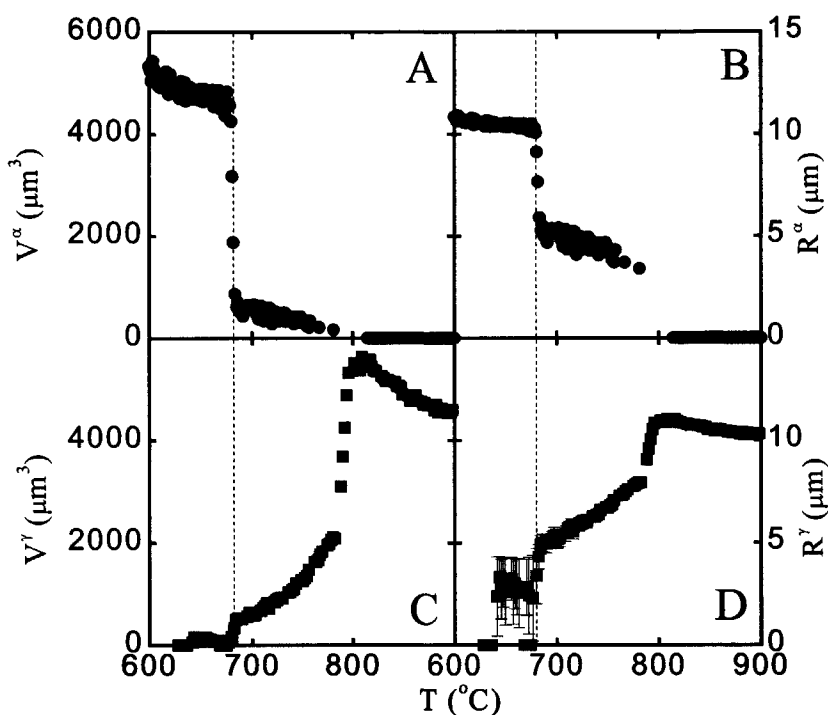
Fig. 6.7: The grain volume (A) and radius (B) of a single pro-eutectoid ferrite grain that continued to grow with the same crystallographic orientation during the pearlite formation as part of a pearlite colony. The grain volume (C) and radius (D) of a single austenite grain that seems to have transformed into ferrite and at 685 °C the remaining part of the austenite grain transformed into pearlite. The austenite and ferrite grain are not related. The dotted line indicates the temperature at which the austenite transforms into pearlite. The measured grain volume is converted into a grain radius under the assumption that the grains are spherical.

The principal advantage of this model over the Vandermeer model is that it takes into account that grain corners are more favorable centers for nucleation than grain edges and boundaries. However, an intrinsic drawback of all single-grain models is that they do not take into account the carbon diffusion between neighbouring austenite grains. The measurements on single austenite grains that are presented here show that the carbon distribution over the austenite grains before and during the transformation significantly influences the transformation kinetics.
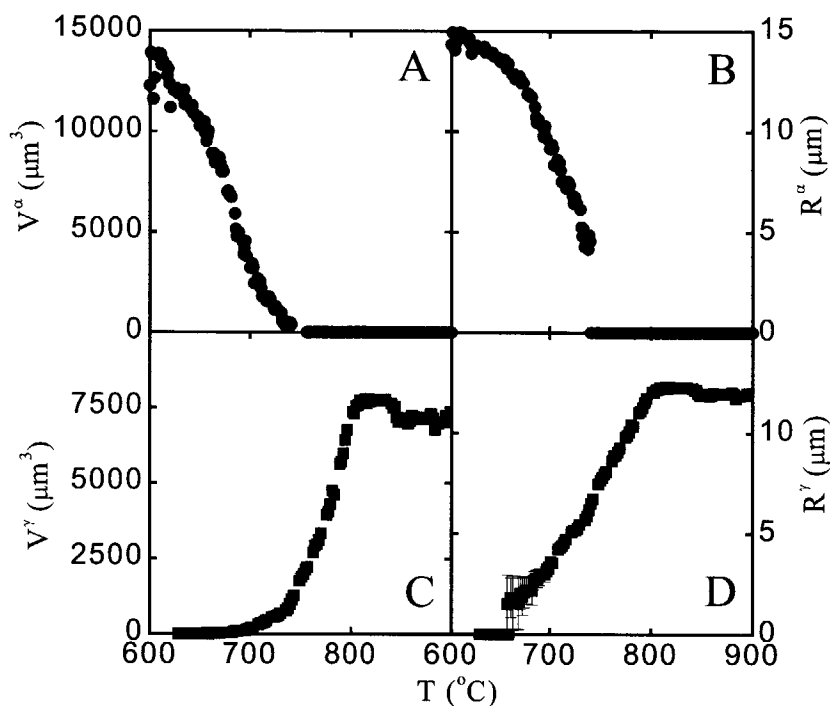
108

Fig. 6.8: The grain volume (A) and radius (B) of a single pro-eutectoid ferrite that displays retarded grain growth with respect to the classical Zener theory of diffusional grain growth. The grain volume (C) and radius (D) of a single austenite grain that slowly transformed into ferrite. The measured grain volume is converted into a grain radius under the assumption that the grains are spherical.

6.2.3. Conclusions

The kinetics of individual austenite grains transforming into ferrite and pearlite was studied during continuous cooling of medium carbon steel by means of the 3DXRD microscope at the ESRF synchrotron. The measurements show that the transforming austenite grains are nearly the mirror image of the first three types of ferrite grain growth. The measurements indicate that not more than one ferrite grain nucleated in a single austenite grain. There are austenite grains that transformed completely into ferrite and austenite grains that transformed into ferrite and pearlite. This shows that the carbon atoms are not homogeneously distributed over the austenite grains before the transformation and that the carbon atoms diffuse between neighbouring austenite grains during the transformation, which significantly influences the transformation kinetics. This has serious consequences for the predictability of the austenite decomposition in steel by single-grain models.

109

References

[1] S.E. Offerman, N.H. van Dijk, J. Sietsma, S. Grigull, E.M. Lauridsen, L. Margulies, H.F. Poulsen, M. Th. Rekveldt, and S. van der Zwaag, *Science*, 298 (2002) 1003.

[2] C. Zener, *J. Appl. Phys.*, 20 (1949) 950.

[3] S.G.E. te Velthuis, *Phase transformations in steel, a Neutron depolarization study*, PhD thesis, Delft University of Technology, 1999.

[4] J. Ågren, *Scripta Metall.*, 20 (1986) 841.

[5] M. Millitzer,R. Pandi, and E.B. Hawbolt, *Metall. Mater. Trans. A*, 27A (1996) 1547.

[6] S. E. Offerman, N. H. van Dijk, M. Th. Rekveldt, J. Sietsma, and S. van der Zwaag, *Mater. Sci. Technol.*, 18 (2002) 297-303.

[7] D.A. Porter and K.E. Easterling, In: *Phase Transformations in Metals and Alloys*, London, Chapman & Hall, 1993.

[8] P.R. Howell, *Mat. Char.*, 40 (1998) 227.

[9] R. A. Vandermeer, *Acta Metall. Mater.*, 38 (1990) 2461.

[10] Y. van Leeuwen, S. Vooijs, J. Sietsma, and S. van der Zwaag, *Metall. Mater. Trans. A*, 29A (1998) 2925.
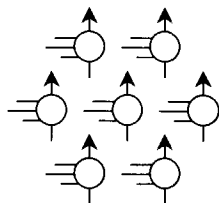
7. High temperature SANS experiments on Nb(C,N) and MnS precipitates in HSLA steel

N.H. van Dijk, S.E. Offerman, W.G. Bouwman, M.Th. Rekveldt, J. Sietsma, S. van der Zwaag, A. Bodin, and R.K. Heenan, *Metall. Mater. Trans. A*, 33A (2002) 1883 – 1891.

Abstract

The volume distribution of precipitates in high-strength low-alloy (HSLA) steels has been studied using small-angle neutron scattering (SANS) at high temperatures. Three samples with different niobium concentrations (0.00, 0.05, and 0.10 wt.%) were slowly heated from a temperature of 910 to 1200 °C. With increasing temperatures, the scattered intensity strongly decreases as the precipitates gradually dissolve or coarsen. A comparison between the particle distribution of the 3 different materials suggests that the particles with a radius below 10 nm mainly correspond to Nb(C,N) precipitates and the larger particles to MnS precipitates. Subsequent cooling from 1200 to 910 °C only leads to a small increase in the scattered intensity. Quenching from the austenite to the ferrite phase and reheating to the austenite phase, however, produces a large increase in the formation of the small precipitates with a radius below 10 nm.

7.1. Introduction

Grain refinement is a powerful metallurgical mechanism to improve the mechanical properties of a material. Both strength and toughness properties increase with decreasing grain size. In hot rolling of high-strength low-alloy (HSLA) steels, a combination of two metallurgical mechanisms is applied to reduce the final grain size of the material: thermo-mechanical rolling and accelerated cooling. Thermo-mechanical rolling involves rolling in the temperature region where the austenite no longer recrystallises after each rolling pass in the finishing mill. This results in accumulated strains over several passes, which is a favourable condition for the following accelerated cooling on the run-out table, usually with water. The heavily deformed austenite has a large interfacial area, and sometimes pronounced intragranular deformation bands, which act as additional sites for ferrite nucleation during the allotropic phase transformation.

By adding small amounts of niobium (usually less than 0.05 wt.%) to low-alloy steels, the temperature below which no recrystallisation of the austenite takes place is increased. This allows higher accumulated strains in the austenite range and hence leads to smaller ferrite grain sizes being formed during accelerated cooling. Whether the recrystallisation is retarded as a result of the drag by solute niobium atoms [1] or by the pinning forces exerted by small Nb(C,N) precipitates [2], is still a matter of debate. The theory combining both explanations is that the solute drag retards recrystallisation and this allows sufficient time for the Nb(C,N) precipitates to form [3]. Further precipitation may occur upon slow cooling to ambient temperature after coiling of the steel in the hot strip mill. The formation and dissolution of the precipitates in the austenite has been studied quite extensively using ex-situ techniques like transmission electron microscopy (TEM) and chemical dissolution [4-8]. A major complication in ex-situ observations is the unavoidable austenite-ferrite phase transformation. Nb(C,N) precipitates which were not present in the austenite may form upon cooling due to the reduced solubility in ferrite. Hence it would be highly desirable to obtain in-situ information on the Nb(C,N) precipitates in austenite.

In this study, small-angle neutron scattering (SANS) experiments have been performed to study the dissolution and (re-)precipitation behaviour of Nb(C,N) in the temperature range of 900-1200 °C. Notwithstanding its experimental complications in determining the origin of the scattering unambiguously, SANS is a very versatile technique for studying the particle-size distribution of scattering inhomogeneities of the order of 1-100 nm [9]. The technique has successfully been used in the study of carbide precipitation in ultrahigh strength steels [10]. A big advantage of SANS is that the whole sample volume can be studied in-situ, because the sample has a relatively large transmission length for neutrons. Scattering can be the result of structural or magnetic differences of the particles relative to the matrix. As the matrix phase is single-phase austenite in the temperature range of interest (900-1200 °C), only nuclear scattering from the precipitates needs to be considered. At lower temperatures polarised neutrons could be used in the SANS measurements to analyse the magnetic scattering from ferrite grains in the matrix, as was recently demonstrated for martensitic steel [11]. For the experiments in this study, silicon-killed laboratory casts were prepared with different niobium contents, containing as small amounts of other alloying elements as possible. As these casts also contain small amounts of manganese and sulphur, the simultaneous formation of small MnS precipitates could not be avoided.

7.2. Experimental

Three silicon-killed HSLA steels (Nb0, Nb5, and Nb10) with different niobium concentrations were cast and hot-rolled at CORUS RD&T. The chemical composition of the three steels is listed in Table 7.1. The rolled material was machined and polished into flat sheets of about 1 mm thick and cut into platelets of 18×25 mm^2. In order to prevent decarburisation of the steel at the high annealing temperatures during the experiment, the surface was coated with a 2 μm thick nickel layer by means of electrochemical deposition. In the experiments we studied steel samples of Nb0, Nb5, and Nb10 with a sample thickness of 2.70, 2.85, and 2.55 mm, respectively. The steels were placed in a custom-made sample holder of tantalum foil, which was mounted in a radiation furnace at high vacuum (10^{-5} mbar). Under these experimental conditions the average heating and cooling rate of the samples was about dT/dt = 100 $^\circ$C/min for the temperature range of interest (500 $^\circ$C $< T <$ 1200 $^\circ$C).

The small-angle neutron scattering measurements have been performed on the LOQ instrument at ISIS [12] with fixed moderator-sample (L_{m-s} = 10.96 m) and sample-detector (L_{s-d} = 4.19 m) distances. A circular neutron beam with a diameter of 11 mm was used in all experiments. We have restricted the wavelength range for our data collection to 0.425 nm $< \lambda < 1$ nm in order to avoid a possible contribution of multiple Bragg scattering from the austenite crystal structure. The beam centre was determined from an empty beam measurement at the start of the experiment. The wavelength dependent sample transmission was determined from the direct-beam intensity of the empty sample holder and of the mounted sample. The transmission of the mounted sample was determined for each sample condition. The background scattering of the furnace (with and without the sample holder) was measured at room temperature and assumed to be temperature independent.

As schematically shown in Fig. 7.1, a sample consisting of small particles embedded in a matrix can cause scattering of the incoming neutron beam. For elastic scattering of neutrons with a wavelength λ, the scattering angle 2θ is related to the wave vector transfer Q (and the momentum transfer $\hbar Q$) by

$$Q = \frac{4\pi}{\lambda} \sin(\theta) . \qquad (7.1)$$

The wave vector transfer Q is inversely proportional to a scattering length $2\pi/Q$ which is characteristic for the scattering particles. When the particle size is relatively large compared to the neutron wavelength λ (0.425 - 1 nm) the scattering is predominantly found at small angles. The scattered intensity $I(Q)$ as a function of Q can generally be described as

$$I(Q) = I_0 \Delta\Omega \eta T V \left(\frac{d\Sigma}{d\Omega} \right)(Q) , \qquad (7.2)$$

where I_0 is the incoming neutron flux, $\Delta\Omega$ the probed solid angle element, η the detector efficiency, T the sample transmission, V the sample volume in the neutron beam, and (dΣ/dΩ)(Q) the macroscopic differential scattering cross-section. After correcting for the background scattering from the furnace and the sample holder, the macroscopic scattering cross-section of the sample can be deduced from the scattered intensity [13].

Table 7.1: Chemical composition of the steel samples in wt.%.

	C	Si	Mn	Nb	S	P	Cr	Ni	Cu	N	Al
Nb0	0.082	0.484	0.067	<0.002	0.029	0.007	0.010	0.023	0.004	0.0035	<0.003
Nb5	0.082	0.519	0.090	0.049	0.004	0.007	0.012	0.023	0.005	0.0034	<0.003
Nb10	0.076	0.526	0.086	0.097	0.004	0.006	0.012	0.023	0.005	0.0032	<0.003
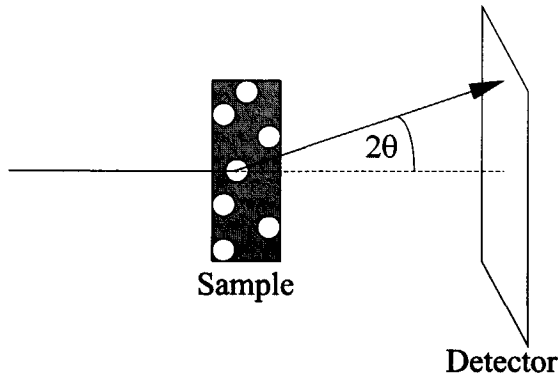
Fig. 7.1: Layout of the small-angle neutron scattering technique. The neutrons scatter from inhomogeneities in the sample over a scattering angle 2θ and are detected by a two-dimensional area detector.

The macroscopic differential scattering cross-section characterises the scattering power of the particles in the matrix and is given for dilute systems by

$$\left(\frac{d\Sigma}{d\Omega}\right)(Q) = (\Delta\rho)^2 \int_0^\infty V(R)D_V(R)|F(Q,R)|^2 \, dR, \qquad (7.3)$$

where $\Delta\rho = \rho_p - \rho_\gamma$ is the contrast in neutron scattering length density of the precipitates ρ_p and the austenite matrix ρ_γ. For spherical precipitates $V(R) = 4\pi R^3/3$ is the particle volume and $F(Q,R) = 3[\sin(QR) - (QR)\cos(QR)]/(QR)^3$ the form factor. $D_V(R)dR$ represents the volume fraction of precipitates with a radius between R and $R+dR$ for a particle volume distribution $D_V(R)$. The frequently used particle number distribution $D_N(V)$, where $D_N(V)dR$ represents the number of particles per unit volume with a radius between R and $R+dR$, is directly related to the particle volume distribution by $D_N(V) = D_V(R)/V(R)$.

The neutron scattering length density of austenite is determined by $\rho_\gamma = N_o^\gamma b_c^{Fe} = 8.02\times10^{14}$ m^{-2}, where N_o^γ is the number density of iron atoms in austenite and b_c^{Fe} is the coherent

114

neutron scattering length of iron. For NbC and MnS precipitates the neutron scattering length density is estimated at $\rho_{NbC} = N_o^{NbC} (b_c^{Nb} + b_c^C) = 5.11 \times 10^{14}$ m^{-2} and $\rho_{MnS} = N_o^{MnS} (b_c^{Mn} + b_c^S) = -0.22 \times 10^{14}$ m^{-2}, respectively. The contrast in scattering length density amounts to $\Delta\rho_{NbC} = 2.91 \times 10^{14}$ m^{-2} for NbC and $\Delta\rho_{MnS} = 8.24 \times 10^{14}$ m^{-2} for MnS precipitates in the austenite matrix. As can be deduced from Eq.(3), the ratio $(\Delta\rho_{NbC})^2/(\Delta\rho_{MnS})^2 = 0.125$ indicates that the sensitivity of the scattered intensity differs a factor 8 between MnS and NbC precipitates in an austenite matrix. If part of the carbon in the NbC precipitates is substituted by nitrogen the scattering length density will show only a minor modification. The scattering length density of Nb(C$_{0.8}$N$_{0.2}$) differs about 10% from that of NbC and amounts to $\rho_{Nb(C,N)} = 4.47 \times 10^{14}$ m^{-2}, resulting in a ratio of $(\Delta\rho_{Nb(C,N)})^2/(\Delta\rho_{MnS})^2 = 0.185$. The expected incoherent background scattering from the iron atoms amounts to $(d\Sigma/d\Omega)_i(Q) = N_o^{\gamma}\sigma_i^{Fe}/4\pi = 2.6 \times 10^{-3}$ cm^{-1}sr^{-1}, where σ_i^{Fe} is the incoherent scattering cross section of iron.

The particle volume distribution $D_V(R)$ of the precipitates was fitted to the macroscopic differential scattering cross-section $(d\Sigma/d\Omega)(Q)$ with the GNOM regularisation programme [14-15]. In the fits we have assumed that the precipitates are spherical, which is supported by transmission electron microscopy measurements on both Nb(C,N) [4-8] and MnS [16] precipitates. Due to the limited Q range with $Q_{min} = 0.09$ nm^{-1} we have restricted the particle radius of the fitted effective particle volume distribution to a maximum value of $R_{max} = \pi/Q_{min} = 33$ nm and allowed for a finite particle volume distribution at R_{max}. No reliable information can be obtained for larger particles from the experimental data. In the presence of precipitates with $R > R_{max}$ this assumption can however introduce a significant uncertainty in the particle volume distribution for the larger particles (close to R_{max}). In order to obtain a quantitative estimate of the particle volume distribution we used the contrast in scattering length density $\Delta\rho$ between austenite and MnS in Eq. (3). The effective particle volume distribution

$$D_V(R) = D_V^{MnS}(R) + \left(\frac{\Delta\rho_{Nb(C,N)}}{\Delta\rho_{MnS}}\right)^2 D_V^{Nb(C,N)}(R), \qquad (7.4)$$

therefore also contains the scaled distribution of the Nb(C,N) precipitates $D_V^{Nb(C,N)}(R)$.

7.3. Results

In Fig. 7.2 the thermal treatment applied to samples Nb0, Nb5, and Nb10 is shown schematically. At the start of the experiment the sample is heated from room temperature to the lower limit of the single-phase austenite region at 910 °C. In order to examine the thermal stability of the precipitates as a function of temperature, the temperature is raised each 30 min in steps of 25 °C until the maximum temperature of 1200 °C is reached. After two hours at 1200 °C the temperature is lowered each hour in steps of 50 °C until the lowest temperature of 910 °C is reached. Finally, we examined the effect of quenching the sample from the austenite to the ferrite phase and a subsequent annealing on the formation of Nb(C,N) precipitates. The samples were reheated to 1200 °C (30 min) to dissolve the Nb(C,N) precipitates, subsequently quenched to 500 °C (30 min) to bring the niobium and carbon in supersaturated solution, and finally reheated to 910 °C (30 min).
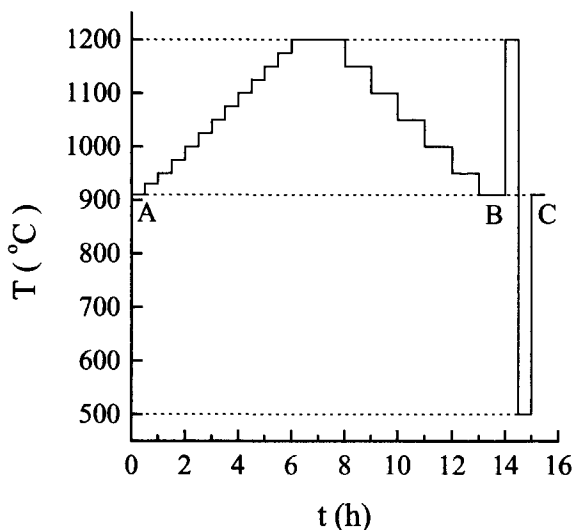
Fig. 7.2: Schematic picture of the temperature profile used for the small-angle neutron scattering experiments at high temperatures. The state at T = 910 °C is indicated by A, B, and C depending on its thermal history of heating (A), cooling (B), or quenching (C).

All isothermal measurements were divided into separate blocks of 10 min in order to study the formation or dissolution kinetics of the precipitates.

In Fig. 7.3 the macroscopic differential scattering cross-section $(d\Sigma/d\Omega)(Q)$ of samples Nb0, Nb5, and Nb10 is shown as a function of the wave vector transfer Q at increasing temperatures. For increasing temperatures the scattered intensity continuously decreases during heating, while the Q dependence of $(d\Sigma/d\Omega)(Q)$ seems to be hardly affected by the change in temperature. A comparison between the data collected in the first 10 min and the following 20 min did not show a significant difference, indicating that the transformation kinetics is relatively fast compared to the 10 min of the individual measurement runs.

In Fig. 7.4 $(d\Sigma/d\Omega)(Q)$ at $Q = 0.11$ nm^{-1} is shown as a function of increasing temperature. The scattered intensity of samples Nb5 and Nb10 is nearly identical and significantly lower than that of sample Nb0. For increasing temperatures $(d\Sigma/d\Omega)(Q = 0.11$ $nm^{-1})$ decreases nearly linearly and extrapolates to a critical temperature of about 1250 °C for all three samples.

The effect of cooling on the macroscopic differential scattering cross-section $(d\Sigma/d\Omega)(Q)$ of samples Nb0, Nb5, and Nb10 is shown in Fig. 7.5 as a function of the wave vector transfer Q. For decreasing temperatures, a weak increase in intensity is observed. The observed intensity at a given temperature is considerably smaller during cooling (Fig. 7.5) than during heating (Fig. 7.3).
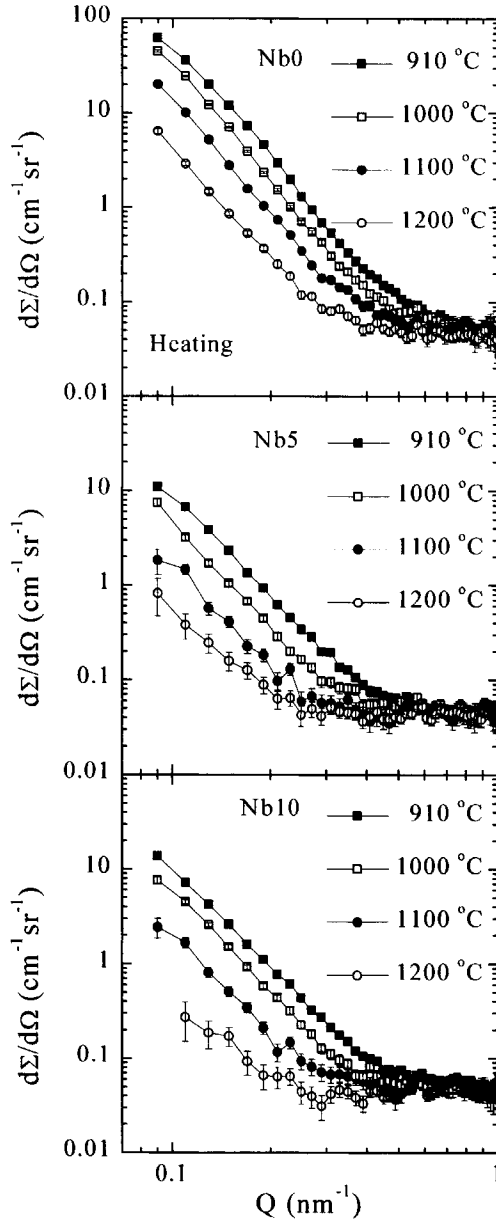
Fig. 7.3: Macroscopic differential scattering cross-section (dΣ/dΩ)(Q) of sample Nb0, Nb5, and Nb10 as a function of the wave vector transfer Q for increasing temperatures at T = 910, 1000, 1100, and 1200 °C (heating).

No significant change in the Q dependence of $(d\Sigma/d\Omega)(Q)$ or indications of a time dependence caused by the precipitation kinetics were observed during cooling.

In order to study the effect of the thermal history on the scattered intensity we have compared $(d\Sigma/d\Omega)(Q)$ at a constant temperature for different stages of the temperature profile of Fig. 7.2. In Fig. 7.6 the macroscopic differential scattering cross-section $(d\Sigma/d\Omega)(Q)$ of sample Nb0, Nb5, and Nb10 is shown as a function of wave vector transfer Q at a temperature of 910 °C for heating (A), cooling (B), and quenching (C). By quenching (C), the scattered intensity strongly increases and even exceeds the intensity in the starting condition (A) at high Q. Furthermore, the slope of $(d\Sigma/d\Omega)(Q)$ as a function of Q is modified after quenching the temperature from 1200 to 500 °C through the austenite-ferrite phase transformation. The scattered intensity in the quenched state at 910 °C showed no significant time dependence, indicating that the precipitation was completed in the annealing for 30 min at 500 °C.

In Figs. 7.7 and 7.8 the effective particle volume distribution of MnS and Nb(C,N) precipitates $D_V(R) = D_V^{MnS}(R)+(\Delta\rho_{Nb(C,N)}/\Delta\rho_{MnS})^2 D_V^{Nb(C,N)}(R)$, deduced from the scattered intensity of Figs.7.3 and 7.6, is shown as a function of the particle radius R. In Fig. 7.7, the Nb0 sample which does not contain niobium shows a single maximum in the volume distribution around $R \approx 20$ nm, while the niobium containing samples Nb5 and Nb10 show an additional peak around $R \approx 5$ nm. The peak around 5 nm increases with increasing niobium content, while the peak around 20 nm roughly scales with the sulphur content. For increasing temperature the height of both peaks decreases continuously. In Fig. 7.8, the particle volume distribution of sample Nb0, Nb5, and Nb10 are shown in state A, B, and C of Fig. 7.2. The Nb5 and Nb10 samples show a significant enhancement of small particles with a radius of $R \approx 5$ nm in the quenched state (C), which is absent in the Nb0 sample.
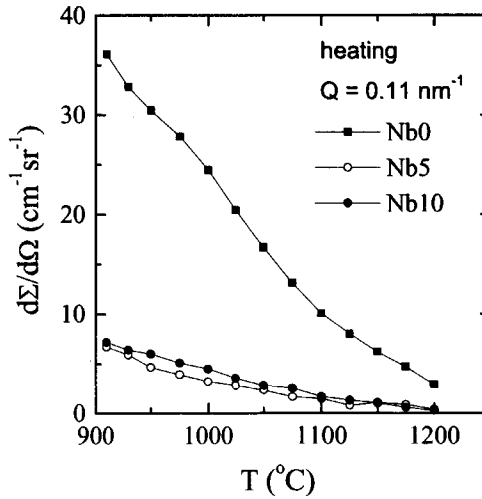

Fig. 7.4: Macroscopic differential scattering cross-section $(d\Sigma/d\Omega)(Q)$ of sample Nb0, Nb5, and Nb10 as a function of increasing temperature (heating) at a wave vector transfer of $Q = 0.11 \ nm^{-1}$.
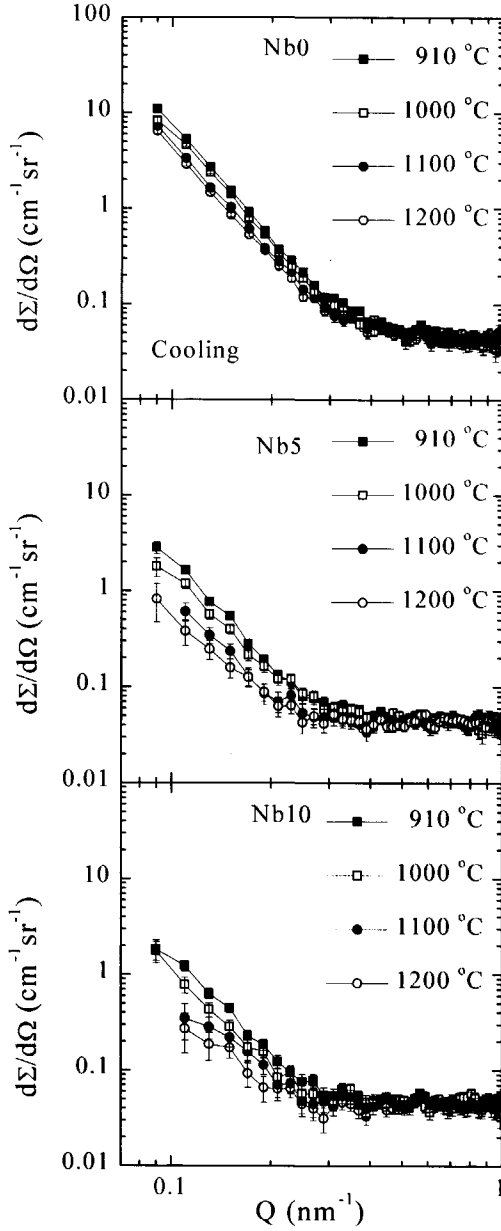
Fig. 7.5: Macroscopic differential scattering cross-section (dΣ/dΩ)(Q) of sample Nb0, Nb5, and Nb10 as a function of the wave vector transfer Q for decreasing temperatures (cooling) at T = 910, 1000, 1100, and 1200 °C.
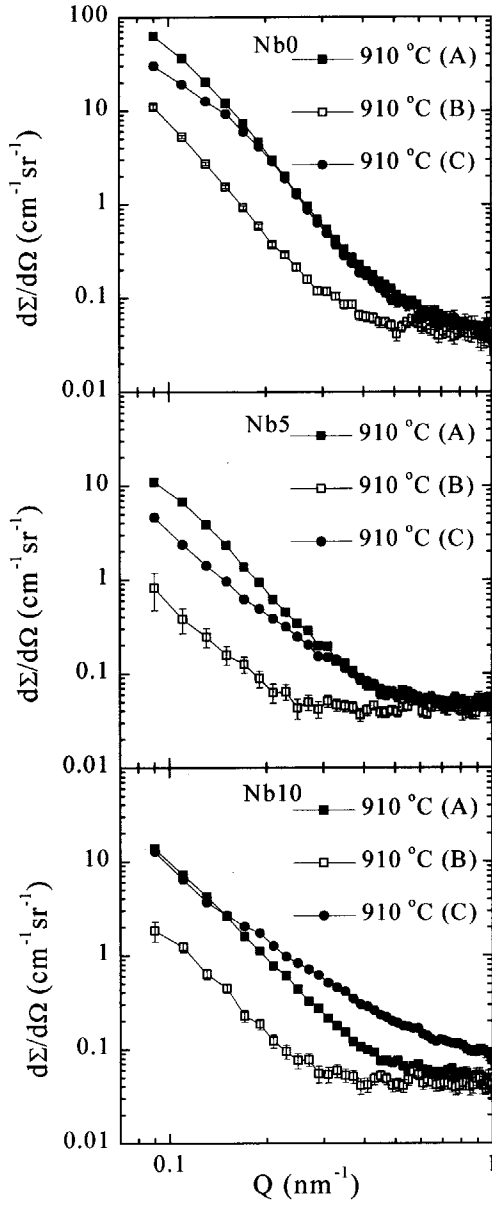
Fig. 7.6: Macroscopic differential scattering cross-section (dΣ/dΩ)(Q) of sample Nb0, Nb5, and Nb10 as a function of the wave vector transfer Q at T = 910 °C for heating (A), cooling (B), and quenching (C), as indicated in Fig. 2.
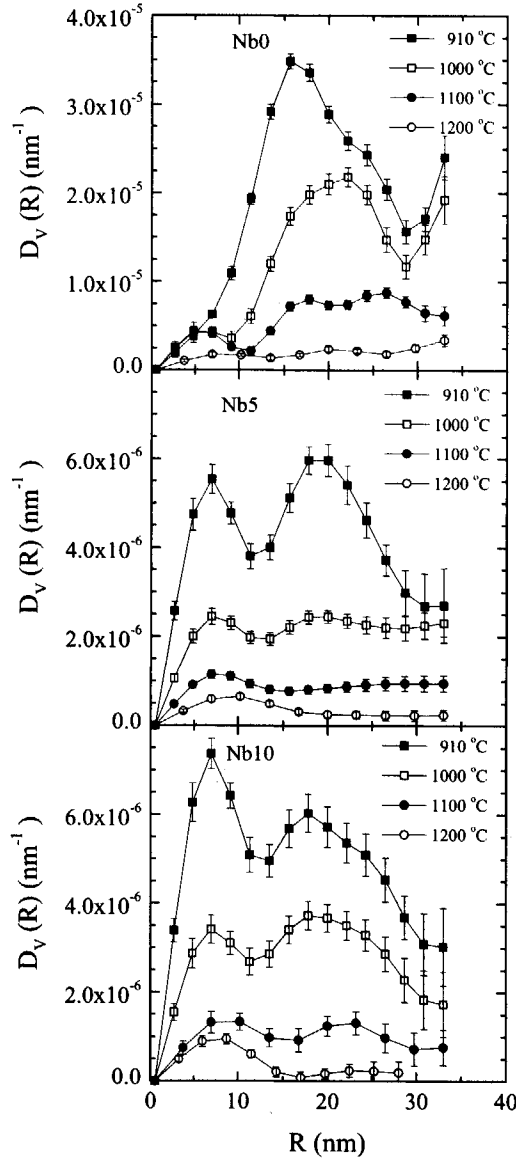
Fig. 7.7: *Effective particle volume distribution of MnS and Nb(C,N) precipitates $D_V(R)$ in sample Nb0, Nb5, and Nb10 as a function of the particle radius R for increasing temperatures (heating) at $T = 910, 1000, 1100,$ and $1200\ ^oC$. Note the differences in the vertical scale.*

121
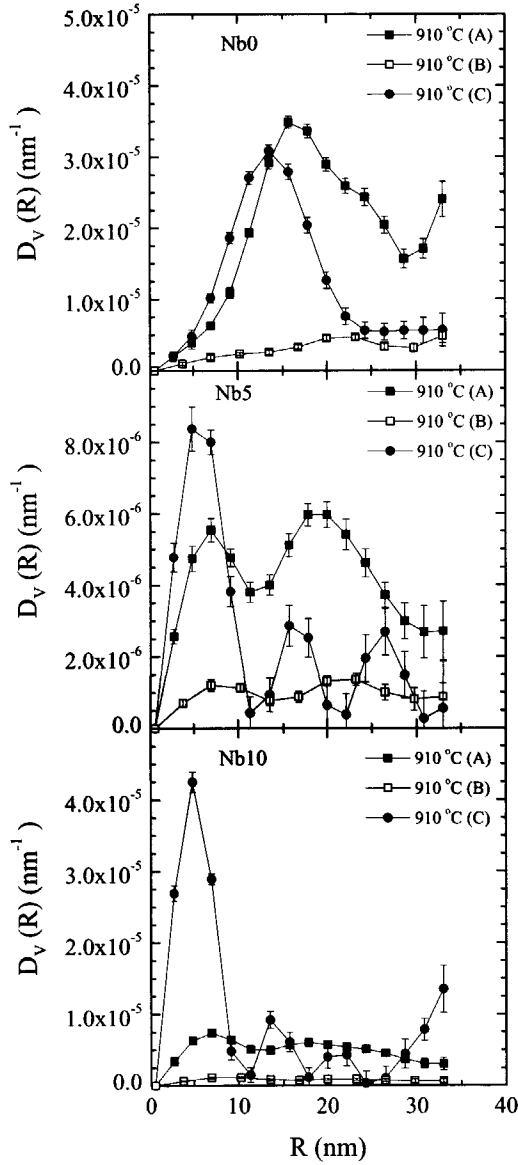
Fig. 7.8: Effective particle volume distribution of MnS and Nb(C,N) precipitates $D_V(R)$ in sample Nb0, Nb5, and Nb10 as a function of the particle radius R at T = 910 °C for heating (A), cooling (B), and quenching (C), as indicated in Fig. 2. Note the differences in the vertical scale.

7.4. Discussion

A comparison of the macroscopic differential scattering cross-section $(d\Sigma/d\Omega)(Q)$ of Figs. 7.3 and 7.4 with the composition of the HSLA steel samples Nb0, Nb5, and Nb10 indicates that the scattered intensity does not show a simple scaling with the niobium concentration. Particularly striking is that the Nb0 sample, which does not contain niobium, gives the strongest signal. As the scattered intensity at $Q = 0.11$ nm^{-1} (Fig. 7.4) roughly scales with the sulphur concentration in the steels, the main source for the observed small-angle neutron scattering in this Q range is probably the presence of a sulphide precipitate, most likely MnS.

Thermodynamical calculations on the equilibrium dissolution behaviour of the NbC and MnS precipitates were performed with the thermodynamic database MTDATA$^®$ for the steel compositions listed in Table 7.1. The results for the equilibrium fraction as a function of temperature for most stable phases NbC$_{0.877}$ and MnS are shown in Figs. 7.9 and 7.10. For the NbC$_{0.877}$ precipitates dissolution temperatures of $T_{diss} = 1249$ and 1317 °C were obtained for Nb5 and Nb10, respectively. At the maximum temperature in the SANS experiments of 1200 °C only a fraction of the Nb(C,N) precipitates is expected to dissolve. For the MnS precipitates dissolution temperatures of $T_{diss} = 1365$, 1406, and 1399 °C were obtained for Nb0, Nb5, and Nb10, respectively. In the temperature range from 910 to 1200 °C a negligible fraction of the MnS precipitates is expected to be in solution. The common extrapolated temperature of about 1250 °C, where the scattered intensity at $Q = 0.11$ nm^{-1} vanishes in Fig. 7.4, is much lower than the MnS dissolution temperatures obtained by MTDATA$^®$. It therefore probably reflects the characteristic temperature where all of the smaller MnS precipitates with a radius of $R < 50$ nm, probed by our SANS measurements, are dissolved due to the coarsening process. It is interesting to note that a frequently used simplified thermodynamical model [17,18], which only considers the solubility of Mn and S but does not account for the effect of additional alloying elements, predicts considerably lower dissolution temperatures for the MnS precipitates of $T_{diss} = 1326$, 1142, and 1138 °C for Nb0, Nb5, and Nb10, respectively.

In Fig. 7.7 the particle volume distribution $D_V(R)$ is shown for the measurements at increasing temperatures presented in Fig. 7.3. At the starting temperature of 910 °C the particle volume distribution $D_V(R)$ shows a single maximum for the Nb0 sample, and a double peak for the Nb5 and Nb10 samples. The additional peak in the particle distribution of the Nb containing samples around 5 nm increases in size for larger Nb concentrations. This strongly suggests that most of the scattering from particles with a size below 10 nm is caused by Nb(C,N) precipitates, while the scattering from larger particles is due to the presence of a sulphide, most likely MnS. With increasing temperatures $D_V(R)$ gradually decreases, both for the relatively small ($R < 10$ nm) and the relatively large ($R > 10$ nm) particles. The thermodynamic calculations on NbC$_{0.877}$ (Fig. 7.9) and MnS (Fig. 7.10) suggest that the Nb(C,N) precipitates partly dissolve into the austenite matrix while the MnS precipitates mainly coarsen to larger particles. The Nb0 sample shows a clear trend of forming larger precipitates for annealing at increasing temperatures, while the Nb5 and Nb10 samples show a change in relative intensity of the two peaks but no clear change in peak position. As shown in Fig. 7.4, the scattered intensity at $Q = 0.11$ nm^{-1} decreases nearly linearly for all three samples and extrapolates to a critical temperature of about 1250 °C, where all of the sulphide precipitates are expected to be coarsened to relatively large precipitates ($R > 50$ nm). Most of the scattered intensity of these large precipitates can, however, not be separated from the unscattered neutron beam and is therefore not monitored in the present SANS experiments. At the maximum applied temperature of 1200 °C a finite concentration of smaller precipitates remains.
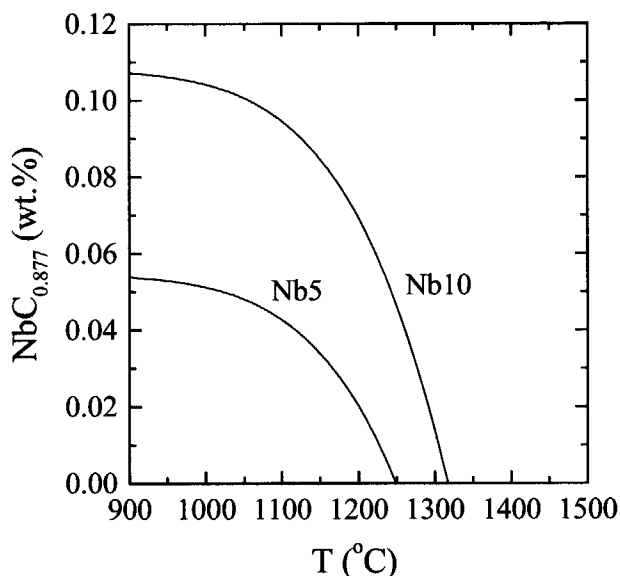
Fig. 7.9: Equilibrium NbC$_{0.877}$ phase fraction as a function for temperature for the Nb5 and Nb10 samples calculated with the thermodynamic database MTDATA®.

The coarsening of MnS precipitates for increasing temperatures up to 1200 °C, which leads to a strong reduction in the concentration of precipitates with $R < 50$ nm, is in good agreement with TEM measurements [16].

During the subsequent cooling from 1200 to 910 °C (Fig. 7.5) the scattered intensity only shows a weak increase with decreasing temperature. As the austenite is in an undeformed state, a relatively small number of nucleation sites for the formation of precipitates is expected to be available. As a consequence, most of the increase in volume fraction of MnS (and Nb(C,N)) precipitates during cooling is expected to occur through a growth of the existing relatively large ($R > 50$ nm) particles, which are not visible in the Q range of the present experiment, rather than through the formation of new small particles.

The effect of supersaturation of Nb(C,N) has been measured by heating the sample to 1200 °C, quenching to 500 °C, and finally reheating to 910 °C, as indicated in Fig. 7.6. In Fig. 7.8 the corresponding particle volume distribution $D_V(R)$ is shown (C). For the Nb0 sample the particle distribution of the quenched state (C) closely resembles that of the starting condition (A). For the Nb5 and Nb10 samples the concentration of small precipitates shows a significant enhancement in the quenched state (C) with respect to the starting condition (A). This enhancement in the concentration of small precipitates with a radius of about 5 nm becomes more pronounced with increasing niobium concentration. This suggests that the formation of Nb(C,N) precipitates is strongly enhanced by rapid cooling through the austenite to ferrite phase transformation and reheating to the austenite phase.
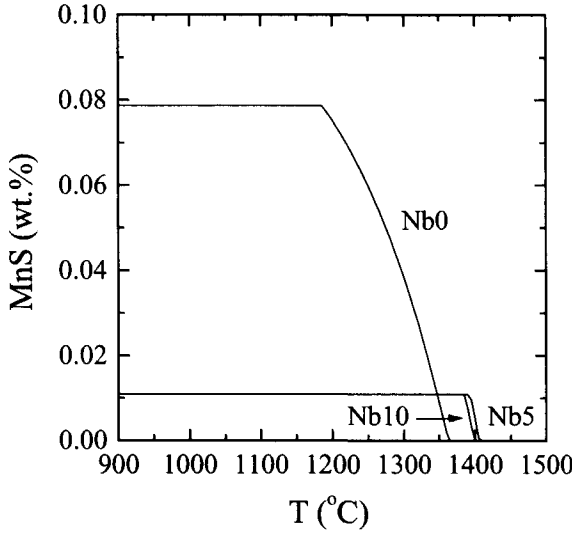
Fig. 7.10: Equilibrium MnS phase fraction as a function for temperature for the Nb0, Nb5 and Nb10 samples calculated with the thermodynamic database MTDATA®.

The supersaturation of niobium caused by the large undercooling after quenching from the austenite to the ferrite phase is expected to introduce a large concentration of new nucleation sites for Nb(C,N) precipitates. For the sample without niobium no significant change in the concentration of small particles ($R < 10$ nm) is observed. Quenching of the Nb0 sample through the austenite to ferrite phase transformation and reheating to the austenite phase promotes the formation of MnS precipitates with a radius of $R < 50$ nm in comparison with slow cooling (B). It does however not lead to an additional peak in particle volume distribution around 5 nm.

The absence of a significant time dependence of the scattered intensity of the 10 min runs during all of the experiments indicates a relatively fast precipitation and coarsening process. This is confirmed by TEM measurements on (Ti,Nb)(C,N) [4] and thermodynamic calculations on MnS [18], which indicate that the precipitation processs of both types of precipitates occurs within 1 min for the particle sizes of interest in our SANS experiments.

From the effective particle volume distribution of Figs. 7.7 and 7.8 the volume fractions of the precipitates can be evaluated. For small concentrations of MnS and Nb(C,N) precipitates the integrated effective particle volume distribution of Eq. (4) corresponds to

$$\int_0^{R\,max} D_V(R)dR = f_{MnS}(R < R_{max}) + (\Delta\rho_{Nb(C,N)}/\Delta\rho_{MnS})^2 f_{Nb(C,N)}(R < R_{max}), \quad (7.5)$$

where $f_{MnS}(R < R_{max})$ and $f_{Nb(C,N)}(R < R_{max})$ are the volume fraction of MnS and Nb(C,N) precipitates with a radius smaller than R_{max}, respectively. In Table 7.2 the integrated effective particle volume distribution is shown for the calculated volume distributions of Fig. 7.8. The

125

integrated effective particle volume distribution for sample Nb0, Nb5, and Nb10 at T = 910 °C after heating (A), cooling (B), and quenching (C) is listed for R_{max} = 33 nm and R_{max} = 10 nm. It is important to note that due to the limited experimental Q range a significant uncertainty can be present at the higher end of the particle volume distribution and therefore in the integration up to R_{max} = 33 nm. This uncertainty is however expected to negligible for the particle volume distribution of the smaller particles, represented by the integration up to R_{max} = 10 nm in Table 7.2. For the Nb0 sample without niobium the volume fraction of MnS precipitates with a radius R < 33 nm is significantly smaller than the maximum volume fraction of 0.00156. The maximum volume fraction of MnS precipitates is estimated from the sulphur concentration of Table 7.1. During cooling (B) the concentration of MnS precipitates with R < 33 nm is strongly reduced with respect to the starting material during heating (A). This can be caused by a coarsening process of the MnS precipitates during heating to T = 1200 °C. Subsequent quenching (C) from 1200 °C again increases the volume fraction of smaller MnS precipitates, although it does not reach the value observed after heating the starting material to T = 910 °C (A). This is probably because not all of the coarsened MnS precipitates dissolve in the matrix at the maximum temperature of T = 1200 °C. As most of the scattering is caused by the MnS precipitates similar trends are observed for the integrated effective volume distribution up to R_{max} = 33 nm of the Nb5 and Nb10 samples. For the Nb5 and Nb10 sample the maximum volume fraction of MnS precipitates is estimated at 0.00022 when all of the sulphur forms precipitates. The maximum volume fraction of Nb(C,N) precipitates when all of the niobium forms precipitates is 0.00055 and 0.00110 for the Nb5 and Nb10 samples, respectively. The mass fractions of MnS and Nb(C,N) precipitates can be transformed into volume fractions by taking into account the density of MnS (3.99 g/cm^3) and NbC (7.86 g/cm^3) with respect to HSLA steel (7.84 g/cm^3).

Table 7.2: The integrated effective particle volume distribution $\int_0^{R\,max} D_V(R)dR$ for sample Nb0, Nb5, and Nb10 at T = 910 °C after heating (A), cooling (B), and quenching (C). The integrated effective particle volume distribution corresponds to $\int_0^{R\,max} D_V(R)dR = f_{MnS}(R < R_{max})$ + $(\Delta\rho_{Nb(C,N)} / \Delta\rho_{MnS})^2 f_{Nb(C,N)}(R < R_{max})$, where $f_{MnS}(R < R_{max})$ and $f_{Nb(C,N)}(R < R_{max})$ correspond to the volume fraction of MnS and Nb(C,N) precipitates with a radius smaller than R_{max}, respectively.

| | R_{max} = 33 nm / 10 nm | | |
	Heating (A)	Cooling (B)	Quenching (C)
Nb0	0.00061 / 0.00007	0.00009 / 0.00001	0.00040 / 0.00010
Nb5	0.00014 / 0.00004	0.00003 / 0.00001	0.00009 / 0.00005
Nb10	0.00016 / 0.00006	0.00003 / 0.00001	0.00032 / 0.00023

Because TEM measurements [4-8] indicate that the Nb(C,N) particle sizes are limited to $R <$ 10 nm, we can use the integrated effective particle volume distribution up to $R_{max} = 10$ nm from Table 7.2 to estimate the volume fraction of Nb(C,N) precipitates quantitatively. In order to do this the calculated volume fraction of small MnS precipitates $f_{MnS}(R < 10$ nm) for the Nb0 sample is subtracted from the niobium containing samples after scaling with the sulphur concentration in the samples. When the reduced sensitivity of the effective particle volume distribution to the Nb(C,N) precipitates is taken into account, the volume fraction of Nb(C,N) precipitates is obtained, as listed in Table 7.3. The estimated volume fractions are generally significantly smaller than the maximum volume fraction when all the niobium forms precipitates. During heating (A) about half of the maximum volume fraction is observed for the Nb5 and Nb10 samples at $T = 910$ °C. During cooling (B) most of the niobium is still dissolved in the matrix, while quenching (C) causes a significant increase in the Nb(C,N) volume fraction with respect to the starting material during heating (A). For the Nb10 sample even a volume fraction is found which is larger than the maximum value when all of the niobium is precipitated. This may indicate that the formation of Nb(C,N) precipitates enhances the formation of small MnS precipitates with $R < 10$ nm.

Table 7.3: Estimated volume fraction of Nb(C,N) precipitates at $T = 910$ °C for sample Nb5 and Nb10 deduced from the effective particle volume distribution integrated up to $R_{max} = 10$ nm (Table 7.2). The maximum volume fraction of Nb(C,N) precipitates is 0.00055 and 0.00110 for the Nb5 and Nb10 sample, respectively.

	Heating (A)	Cooling (B)	Quenching (C)
Nb5	0.00026	0.00005	0.00033
Nb10	0.00037	0.00005	0.00169

7.5. Conclusions

We have studied the volume distribution of precipitates in silicon-killed HSLA steels by small-angle neutron scattering at high temperatures. Three hot-rolled samples with different niobium concentrations were studied. For slow heating from a temperature of 910 to 1200 °C the scattered intensity strongly decreases. A comparison of the particle volume distribution of the 3 different samples reveals that the samples containing niobium have an additional peak around 5 nm, which increases in size with the niobium concentration. This strongly suggests that most of the scattering from particles with a size below 10 nm is caused by Nb(C,N) precipitates, while the scattering from larger particles is expected to be caused by MnS precipitates. This is supported by a comparison of the maximum in the particle volume distribution around 20 nm for the 3 different samples, which shows that the intensity of this maximum mainly scales with the sulphur rather than the niobium content, indicating that the scattering from particles with a radius of $R \approx 20$ nm is predominantly caused by a sulphide, probably MnS, rather than Nb(C,N). Thermodynamic calculations suggest that the Nb(C,N) precipitates gradually dissolve, while the MnS precipitates do not dissolve but coarsen when the temperature increases from 910 to 1200 °C. During subsequent cooling from 1200 to 910 °C the scattered intensity shows a weak increase as the existing precipitates are expected to

127

grow in the absence of a significant concentration of new nucleation sites without deformation. The particle distribution obtained after quenching from the austenite to the ferrite phase and reheating to the austenite phase strongly enhances the presence of small precipitates of about 5 nm, suggesting that a large concentration of Nb(C,N) precipitates is formed.

Acknowledgements

References

[1] G. Li, T.M. Maccagno, D.Q. Bai, J.J. Jonas, ISIJ International 36 (1996) 1479.

[2] J. Perttula, P. Kantanen, P. Karjalainen, Scand. J. of Metallurgy 27 (1998) 128.

[3] H.L. Andrade, M.G. Akben, J.J. Jonas, Metallurgical Transactions A, 14A (1983) 1967.

[4] Heilong Zou and J.S. Kirkaldy, Metallurgical Transactions A, 22A (1991) 1511.

[5] R.C. Cochrane and W.B. Morrison, Proceedings *Steels for line pipe and pipeline fittings* Conference, The Metal Society, 21-23 October 1981, London, p. 70.

[6] S. Akamatsu, T. Senuma, and M. Hasebe, ISIJ 32 (1992) 275.

[7] R. Abad, B. López, and I Gutierrez, Materials Science Forum 284-286 (1998) 167.

[8] V. Thillou, M. Hua, C.I. Garcia, C. Perdrix, and A.J. DeArdo , *Materials Science Forum* 284-286 (1998) 311.

[9] A.D. Sequeira, J.S. Pedersen, and G. Kostorz, in *Modern Aspects of Small-Angle Scattering*, Edited by H. Brumberger, Kluwer Academic Press, (1995), p. 267.

[10] A.J. Allen, D. Gavillet, and J.R. Weertman, Acta Metall. Mater. 41 (1993) 1869.

[11] R. Coppola, R. Kampmann, M. Magnani, and P. Staron, Acta Mater. 46 (1998) 5447.

[12] R.K. Heenan, J. Penfold, and S.M. King, J. Appl. Cryst. 30 (1997) 1140.

[13] S.M. King, in *Modern Techniques for Polymer Characterisation*, Edited by R.A. Pethrick and J.V. Dawkins, John Wiley & Sons, (1999), p. 171.

[14] D.I. Svergun, J. Appl. Cryst. 25 (1992) 495.

[15] http://www.embl-hamburg.de/ExternalInfo/Research/Sax/gnom.html.

[16] T. Hayashida, S. Sanagi, and T. Kawano, ISS 33rd Mechanical Working and Steel Processing Conference held in October 1991, Ironmaking & Steelmaking (1992) 33.

[17] E.T. Turkdogan and J. Pearson, J. Iron and Steel Inst. 177 (1955) 349; E.T. Turkdogan, S. Ignotowicz, and J. Pearson, J. Iron and Steel Inst. 180 (1955) 349.

[18] R.A. Hubert and C. Standaert, Proceedings THERMEC'97 International Conference on Thermo-Mechanical Processing of Steels and Other Materials, Eds. T. Chandra and T. Sakai, The Minerals, Metals and Materials Society (1997) p. 459.

Evolving Microstructures in Carbon Steel

A Neutron and Synchrotron Radiation Study

S.E. Offerman

Summary

The work presented in this thesis aims to provide in-situ experimental observations, obtained with neutron and synchrotron techniques, on the decomposition of austenite into ferrite and pearlite in carbon steel and to relate these observations to physical models that describe the phase transformation kinetics as grain nucleation and growth processes. This thesis describes unique neutron and synchrotron experiments that give in-situ information on the dynamic behavior of grains inside carbon steel during solid-state phase transformations, even down to the level of individual grains.

Chapter 1 presents the background and relevance of the research presented in this thesis. The mechanical properties of polycrystalline materials like steel are largely determined by the phase transformation kinetics during the production process. A detailed knowledge of the evolution of the microstructure as a function of the process parameters is essential for the production of materials with strictly specified demands concerning strength and formability. The current phase transformation models for industrial conditions are often empirical or semi-empirical in nature. These models can not be used to predict the phase transformation kinetics during new processing routes or to develop new materials. Experimental observations that give more detailed information about the evolution of the microstructure during phase transformations are crucial for the development of physical phase transformation models.

Chapter 2 gives a brief overview of the nucleation and growth theories on which the current diffusion-controlled solid-state phase transformation models are based. Firstly, the classical nucleation theory (CNT) is described. Secondly, the theory of Zener that describes the growth of a pro-eutectoid phase like ferrite is presented. Thirdly, the theories of Zener-Hillert and Hillert that describe the growth of an eutectoid phase like pearlite is described. Finally, the most important results of the theory developed by Kolmogorov, Johnson, Mehl, and Avrami (KJMA) that predicts the overall transformation rate are reviewed.

Chapter 3 describes the in-situ neutron and synchrotron techniques that are used for this thesis, which are three-dimensional neutron depolarization (3DND), three-dimensional x-ray microscopy (3DXRD) and small-angle neutron scattering (SANS). The 3DND technique simultaneously probes the ferrite fraction, the mean magnetic particle size, and the spatial distribution of the forming ferromagnetic phase in the paramagnetic austenite matrix during the transformation. The 3DXRD technique allows the in-situ study of *individual* grains during the phase transformations in steel: Nucleation and growth behavior of individual pro-eutectoid or pearlitic ferrite grains, and the carbon enrichment of individual austenite grains. SANS can be used to determine particle size distributions of precipitates that are embedded in the microstructure.

Chapter 4 describes the influence of micro-segregation of Mn, Si, and Cr on the austenite decomposition into ferrite/pearlite bands during isothermal transformations in hot-rolled medium-carbon steel, which has been studied by Neutron Depolarization, Electron Probe Micro Analysis (EPMA), and optical microscopy. Two-dimensional EPMA-scans across several ferrite/pearlite bands show that microstructural banding in hot-rolled medium-carbon steel is related to the microchemical segregation of manganese and silicon. The presence of microchemical bands results in a spatial variation of the austenite/ferrite transition temperature. Therefore, the local driving force for ferrite nucleation is higher in regions with a high austenite/ferrite transition temperature than in regions with a low austenite/ferrite transition temperature. The experiments show that the degree of banding is low for low isothermal transformation temperature, since the relative difference between the ferrite nucleation rates in regions with low and high austenite/ferrite transition temperatures is small in that case. Stronger band formation is found at lower undercoolings. It is shown that the presence of microchemical bands is a prerequisite for band formation, but the kinetics of the phase transformation determines the actual existence of microstructural bands. A quantitative model based on nucleation and growth criteria has been developed, with which the formation of microstructural bands can be predicted.

Chapter 5 describes neutron depolarization measurements on the isothermal decomposition of austenite into ferrite and pearlite, as well as improvements on the interpretation of 3DND measurements. 3DND measurements on the isothermal austenite/ferrite phase transformation in a medium carbon steel (C45) were performed. In a subsequent study on the isothermal austenite/pearlite transformation in nearly eutectoid steel a comparison was made between dilatometry and 3DND measurements. This study showed that the reduced magnetization changes during the transformation corresponding to the evolution of the magnetic structure from isolated pearlite colonies, via a transition region, to an interconnecting network. From additional optical microscopy measurements and magnetic calculations, it was found that the measured magnetic domain size in pearlitic steel corresponds to the average distance over which the ferrite plates within a pearlite colony are more or less parallel. It was shown that the average particle size and the degree of clustering of pearlite colonies can be determined separately from the measured depolarization. These improvements on the interpretation of 3DND measurements allows a more detailed analysis of the isothermal austenite/pearlite transformation in nearly eutectoid steel. The pearlite fraction, the average pearlite colony size, and the spatial distribution of the pearlite colonies were simultaneous determined. From these measured parameters nucleation and growth rates were determined.

The in-situ measurements show that the pearlite nucleation is a transient nucleation process in which the nucleation rate increases linearly with time, which can be described approximately by the classical nucleation theory. The rate controlling mechanism for the nucleation of pearlite in hypo-eutectoid steels is the nucleation of cementite (see chapter 6). The effect of interfacial energies on the activation energy for cementite nucleation during the pearlite formation is found to be approximately 10^5 times higher than for the nucleation of pro-eutectoid ferrite. The main difference between the nucleation of pro-eutectoid ferrite and pearlitic cementite is probably that the former takes place at high-energy grain boundaries, while the latter takes place at low-energy interfaces. Therefore, the nucleation of pro-eutectoid ferrite is relatively easy compared to the nucleation of pearlitic cementite.

There is a controversy in literature on how to describe the pearlite growth kinetics. The Zener-Hillert law assumes that volume diffusion of carbon atoms is the rate controlling mechanism for pearlite growth, while the Hillert law assumes that grain boundary diffusion of carbon atoms is the rate controlling mechanism for pearlite growth. The 3DND

130

measurements show that relatively close to the austenite/pearlite transition temperature, the average pearlite growth rate corresponds to the theoretical prediction on the basis of volume diffusion of carbon atoms.

Chapter 6 describes three-dimensional x-ray diffraction microscopy measurements on the decomposition of austenite into ferrite and pearlite during continuous cooling of medium carbon steel. The in-situ measurements give information about the behavior of individual grains of pro-eutectoid ferrite, pearlitic ferrite and austenite during the transformation. By using a beam of focussed hard x-rays (80 keV) with dimensions of 100×100 μm^2, the diffraction patterns that were recorded during the transformation were composed of individual diffraction spots corresponding to individual grains in the steel specimen.

By counting the number of diffraction spots, the number of ferrite grains (with a grain radius above the detection limit of about 2 μm) is obtained as a function of temperature. The number of ferrite nuclei increases most rapidly just below the austenite/ferrite transition temperature, but new ferrite nuclei are continuously formed over a large temperature range until the austenite/pearlite transformation starts. Only a very small number of new pearlitic ferrite nuclei are formed at the pearlite transition temperature range. The normalized experimental nucleation rate is compared to the CNT. The shape of the theoretical curve is in qualitative agreement with the measurements. The most striking difference is, however, that the maximum nucleation rate occurs at a higher temperature than predicted by the CNT. The measurements show that the activation energy for grain nucleation is at least two orders of magnitude smaller than that predicted by thermodynamic models applied to the CNT. The low experimental value for the activation energy for nucleation indicates a close balance between the energy that is released by the removal of incoherent austenite/austenite grain boundaries and the energy that is required for the formation of coherent and incoherent austenite/ferrite grain boundaries.

The growth behavior of an individual grain was determined from the intensity of the corresponding diffraction spot, which is proportional to the volume of the grain. Four types of ferrite growth could be distinguished. Firstly, the observed growth curves of the newly formed grains confirm the parabolic growth model of Zener, but growth curves of other grains show three fundamentally different types of growth. The second type of ferrite growth is related to ferrite grains that continue to grow with the same crystallographic orientation during the pearlite formation as part of a pearlite colony. The third type is related to retarded ferrite nucleation and growth. An enrichment of carbon in the austenite causes a local decrease in transition temperature, which leads to a retarded nucleation. The retarded growth is caused by an indirect interaction with growing neighboring grains. The neighboring grains do not directly touch each other, but interfere via surrounding diffusion and stress fields. The last class of ferrite grain growth is characterized by a complex growth behavior. In this least frequently observed growth mode, ferrite grains not only grow, but also temporarily shrink upon continued transformation. This behavior is attributed to a complex grain-boundary migration caused by a direct interaction with neighboring grains. The neighboring grains directly touch, but their grain boundaries are not yet in their equilibrium position. It is known that some grain boundaries are more stable than others depending on the curvature. As the growth is a dynamic process, the forces on the grain boundaries may change irregularly resulting in the observed growth behavior.

Chapter 7 describes SANS measurements of the size distributions of Nb(C,N) and MnS precipitates as a function of temperature during dissolution or precipitation in high strength low alloy (HSLA) steel. Nb(C,N) precipitates have an important influence on the

decomposition of austenite into ferrite, because Nb(C,N) precipitates can act as pinning centers that retard the austenite recrystallization process. This results in a smaller average austenite grain size and thereby in an enhanced number of potential nucleation sites for ferrite. The volume distribution of precipitates in silicon-killed HSLA steel is studied by small-angle neutron scattering at high temperatures. Three hot-rolled samples with different niobium concentrations were studied. For slow heating from a temperature of 910 to 1200°C the scattered intensity strongly decreases. Thermodynamic calculations suggest that the Nb(C,N) precipitates gradually dissolve, while the MnS precipitates do not dissolve but coarsen when the temperature increases from 910 to 1200°C. During subsequent cooling from 1200 to 910°C the scattered intensity shows a weak increase as the existing precipitates are expected to grow in the absence of a significant concentration of new nucleation sites in this undeformed material. The particle distribution obtained after quenching from the austenite to the ferrite phase and reheating to the austenite phase strongly enhances the presence of small precipitates of about 5 nm, suggesting that a large concentration of Nb(C,N) precipitates is formed.

Evoluerende Microstructuren in Koolstofstaal

Een onderzoek met neutronen en synchrotronstraling

S.E. Offerman

Samenvatting

Het doel van dit proefschrift is om de decompositie van austeniet in ferriet en perliet in koolstofstaal experimenteel waar te nemen met behulp van in situ neutronen- en synchrotrontechnieken en om deze waarnemingen te relateren aan fysische modellen die de kinetiek van fasetransformaties beschrijft als nucleatie- en groeiprocessen van korrels (kristallen). Dit proefschrift beschrijft unieke neutronen- en synchrotronexperimenten die in situ informatie geven over het dynamische gedrag van korrels in koolstofstaal tijdens transformaties, zelfs tot op het niveau van individuele korrels.

In hoofdstuk 1 wordt de achtergrond en relevantie van dit onderzoek beschreven. De mechanische eigenschappen van polykristallijne materialen zoals staal worden grotendeels bepaald door de kinetiek van fasetransformaties tijdens het productieproces. Een gedetailleerde kennis van de evolutie van de microstructuur als functie van de procesparameters is essentieel voor de productie van materialen met strikte specificaties met betrekking tot de sterkte en vervormbaarheid. De huidige modellen van fasetransformaties voor industrieel gebruik zijn vaak empirisch of semi-empirisch. Deze modellen kunnen niet gebruikt worden om de kinetiek van fasetransformaties te voorspellen voor nieuwe productieroutes of voor de ontwikkeling van nieuwe materialen. Experimentele waarnemingen die meer gedetailleerde informatie geven over de evolutie van de microstructuur tijdens fasetransformaties zijn cruciaal voor de ontwikkeling van fysische modellen van fasetransformaties.

In hoofdstuk 2 wordt een bondig overzicht gegeven van de nucleatie- en groeitheorieën die de basis vormen voor de huidige fysische modellen die fasetransformaties in vaste stoffen beschrijven die door diffusie worden gedomineerd. Ten eerste wordt de klassieke nucleatie theorie (CNT) beschreven. Ten tweede wordt de Zener theorie gepresenteerd die de groei van een pro-eutectoïdische fase als ferriet beschrijft. Ten derde worden de Zener-Hillert en Hillert theorieën behandeld die de groei van een eutectoïdische fase als perliet beschrijven. Tenslotte worden de belangrijkste resultaten besproken van de theorie die is ontwikkeld door Kolmogorov, Johnson, Mehl en Avrami (KJMA). Deze theorie voorspelt het totale verloop van de transformatie.

Hoofdstuk 3 beschrijft de in situ neutronen- en synchrotrontechnieken die voor dit proefschrift zijn gebruikt: driedimensionale neutronendepolarisatie (3DND), driedimensionale Röntgenmicroscopie (3DXRD) en kleine-hoek neutronenverstrooiing (SANS). De 3DND-techniek geeft simultaan informatie over de fractie ferriet, de gemiddelde magnetische deeltjesgrootte en de ruimtelijke verdeling van de zich vormende ferromagnetische fase in de paramagnetische austenietmatrix. Met de 3DXRD-techniek kan het nucleatie- en groeigedrag van *individuele* pro-eutectoïdische en perlitische ferrietkorrels

en de koolstofverrijking van individuele austenietkorrels worden bestudeerd tijdens fasetransformaties. Met behulp van de SANS-techniek kan de deeltjesgroottedistributie van precipitaten die zich in de microstructuur bevinden worden bepaald.

In hoofdstuk 4 wordt de invloed van de microsegregatie van Mn, Si en Cr op de isotherme decompositie van austeniet in banden van ferriet en perliet in een warmgewalst koolstofstaal (0.36 wt.% C) bepaald met behulp van 3DND, electron probe micro analysis (EPMA) en optische microscopie. Tweedimensionale EPMA-scans over meerdere ferriet/perliet-banden laten zien dat de microstructurele bandvorming in warmgewalst koolstofstaal gerelateerd is aan de microchemische segregatie van mangaan en silicium. De aanwezigheid van microchemische banden resulteert in een ruimtelijke variatie van de overgangstemperatuur van austeniet naar ferriet. Daardoor is de lokale drijvende kracht voor nucleatie van ferriet groter in gebieden met een hoge overgangstemperatuur van austeniet naar ferriet dan in gebieden met een lage overgangstemperatuur. De experimenten tonen aan dat de mate van bandvorming klein is voor lage transformatietemperaturen, omdat het relatieve verschil in nucleatiesnelheid van ferriet kleiner wordt tussen gebieden met een lage en een hoge overgangstemperatuur. Sterkere bandvorming wordt waargenomen bij kleinere onderkoelingen. Aangetoond is dat de aanwezigheid van microchemische banden een voorwaarde is voor het ontstaan van microstructurele bandvorming, maar de kinetiek van de fasetransformaties bepaalt of er daadwerkelijk microstructurele banden ontstaan. Er is een kwantitatief model ontwikkeld dat is gebaseerd op nucleatie- en groeicriteria waarmee de vorming van microstructurele banden kan worden voorspeld.

Hoofdstuk 5 beschrijft zowel neutronendepolarisatiemetingen tijdens de isotherme decompositie van austeniet in ferriet en perliet als verbeteringen in de interpretatie van 3DND metingen. Er zijn 3DND metingen verricht gedurende de isotherme fasetransformatie van austeniet in ferriet in een koolstofstaal (0.47 wt.% C). In een studie naar de transformatie van austeniet in perliet in bijna eutectoïdisch staal is een vergelijking gemaakt tussen dilatometrie- en 3DND-metingen. Uit deze studie blijkt dat de verandering van de gereduceerde magnetisatie tijdens de transformatie overeenkomt met de evolutie van de magnetische structuur van een toestand met geïsoleerde perliet-kolonies, via een overgangsgebied, in een netwerk van onderling verbonden magnetische domeinen. Uit aanvullende metingen met de optische microscoop en magnetische berekeningen blijkt dat de gemeten magnetische domeingrootte in perlitisch staal overeenkomt met de gemiddelde afstand waarover de platen van ferriet in een perlietkolonie min of meer parallel zijn. Aangetoond wordt dat de gemiddelde deeltjesgrootte en de mate van clustering van perlietkolonies onafhankelijk van elkaar bepaald kunnen worden uit de gemeten depolarisatie. Deze verbeteringen in de interpretatie van de 3DND-metingen maken een gedetailleerdere analyse mogelijk van de isotherme transformatie van austeniet in perliet in bijna eutectoïdisch staal. De perliet-fractie, de gemiddelde koloniegrootte van perliet en de ruimtelijke verdeling van de perlietkolonies zijn simultaan gemeten. Uit deze metingen zijn nucleatie- en groeisnelheden afgeleid.

De in situ metingen laten zien dat de nucleatiesnelheid van perliet lineair toeneemt met de tijd, hetgeen in benadering beschreven kan worden door de klassieke nucleatietheorie. De snelheidsbepalende stap voor de nucleatie van perliet in hypo-eutectoïdisch staal is de nucleatie van cementiet (zie hoofdstuk 6). Het effect van de grensvlakenergieën op de activeringsenergie voor de nucleatie van cementiet tijdens de vorming van perliet blijkt ongeveer 10^5 maal groter te zijn dan voor de nucleatie van pro-eutectoïdisch ferriet. Het grote verschil tussen de nucleatie van pro-eutectoïdisch ferriet en perlitisch cementiet is waarschijnlijk dat de eerstgenoemde plaats vindt op korrelgrenzen met een hoge energie,

134

terwijl de laatstgenoemde plaats vindt op korrelgrenzen met een lage energie. Hierdoor is de nucleatie van pro-eutectoïdisch ferriet relatief eenvoudig vergeleken bij de nucleatie van perlitisch cementiet.

Een controverse in de literatuur is de beschrijving van de groei van perliet. De Zener-Hillert wet veronderstelt dat volumediffusie van koolstofatomen het snelheidsbepalende mechanisme is voor de groei van perliet, terwijl Hillert veronderstelt dat korrelgrensdiffusie van koolstofatomen het snelheidsbepalende mechanisme is voor de groei van perliet. De 3DND metingen tonen aan dat relatief dicht bij de overgangstemperatuur van austeniet naar perliet de gemiddelde groeisnelheid van perliet overeenkomt met de theoretische voorspelling op de basis van volumediffusie van koolstofatomen.

Hoofdstuk 6 beschrijft driedimensionale Röntgenmicroscopiemetingen tijdens de decompositie van austeniet in ferriet en perliet gedurende continu koelen van een koolstofstaal (0.21 wt.% C). De in situ 3DXRD metingen geven informatie over het gedrag van individuele korrels van ferriet, perlitisch ferriet en austeniet tijdens de transformatie. Door het gebruik van gefocusseerde harde röntgenstralen (80 keV) met een bundelafmeting van 100×100 μm^2, bestaan de diffractiepatronen die tijdens de transformatie zijn opgenomen uit individuele diffractiestippen die overeenkomen met de individuele korrels in het staal.

Het aantal diffractiestippen als functie van de temperatuur geeft het aantal ferrietkiemen (waarvan de straal boven de detectielimiet van 2 μm uitkomt) tijdens de transformatie. Het aantal ferrietkiemen neemt het snelst toe net onder de overgangstemperatuur van austeniet naar ferriet, maar er worden continu nieuwe ferrietkiemen gevormd over een groot temperatuurgebied totdat de transformatie van austeniet in perliet start. Slechts een klein aantal nieuwe kiemen van perlitisch ferriet worden gevormd in het overgangstemperatuur gebied van perliet. De genormaliseerde experimentele nucleatiesnelheid van perliet is vergeleken met de CNT. De vorm van de theoretische curve komt overeen met de metingen. Het meest in het oog springende verschil is echter dat de maximale nucleatiesnelheid bij een veel hogere temperatuur ligt dan voorspeld wordt door de CNT. De metingen tonen aan dat de activeringsenergie voor nucleatie van korrels twee ordes van grootte kleiner is dan wordt voorspeld door de thermodynamische modellen die toegepast worden in de CNT. De lage experimentele waarde voor de activeringsenergie voor nucleatie doet vermoeden dat er een balans is tussen de energie die vrijkomt bij het verwijderen van incoherente korrelgrenzen tussen twee austenietkorrels en de energie die benodigd is voor de vorming van coherente en incoherente grensvlakken tussen austeniet- en ferrietkorrels.

Het groeigedrag van individuele korrels is bepaald uit de intensiteit van de corresponderende diffractiespot die evenredig is met het volume van de korrel. Vier typen groei van ferriet konden worden onderscheiden. Ten eerste bevestigen de waargenomen groeicurves van de nieuw gevormde korrels het klassieke parabolische groeimodel van Zener, maar andere groeicurves tonen tevens drie fundamenteel andere typen groei aan. Het tweede type groei van ferriet is gerelateerd aan pro-eutectoïdische ferrietkorrels die met dezelfde krystallografische oriëntatie doorgroeien als deel van een perlietkolonie tijdens de vorming van perliet. Het derde type groei is gerelateerd aan vertraagde nucleatie en groei van ferriet. De verrijking van koolstof in de austeniet zorgt voor een lokale verlaging van de overgangstemperatuur, hetgeen een vertraagde nucleatie tot gevolg heeft. De vertraagde groei wordt veroorzaakt door een indirecte interactie met naburige korrels die groeien. De naburige korrels raken elkaar niet direct, maar interfereren via omliggende diffusie- en spanningsvelden. De laatste klasse van groei van ferriet wordt gekarakteriseerd door een complex groeigedrag. Tijdens deze minst frequent waargenomen groeimode groeien de korrels van ferriet niet alleen, maar ze krimpen ook tijdelijk tijdens de transformatie. Dit gedrag wordt toegeschreven aan een complexe migratie van korrelgrenzen die veroorzaakt

wordt door een directe interactie met omliggende korrels. De omliggende korrels raken elkaar, maar hun korrelgrenzen zijn nog niet in hun evenwichtspositie. Het is bekend dat sommige korrelgrenzen stabieler zijn dan anderen afhankelijk van de kromming van het grensvlak. Aangezien groei een dynamisch proces is, kunnen de krachten op de korrelgrenzen onregelmatig veranderen tijdens de transformatie, hetgeen resulteert in het waargenomen groeigedrag.

Hoofdstuk 7 beschrijft SANS metingen van de deeltjesgroottedistributie van Nb(C,N) en MnS precipitaten als functie van de temperatuur tijdens oplossing en precipitatie in high-strength low-alloy (HSLA) staal. Nb(C,N) precipitaten hebben een belangrijke invloed op de decompositie van austeniet in ferriet, omdat Nb(C,N) precipitaten de beweging van het grensvlak van austeniet kunnen vertragen tijdens het rekristallisatieproces van austeniet. Dit resulteert in een kleinere gemiddelde korrelgrootte van austeniet en daarmee een verhoogd aantal potentiële plaatsen voor de nucleatie van ferriet.

De volumedistributie van precipitaten in HSLA is bestudeerd met behulp van kleine-hoek neutronenverstrooiing bij hoge temperaturen. Drie warmgewalste preparaten met verschillende niobiumgehaltes zijn bestudeerd. Voor langzaam opwarmen van 910 naar 1200°C neemt de verstrooide intensiteit sterk af. Thermodynamische berekeningen suggereren dat de Nb(C,N) precipitaten langzaam oplossen, terwijl de MnS precipitaten niet oplossen maar vergroven wanneer de temperatuur toeneemt van 910 naar 1200°C. Tijdens aansluitend afkoelen van 1200 naar 910°C neemt de verstrooide intensiteit een klein beetje toe wanneer de bestaande precipitaten verondersteld worden te groeien in de afwezigheid van een significante concentratie aan potentiële plaatsen voor nucleatie in het ongedeformeerde metaal. De deeltjesgroottedistributie die verkregen is na het afschrikken van de austeniet-naar de ferrietfase en opnieuw opwarmen van de austenietfase versterkt de aanwezigheid van kleine precipitaten van ongeveer 5 nm aanzienlijk, hetgeen suggereert dat er een hoge concentratie aan Nb(C,N) is gevormd.

Acknowledgements

List of publications

S.E. Offerman, L.J.G.W. van Wilderen, N.H. van Dijk, J. Sietsma, M.Th. Rekveldt, and
S. van der Zwaag,
*In-situ study of pearlite nucleation and growth during isothermal austenite decomposition in
nearly eutectoid steel,*
Acta Materialia, **51** (2003) 3927-3938.

S.E. Offerman, L.J.G.W. van Wilderen, N.H. van Dijk, M.Th. Rekveldt, J. Sietsma, and
S. van der Zwaag,
*Cluster formation of pearlite colonies during the austenite/pearlite phase transformation in
eutectoid steel,*
Physica B, **335** (2003) 99-103.

S.O. Kruijver, L. Zhao, J. Sietsma, S.E. Offerman, N.H. van Dijk, E.M. Lauridsen,
L. Margulies, S. Grigull, H.F. Poulsen, and S. van der Zwaag,
In situ observations on the mechanical stability of austenite in TRIP steel,
Journal de Physique IV, **104** (2003) 499-502.

S.E. Offerman, N.H. van Dijk, J. Sietsma, S. Grigull, E.M. Lauridsen, L. Margulies,
H.F. Poulsen, M.Th. Rekveldt, and S. van der Zwaag,
Grain nucleation and growth during phase transformations,
Science, **298** (2002) 1003-1005.

S.E. Offerman, N.H. van Dijk, M.Th. Rekveldt, J. Sietsma, and S. van der Zwaag,
Ferrite/pearlite band formation in hot rolled medium carbon steel,
Materials Science and Technology, **18** (2002) 297-303.

N.H. van Dijk, S.E. Offerman, W.G. Bouwman, M.Th. Rekveldt, J. Sietsma, and
S. van der Zwaag, A. Bodin, and R.K. Heenan,
High temperature SANS experiments on Nb(C,N) and MnS precipitates in HSLA steel,
Metallurgical and Materials Transactions A, **33A** (2002) 1883-1891.

L.J.G.W. van Wilderen, S.E. Offerman, N.H. van Dijk, M.Th. Rekveldt, J. Sietsma, and
S. van der Zwaag,
Neutron depolarization study on the austenite/pearlite transformation in steel,
Applied Physics A, **74** (2002) S1052 - S1054.

N.H. van Dijk, S.E. Offerman, W.G. Bouwman, M.Th. Rekveldt, J. Sietsma,
S. van der Zwaag, A. Bodin, and R.K. Heenan,
SANS experiments on Nb(C,N) and MnS precipitates in HSLA steel,
Applied Physics A, **74** (2002) S978 – S980.

S.O. Kruijver, L. Zhao, J. Sietsma, S.E. Offerman, N.H. van Dijk, L. Margulies,
E.M. Lauridsen, S. Grigull, H.F. Poulsen, and S. van der Zwaag,
In situ observations on the austenite stability in TRIP steel during tensile testing,
Steel Research, **73** (2002) 236-241.

S.E. Offerman, N.H. van Dijk, J. Sietsma, S. Grigull, E.M. Lauridsen, L. Margulies,
H.F. Poulsen, M.Th. Rekveldt, and S. van der Zwaag,
Grain nucleation and growth during phase transformations,
ESRF Highlights, (2002) 66-67.

S.E. Offerman, N.H. van Dijk, M.Th. Rekveldt, J. Sietsma, and S. van der Zwaag,
3D neutron depolarization experiments on the phase transformations in steel,
Physica B, **276-278** (2000) 868-869.

Q. Lin, S.W. Simpson, S.E. Offerman, and M. Rados,
Pseudorandom noise injection as diagnostic tool for gas metal arc welding systems, Science
and Technology of Welding and Joining **4,** (1999) 312-316.

W.M. Rainforth, M.P. Black, R.L. Higginson, E.J. Palmiere, C.M. Sellers, I. Papst, P. Warbichler,
F. Hofer, N.H. van Dijk, S.E. Offerman, and P. Strunz,
A critical comparison of the methods of quantifying precipitate size distribution in a model Fe-30Ni-Nb microalloyed steel,
Accepted for publication in the Proceedings of the International Conference on Thermo-mechanical
Processing: Mechanics, Microstructure & Control, 23-26 June Sheffield, UK.

N. H. van Dijk, S. E. Offerman, J. C. P. Klaasse, J. Sietsma and S. van der Zwaag,
*High-temperature magnetisation measurements on the pearlite transformation kinetics in
nearly eutectoid steel,*
Journal of Magnetism and Magnetic Materials, in Press.

Curriculum vitae

1974   Born on the 2nd of October in Schiedam, the Netherlands

1993-1999:   Masters degree in Materials Science and Engineering at the
Delft University of Technology, Delft, the Netherlands.
Main subject: 'Theoretical and experimental development of surface tension
measurements under arc plasma conditions'

1996-1997:   Work experience at the Plasma Engineering research group of the faculty
of Electrical Engineering of the University of Sydney, Sydney, Australia.
Subject: 'Pseudorandom noise injection as diagnostic tool for gas metal
arc welding systems'

1999-2003:   Ph.D.-research at the Interfaculty Reactor Institute and the Laboratory of
Materials Science, Delft University of Technology, Delft, the Netherlands.
Subject: 'Evolving microstructures in carbon steel. A neutron and synchrotron
radiation study.'

2000:   Higher European Research Course for Users of Large Experimental
Systems, Grenoble, France

Present: Post-doctoral position at the Interfaculty Reactor Institute and the
Laboratory of Materials Science, Delft University of Technology, Delft,
the Netherlands.

A long-standing problem in the field of materials science is the understanding of the evolution of the microstructure during the formation of polycrystalline materials like metals and ceramics. The most important reasons for this are the limitations of the experimental and modeling techniques that prevent a detailed study of the grain nucleation and growth mechanisms. This thesis describes unique neutron and synchrotron measurements, which have hitherto not been realized with other techniques, on the evolution of the microstructure in the bulk of carbon steel, even down to the level of individual grains. These measurements are of vital importance for technological applications, because a better understanding of the evolution of the microstructure opens the opportunity for the industrial development of materials with superior strength and formability.